NUMERICAL INVESTIGATIONS OF THE EARLY STAGES OF PLANET FORMATION

NUMERICAL INVESTIGATIONS OF THE EARLY STAGES OF PLANET FORMATION

By JOSEF J. RUCSKA, B. SC.

A Thesis Submitted to the School of Graduate Studies in Partial Fulfilment of the Requirements for the Degree Master's of Physics.

McMaster University Master's of Science (2018) Hamilton, Ontario (Physics & Astronomy)
TITLE: Numerical investigations of the early stages of planet formation
AUTHOR: Josef J. Rucska, B.Sc. (McMaster University)
SUPERVISOR: Dr. James Wadsley
NUMBER OF PAGES: ix, 111

Abstract

Dust grains are a crucial component of disks around young stellar systems where current observations and theory show that planets form. Dust grains must grow 10 orders of magnitude in size to become planets. However, one of the early steps in this growth phase faces stringent theoretical constraints. The metre barrier relates to two well-studied physical mechanisms which inhibit grain growth beyond centimetre sizes. We report on numerical studies which probe these early stages of planet formation including instabilities that promote dust concentration such as the streaming instability (SI). We explore several different SPH models for dusty gas evolution. We find the linear SI is difficult for SPH to capture because it begins with perturbations below the 1% level. We also employ the Athena 3rd order Eulerian code which has been used to study the SI in the linear phase and the non-linear or saturated phase. We present numerical confirmations of recent analytical predictions of enhancements to the SI growth rates caused by the dust settling to the disk midplane in the earliest stages of the protoplanetary disk evolution. Symmetric analytical predictions for SI growth are not directly relevant to the non-axisymetric, planar geometry of the saturated, non-linear phase. We lay the ground work to explore this in future work.

Acknowledgements

I would like to thank my supervisor, Prof. James Wadsley, for his limitless support and patience over the course of the last two years. I have grown a lot as a researcher, and acquired an array of new skills as well as an appreciation for what makes a person a strong scientist. Much of this is thanks to his guidance. I would also like to thank Prof. Ralph Pudritz and Prof. Alison Sills for their committee support over the duration of this project, and Prof. Daniel Price for his helpful conversations during my time at Monash Univeristy in the fall of 2017. Our collaborators Prof. Tom Quinn and Dr. Isaac Backus at the University of Washington developed computer code which provided a strong starting point for the research presented in this thesis.

I would also like to thank Dr. Isaac Backus and Dr. Ben Keller, whom were both senior graduate students during my first year and were exceptionally helpful in my transition into graduate school. My office mates Jasper Grond and Tom Mudway were also invaluable for their moral support.

Lastly, I would like to thank Mum, Dad, my brother Ben, and my girlfriend Inna for forming the pillars of my support group at home. When it comes to managing the pressures that can arise in my studies, and in anything else in life, really, I could not do it without you.

This research has made use of the NASA Exoplanet Archive, which is operated by the California Institute of Technology, under contract with the National Aeronautics and Space Administration under the Exoplanet Exploration Program.

Contents

List of Figures

Chapter 1

Introduction

The presence of small, micrometre sized grains of solid material in the space between stars can be inferred by the extinction of observed starlight due to absorption by the dusty, solid material (Draine 2003). Observations in the infrared spectrum have demonstrated that dust is a major contributor the mass present in young stellar systems. It is widely accepted that planets form directly in the dynamic environments which surround these young stellar objects (de Pater and Jack J. Lissauer 2010). The mechanisms by which small dust grains become planets are poorly constrained, and this presents one of the fundamental problems in modern astrophysics.

1.1 Dust observations

The degree of the extinction of starlight caused by dust is highly dependent on the frequency of the light being observed (Draine 2003). Weingartner and Draine (2001) discuss a model grain size population distribution that recreates observed peaks in the extinction spectrum. They conclude that grains in the ISM are primarily 0.1-1 μm in size (see Figure 1.1), if the grains are modelled as spheres whose size is characterized by one length scale.

Spectral features from absorbed, scattered, and emitted light from dust grains, as well as meteorite samples, provide information on the chemical composition of the interstellar dust grains. Evidence suggests the major contributors to the grain population are silicates and carbonaceous compounds such as graphite. Polycyclic aromatic hydrocarbons (PAH's) are large molecules made of numerous carbon rings,

and they contribute strongly to emission and absorption in the 3-15 μm wavelength band, which interferes with parts of the dust grain spectra and makes it difficult to distinguish which features in this waveband are due to dust grains (Draine 2003).

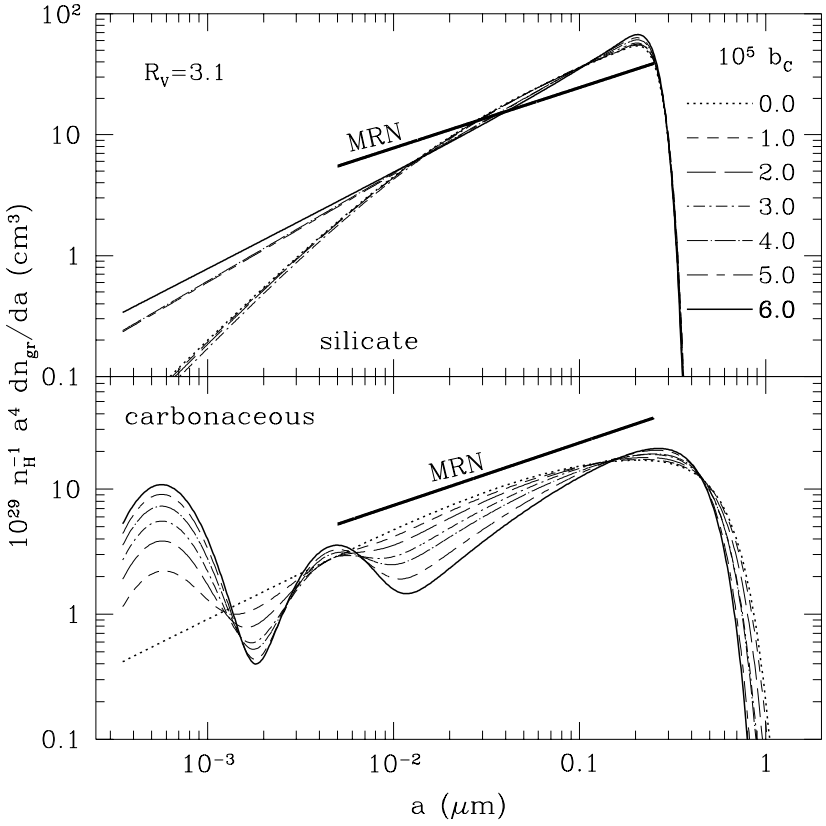

Figure 1.1: Differential population distribution of grain sizes dn_{gr}/da in the ISM, from a model presented in Weingartner and Draine (2001). This figure is reproduced from Weingartner and Draine (2001) with permission. The particle size, a, is plotted on the x-axis. Note the scale of the y-axis: the distribution is multiplied by a^4, as the overall distribution is dominated by a a^{-4} power law. n_H is the number density of H nuclei. The top panel is for a model of dust grains that are composed of silicates, and the bottom panel is for carbon-based grains.

Dust emits thermally in the infrared spectrum, and young stellar objects (YSO's) exhibit an excess of infrared spectrum intensity when compared to the intensity one would expect from a lone early star (see Figure 1.2 here, and Greene et al. (1994), Andre et al. (2000)). The spectral energy distributions (SED) from YSO's match emission models for a pre-main sequence star embedded in a circumstellar disk of dusty material (Adams et al. 1987). Thus the evidence suggests that compact envelopes

of dust surround these young stars, and they are of sufficient mass to dominate the infrared emission.

Early observational research surrounding these objects lead to a classification of YSO's based on the power-law slope of the infrared excess emission. These classes are interpreted as an evolutionary sequence which YSO's follow, where the material surrounding the young, pre-main sequence star transitions from a large, enveloping shell of dust to a developed, flattened circumstellar disk, and then to a thin, dispersed disk that does not provide much excess infrared radiation in the SED of the young star (Kenyon et al. (1993), Calvet et al. (1994)).

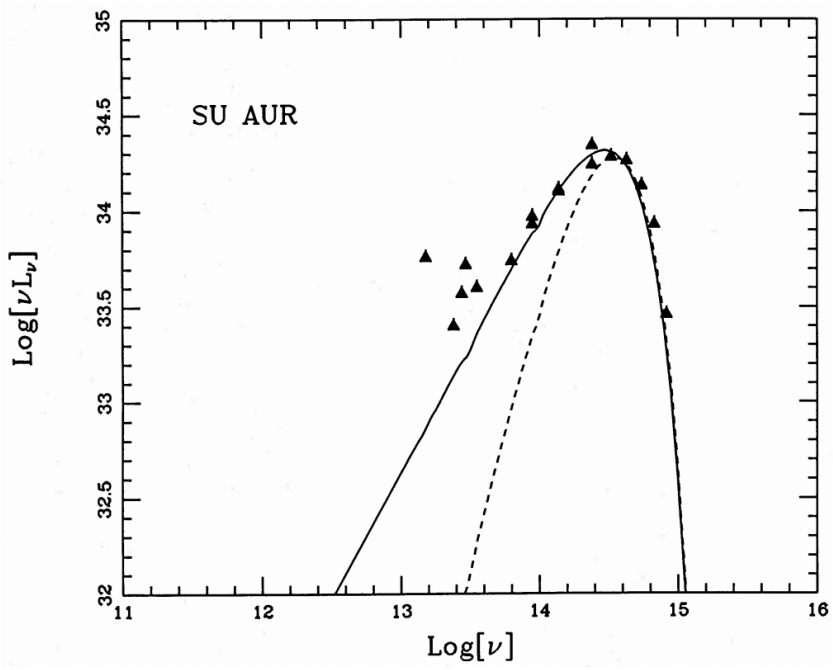

Figure 1.2: Observed spectrum of the young stellar object SU AUR in Taurus from Adams et al. (1987), reproduced with permission. The triangular points represent observational data, the dashed line shows a reddened black body, and the solid is the model developed in Adams et al. (1987) that includes emission from a circumstellar disk.

Some studies have imaged YSO's with circumstellar disks in the Orion nebula with the Hubble Space Telescope (Bally et al. (2000), Smith et al. (2005)). Many of these objects are surrounded by bright ionization fronts that are around 100 AU in size, and may also display dark, silhouettes that can be as wide as 1000 AU. At the time, these object were referred to as proplyds. Some of these silhouettes display a noticeable disk

shape, and suggest the presence of large a disk of dust grains orbiting these young stars and blocking their optical light, creating the dark silhouettes.

The Atacama Large Millimeter/submillimeter Array (ALMA, *ALMA Science Portal* (2018)) has given the observational community a high level of spatial resolution in the infrared spectrum that was previously entirely inaccessible. With ALMA, one can resolve dust structures in these YSO circumstellar disks. Recent observations have made protoplanetary disks (PPD's) one of the hottest topics in astronomy. A selection of ALMA observations of PPD's is provided in Figure 1.3. This specific selection was chosen to highlight the variety of shapes present in some of these PPD's.

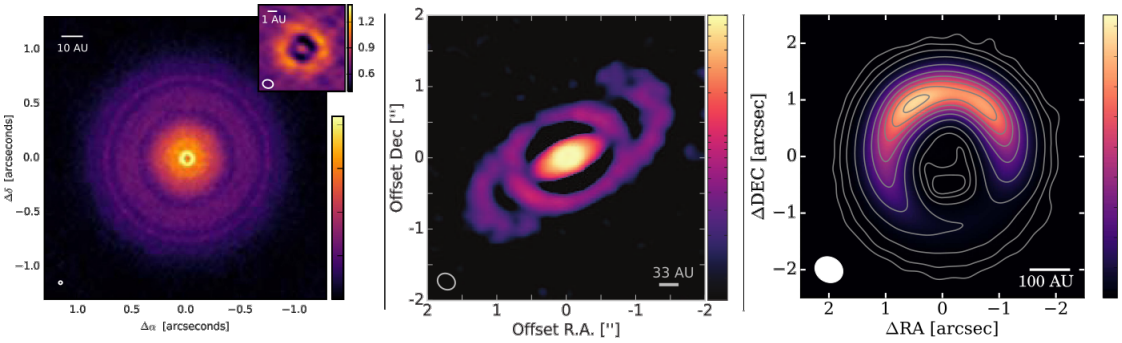

Figure 1.3: Observations of protoplanetary disks with ALMA. From left to right: TW Hya at 0.87 mm, Andrews et al. (2016); Elias 2-27 at 1.3 mm Pérez et al. (2016), HD 142527 at 0.87 mm Kataoka et al. (2016). All figures are reproduced here with permission.

The magnitude of the drag force applied to a dust grain as it moves through the gaseous disk will depend on the size of the dust grain. Thus, the dust structures that form in PPD's may vary with grain size. The PPD accompanying the star MWC758 has been imaged in the optical spectrum by the SPHERE instrument on the Very Large Telescope (Benisty et al. 2015) and at 0.87mm recently by ALMA (Dong et al. 2018). The two observations (provided in Figure 1.4) show how grains of different sizes are distributed differently in MWC758. In protoplanetary disks, ALMA observes dust grains near 1mm in size at the midplane of the disk, which emit thermally in the infrared spectrum. Scattered optical light (which is imaged by SPHERE in the Benisty et al. (2015) study) typically tracks smaller grains that exist at the surface layer of the protoplanetary disk. Dong et al. (2018) discuss the differences between the two images, which may be caused by projection effects or the difference in the

drag force for grains of different sizes.

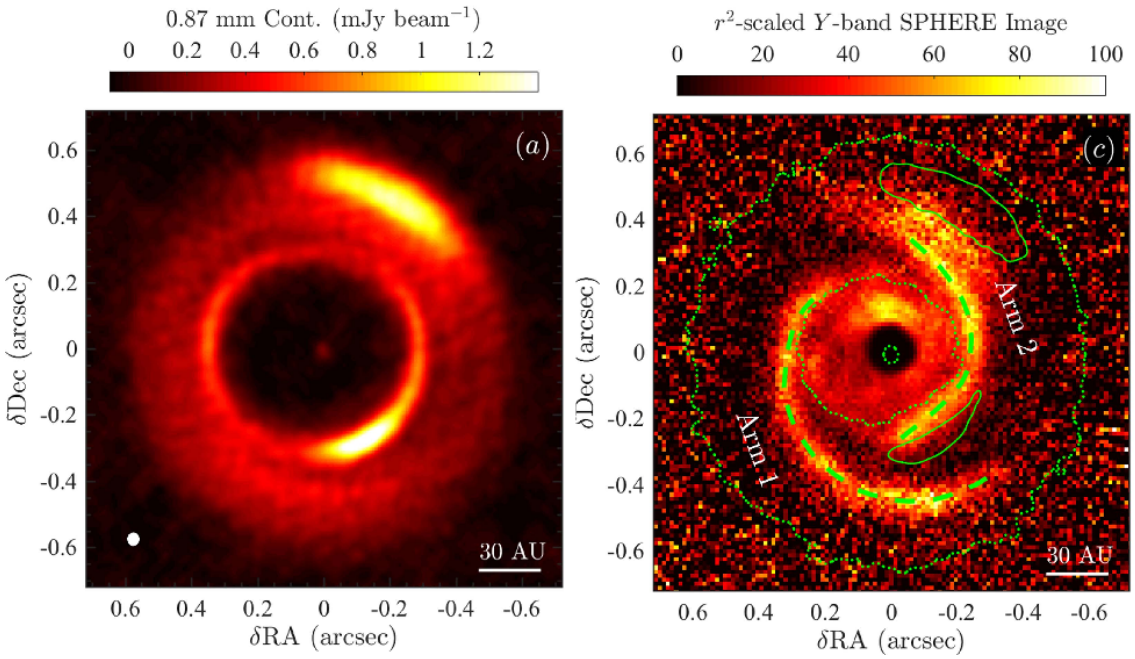

Figure 1.4: Observations of the protoplanetary disk MWC758. *Left.* ALMA 0.87 mm continuum emission (Dong et al. 2018). *Right.* $1/r^2$ scaled SPHERE 1 μm polarized scattered light image (Benisty et al. 2015). The left panel is reproduced from Dong et al. (2018) under the Creative Commons Attribution 3.0 licence. The right panel is reproduced from Benisty et al. (2015) with permission.

The data presented in these ALMA images hint that planets may form early in these disks and play a central role in the dynamics that follow. They may be responsible for creating the gaps in the dust structure and the asymmetrical features that have been observed by ALMA.

1.2 Exoplanet Observations

To date, nearly 4,000 planets external to our own solar system have been detected (*Exoplanet Archive* 2018). Most of these exoplanetary systems contain worlds which are very different in character from the planets we are familiar with. Figure 1.5 shows the distribution of discovered exoplanets according to their orbital period and mass.

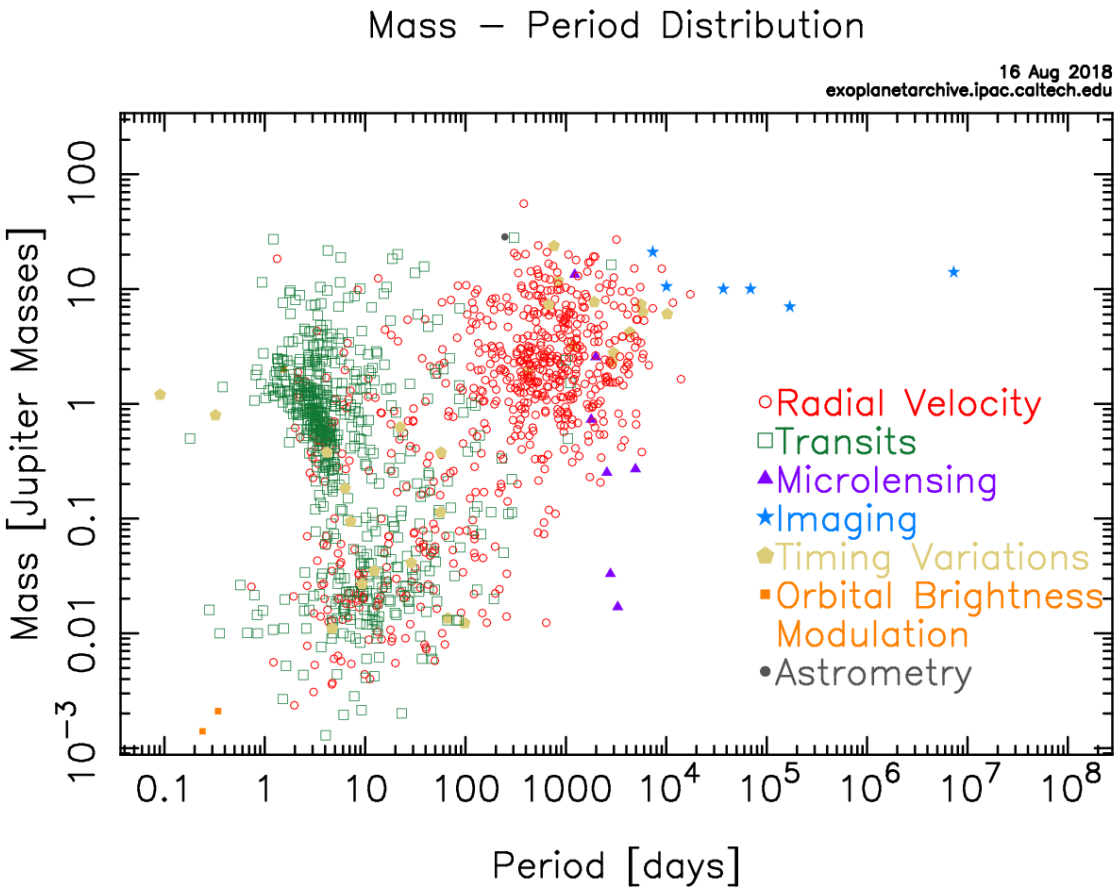

Figure 1.5: Distribution of confirmed exoplanets according to their orbital period and mass retrieved from *Exoplanet Archive* (2018), and reproduced here with permission. The mass data represent the product $M_{planet} \sin i$, where i is the angle of inclination from the line of sight to the orbital plane of the exoplanet-star system and is generally not known. The data are coloured by the observational technique used to discover them. Note: error bars have been omitted to reduce clutter. Some data points in this figure have significant uncertainties.

The general distribution of the planetary characteristics in Figure 1.5 is worth discussing in further detail, as it may contain clues about the nature of the planet formation process, and whether it may favour the production of planets of a particular size at a particular orbital radius over others. First, we will briefly introduce the main observational techniques used to discover exoplanets and the biases present within each technique. A more complete overview of these methods is available in Fischer et al. (2014).

The first Jupiter-mass planet around a Sun-like star was observed using the radial

velocity method (Mayor and Queloz 1995), which probes the emission spectra of stars for a signal that would signify a periodic wobble in the radial (line of sight) velocity of the star that could be caused by gravitational interactions with a planetary companion. However, this method is biased towards discovering high mass planets with short orbital distances to their star, as this would produce the largest possible signal.

For the 15 years that followed the first exoplanet discoveries, the radial velocity (RV) method proved to be the most efficient mechanism for discovering new planets; only a dozen or so exoplanets had been discovered using transits by 2007 (Charbonneau et al. 2007). A transit occurs when an exoplanet passes between its star and an observer, which results in the partial obstruction of the starlight by the planetary surface. With a sufficiently sensitive instrument, a periodic dimming of the star's brightness can be measured, leading to the conclusion that a non-luminous body (in optical wavelengths) is orbiting this star. NASA's Kepler Space Mission which launched in 2009 was designed to make use of transits to search for Earth-sized planets orbiting Sun-like stars (Borucki et al. 2010). The Kepler mission planned to monitor 150,000 stars for several years, and was capable of unprecedented photometric precision (J. J. Lissauer et al. 2014). As of August 2017, nearly 4,500 exoplanet candidates have been discovered by Kepler, and two thirds of all confirmed exoplanet discoveries have come from data collected by this mission.

The transit method for detecting exoplanets is also subject to a set of observational biases. Exoplanets with large radii will provide the strongest signal during a transit. Also, numerous orbits for each exoplanet need to be observed in order to confirm that the star dimming events are indeed due to planetary transits. Hence, the four-year lifespan of the Kepler mission limits the exoplanetary systems than can be confirmed to those that experience many orbits in the span of four years.

The data in Figure 1.5 suggests most of the observed exoplanets can be organized into three major groups: 1) 0.01 to 0.05 Jupiter masses, period of 4 to 12 days; 2) 0.2 to 3 Jupiter masses, period of 1 to 8 days; 3) 1 to 10 Jupiter masses, period 100 to 2000 days. For reference, Jupiter's orbital period is 4,330 days, Earth's mass is 0.003 Jupiter masses, and Neptune has a mass of 0.054 Jupiter masses and an orbital period of 6×10^4 days (Williams 2018).

The separation in mass for the planets with an orbital period between 1 and 100 days can be explained by the core accretion model, a theory that suggests gas giant planets form from a core of rocky material that triggers a hydrodynamic instability

in the gaseous disc when the core reaches a critical mass (Perri and Cameron (1974), Mizuno et al. (1978)). The instability enables the rapid infall of gas onto the rocky core, resulting in a rapid overall mass growth. The specific value of this critical mass is somewhat disputed in the literature, but it is apparent that it depends on the protoplanetary disk properties and accretion rates. Rafikov (2006) reports that this value can be between 0.02 and 0.19 Jupiter masses, for example. The gap between what we've called group 1 and group 2 seems to suggest a deficiency of exoplanets in the range of 0.05 to 0.2 Jupiter masses. Thus, the core accretion theory is a suitable explanation for the presence of this particular deficiency in the exoplanet population. It is unlikely that this gap is due to observational bias, as both group 1 and group 2 exoplanets have primarily been discovered by Kepler via the transit method, and if 0.02 Jupiter mass and 1.0 Jupiter mass planets are observable with this method, then a 0.1 Jupiter mass planet would presumably be observable as well.

The planets in group 1, in the lower left portion of Figure 1.5, have masses that roughly range from 3 Earth masses to 1 Neptune mass. A recent study by Fulton et al. (2017) has demonstrated that the planets within this group can be divided into two further sub-groups according to their radius (see Figure 1.6 below). These two classes of planets have thus been dubbed super-Earths and mini-Neptunes. Interestingly, there are no analogous objects in our solar system, yet dozens of such exoplanets have been discovered.

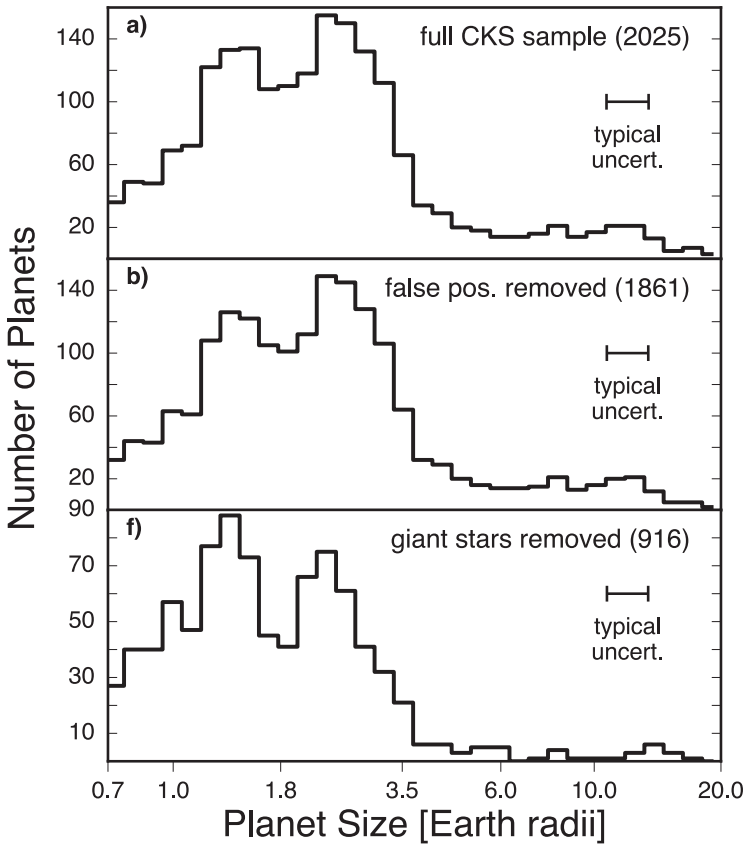

Figure 1.6: Histogram of planet radii from Fulton et al. (2017), reproduced with permission. The key result from this paper is the gap in the distribution that appears at around 1.8 Earth radii. This Figure is adapted from their Figure 2, which contains more panels than the three presented here. Each panel considers a subset of the full sample (except panel a)), and the presence of the gap in each panel supports the conclusion that this gap exists for exoplanets of many varieties.

Exoplanets have also been discovered using gravitational microlensing. When and object such as a star, galaxy, or system of stars and planets, crosses the line of sight between an observer and background stars, the gravity of the foreground object can create a pair of images of the source stars (Paczyński 1996). These events are in general rare and require significant observational infrastructure to be seen. However, even terrestrial mass planets that orbit at a few AU from their host star can be observed with this technique (Beaulieu et al. 2006). This is a regime of exoplanet properties that is currently inaccessible to the RV and transit methods. As can be seen in Figure 1.5, a lone pair of exoplanets have been discovered that have masses between 0.01 and 0.03 Jupiter masses and orbital periods of 2,000 to 3,000 days, and both have been

discovered via microlensing.

Exoplanets that are sufficiently massive, luminous, and spatially separated from their host star can actually be observed directly in infrared wavelengths with careful observational techniques. Marois et al. (2008) present the discovery of 3 exoplanets with a mass of ∼10 Jupiter masses in orbits with semi-major axes that range from ∼20 AU to ∼70 AU. For reference, Jupiter's orbital semi-major axis is approximately 5 AU. These planets discovered with direct imaging in Figure 1.5 are the only known exoplanets with orbits longer than 20,000 years.

The current image of the planetary and exoplanetary zoo may be incomplete, but the main lesson from the observations of exoplanets is that planetary systems come in all sorts of shapes and sizes, and our theories of planet formation must be able to account for this.

1.3 Constraints on Planet Formation Timelines

Theoretical models for the formation of planets have long been accompanied by well-documented and widely accepted time constraints for the formation timescale.

One well known constraint is reported in Ribas et al. (2014), which says that the circumstellar disks observed in young stellar objects (c.f. Section 1.1) only exist for ∼6 Myr (measured from the time the star formed) before the infrared excess which is characteristic of a circumstellar disk (c.f. Figure 1.2) is no longer observed. This imposes an upper limit for the timescale of the formation of giant gas planets, which must gather their gaseous envelopes from the protoplanetary disk. Not all core accretion models discussed in the literature at the time of the Ribas et al. (2014) paper were compliant with this constraint. Figure 1.7 demonstrates one of the main results from the Ribas et al. (2014) paper, plotting the age of various star forming regions along with the percentage of stars in those regions that display the infrared excess which is characteristic of a circumstellar disk (c.f. Figure 1.2).

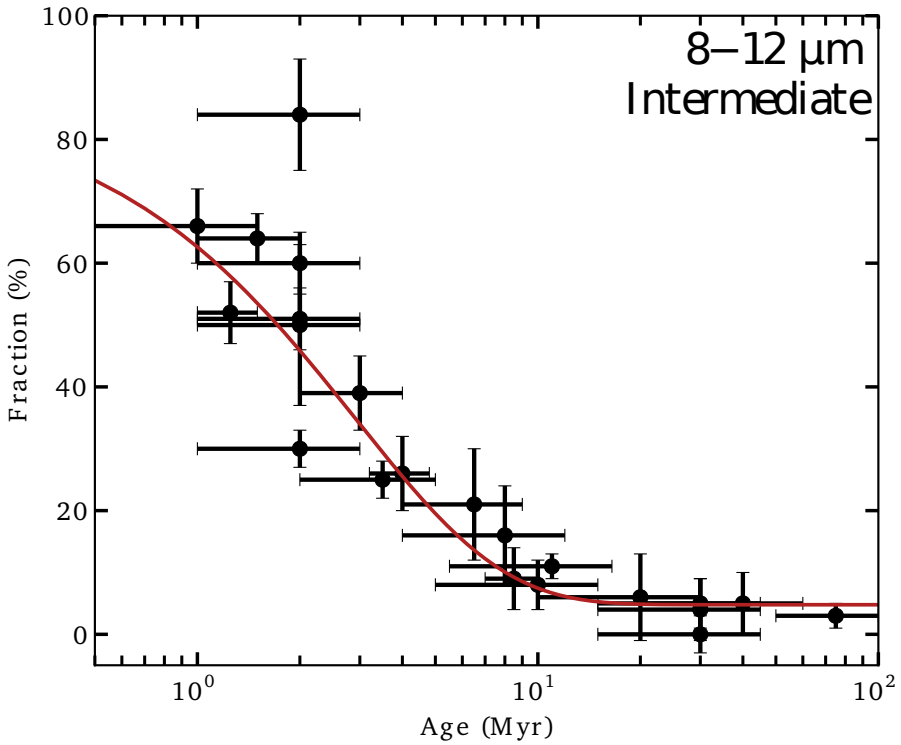

Figure 1.7: Fraction of stars in young star clusters that show evidence of a circumstellar disk as a function of the age of each cluster, reproduced from Ribas et al. (2014) with permission.

Dramatically more pressing time constraints than 6 Myr are imposed on planet formation when one considers the interactions between the dust grains and the gas in protoplanetary disks via aerodynamic drag, however.

The gas motions in a protoplanetary disk are dominated by the gravity of the central star. Thus, in the absence of any significant external perturbers or large pressure gradients, the gas will orbit on nearly circular, Keplerian orbits. However, the gas density will on average decrease as a function of distance from the central star, leading to a pressure gradient that points radially outwards. Thus, the gas will orbit at a slightly sub-Keplerian velocity. The dust particles—which do not create or respond to pressure gradients—will orbit at the Keplerian velocity. This results in the dust grains experiencing a headwind as they orbit in the disk, pushing them along inwardly spiralling orbits. For large dust objects that are comparable in size to asteroids in our solar system, their inertia is sufficiently large that their orbits are mostly undisturbed. Small, micron sized grains (which compose the dust in the interstellar medium, see

Figure 1.1) are tightly coupled to the gas via aerodynamic drag, and the terminal velocity in the radial direction is small. However, for dust objects of a specific size, near 1 metre, this radial drift effect can be substantial. Weidenschilling (1977) is the seminal paper on this topic. Two figures from this paper are reproduced here in Figure 1.8. A dramatic conclusion from this study is that metre sized objects which form in a gaseous disk somewhere between 1 and 8 AU will spiral into the central star in less than 1,000 years!

This result is one of the components of the so-called metre-barrier, and has presented a serious issue to the field of planet formation since its inception.

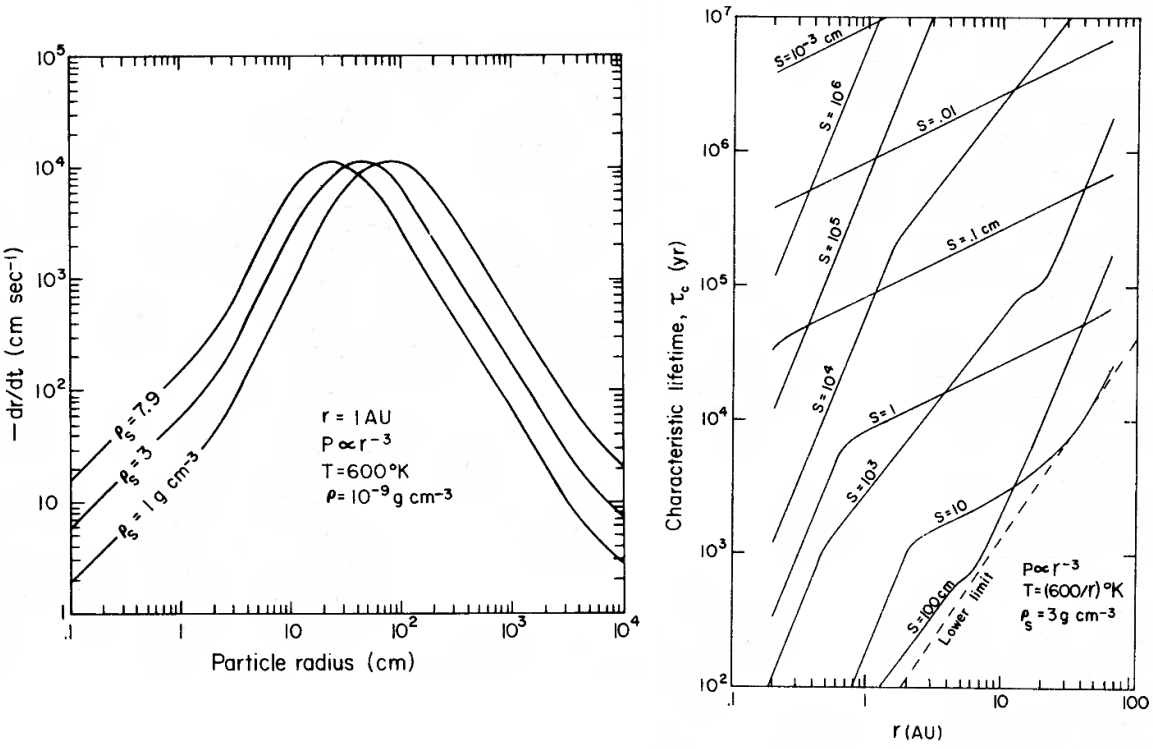

Figure 1.8: Rates of the radial drift of solid material orbiting in a gaseous protoplanetary disk based on analytical models, reproduced with permission from Weidenschilling (1977). Assumptions of the gaseous disk properties are inset in each panel. *Left.* The velocity of the radial drift $-dr/dt$ as a function of the particle size. The three lines represent three different values for the intrinsic bulk density of the solid material. *Right.* The timescale for solid particles to fall into the central star. The x-axis shows the radial position that each particle started at in the calculation. The different lines are for different particle sizes, s.

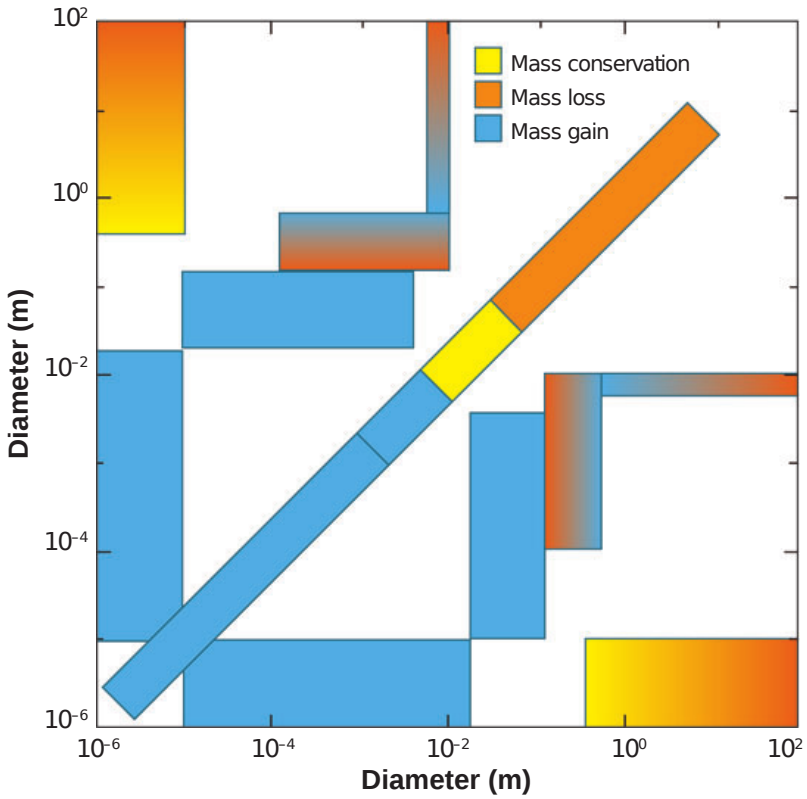

Figure 1.9: The consequences of collisions between dust grains in astrophysical environments according to experiments summarized in Blum and Wurm (2008). This figure displays a collision between two dust particles, and the size of each particle is represented on the opposing axes. Blue boxes represent a region of the particle size parameter space where collisions are always constructive, resulting in larger objects than the original two; orange represents destructive collisions where the resultant objects are always smaller; and yellow represents no net size change, such as collisions where the particles bounce off each other. Reproduced from Blum and Wurm (2008) with permission.

The other component of the metre-barrier comes from experimental studies and molecular dynamics simulations of collisions between dust grains. The results from a suite of such experiments is reviewed in Blum and Wurm (2008), and their summary figure is copied here in Figure 1.9. This figure presents a parameter space for a collision between two dust grains, where the size of one grain is on one axis and the size of the other grain is on the opposite axis. We see that when either of the collisional objects are beyond approximately 1 metre in size, the net result of any collision is always destructive. That is, the dusty material that leaves the collision is smaller in

size than either of the original objects that entered it. It is only in the parameter space where both objects are in the micron to centimetre range where the dust grains will stick together and become larger. Early models for the formation of planetesimals (which are solid bodies with sizes on the order of 1 km), relied on extensive dust grain coagulation (e.g. Weidenschilling (1980)). The results of the experiments presented in Blum and Wurm (2008) suggest coagulation alone can only bring dust grains to $\sim$10 cm in size. The dust grains used in these experiments may not be accurate analogues for dust grains in nature. Empirical data on the small scale, internal structure of interstellar dust grains is limited, and assumptions about this structure may affect the results of such collisional coagulation studies.

1.4 Rapid planetary core growth: pebble accretion

Recent research on a growth mechanism known as pebble accretion suggests that mm to cm dust grains—which are referred to as pebbles in the associated literature—may be the main contributor to the growth of small planetary cores (see Johansen and Lambrechts (2017) for a review). In short, the pebble accretion mechanism states aerodynamic drag that acts on pebbles as they approach the vicinity of a small planetary core will increase the likelihood of those pebbles being accreted by the core. With the pebble accretion mechanism, planetary cores as small as 0.1% of the Earth's mass can grow rapidly and become Earth mass cores or larger. Of course, important questions remain regarding the origins of these planetary cores, but pebble accretion permits a novel growth mechanism for the planet formation process. Previous gas giant planet formation theories (e.g. Pollack et al. (1996)) were built on the assumption of the existence of a large "ocean" of kilometre sized planetesimals which were accreted by planetary cores. A major problem that has faced such theories is the lack of a mechanism which can definitively create so many large solid objects. With pebble accretion, the population of solid bodies in protoplanetary disks can be a heterogeneous mix. An ocean of planetesimals is no longer required. We only need enough to produce a handful of planetary cores. The rest of the dust in the disk can remain as cm and mm dust grains—which have likely been created from the ISM μm dust grains via coagulation—and need not form planetesimals.

1.5 Streaming Instability

An important mechanism first introduced by Youdin and Goodman (2005) known as the streaming instability (SI) seems to offer a potential pathway for overcoming the metre barrier problem. We will discuss the machinery of the streaming instability in detail in Chapter 4, but will explore the results of some of the seminal SI studies in this section to argue for the potential of this instability to address the metre barrier.

1.5.1 Planetesimal formation

One of the major results involving high resolution, 3D simulations of the streaming instability is reported in Johansen et al. (2007). With a total dust to gas mass ratio within the simulation domain of 1%, and an initially disperse distribution of dust, the authors demonstrate that the streaming instability is able to concentrate the dust particles into locally overdense regions where the dust mass density is over 50 times as large as the gas density (see Figure 1.10). Within a few disk orbital times[1], the non-linearly evolving streaming instability produces a turbulent saturated state, where the maximum dust density no longer increases in time (Johansen and Youdin 2007). In the Johansen et al. (2007) study, once this turbulent state is reached, self-gravity is activated in the simulation. The authors want to highlight the ability of the SI to concentrate the dusty material without the influence of gravitational forces between the dust. If self-gravity was present from the beginning of the simulation, it would be difficult to distinguish the relative importance of the SI and gravity in forming clumps of solid material. When self-gravity is activated in the turbulent steady-state, these overdense regions quickly collapse azimuthally and form numerous bound clumps of solid material. In their simulations, one of these clumps contained a similar mass to that of the dwarf planet Ceres. Figure 1.11 shows the evolution of the surface density of the dust in the radial-azimuthal plane once self gravity was turned on.

This result supports the idea that the streaming instability can seed planetesimal formation from initially disperse distributions of small, centimetre sized grains. Once the dust particles are sufficiently clumped, self-gravity is capable of collapsing these over dense regions into macroscopic astrophysical objects.

[1]This concentration timescale depends on the properties of the dust and gas (Bai and Stone 2010b). A few orbital periods is valid for the grains with the fastest growth timescales.

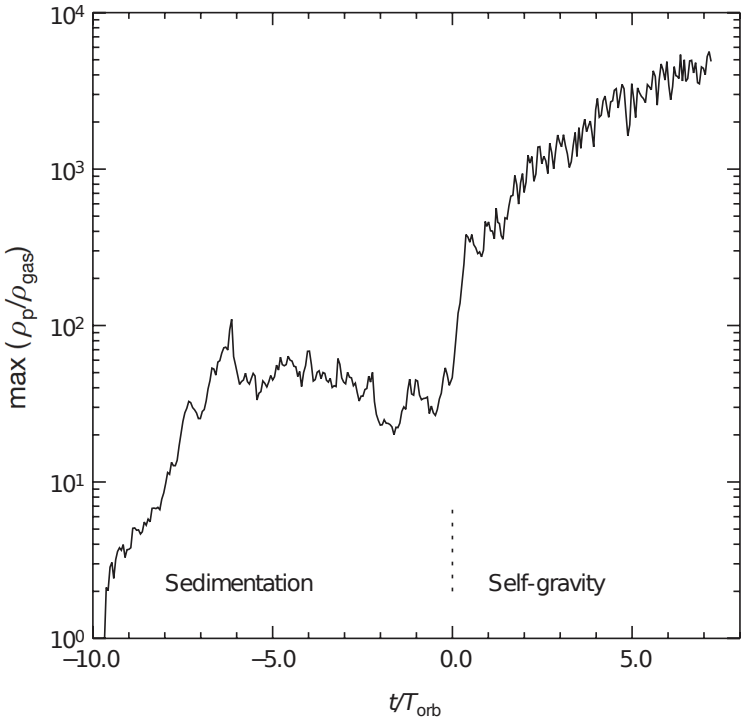

Figure 1.10: Maximum dust particle density present in the simulation in Figure 1.11 as a function of the elapsed simulation time. The simulation begins with drag and vertical gravity turned on at $t = -10T_{orb}$ (where T_{orb} is the orbital period). Initially, the maximum dust to gas density ratio is near 1%. The streaming instability creates overdense regions that saturate at $\max(\rho_p/\rho_{gas}) \sim 50$, and when self-gravity is activated, the maximum observed density increases dramatically. Reproduced from Johansen et al. (2007) with permission.

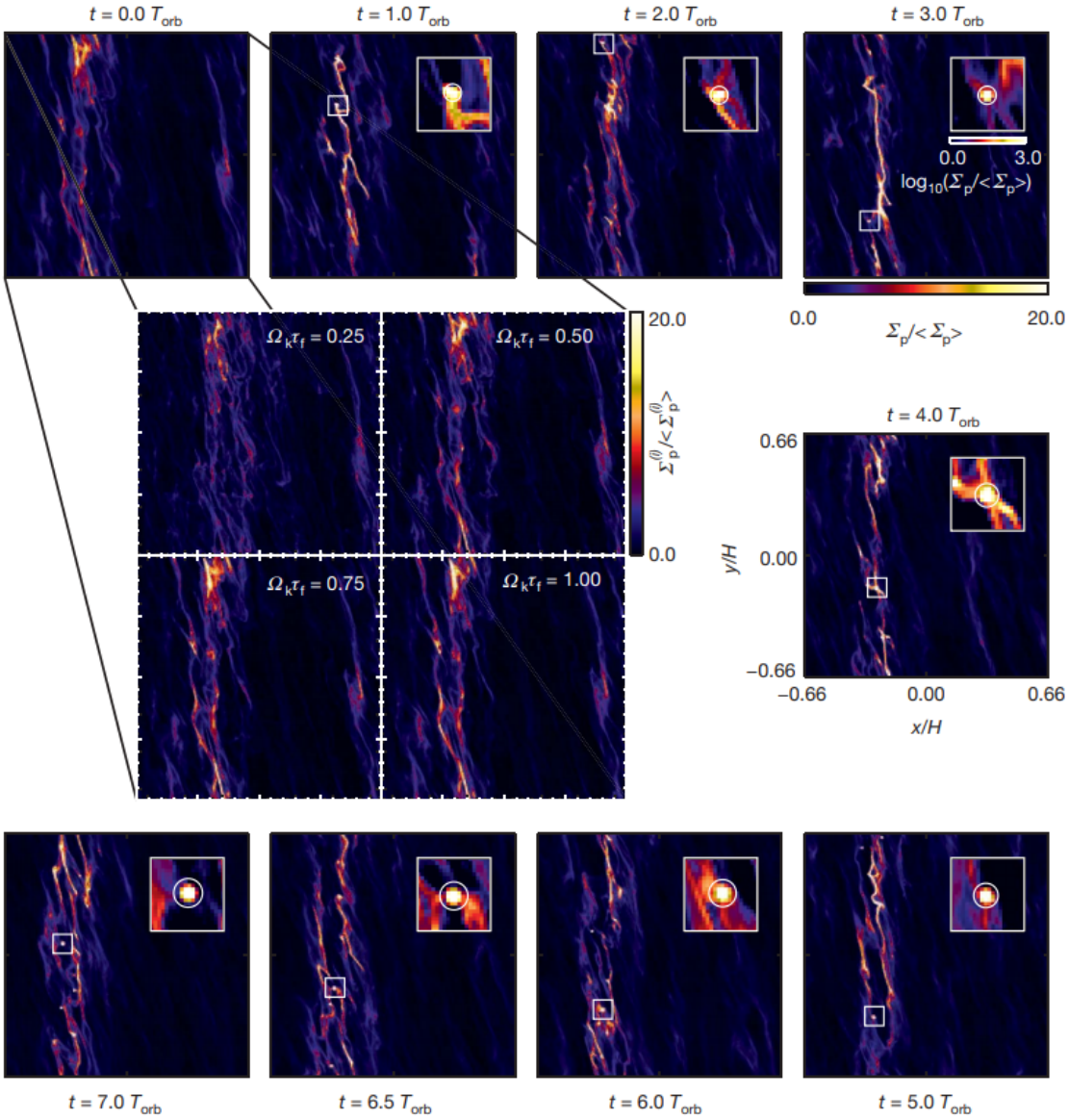

Figure 1.11: Gravitational collapse of over dense dust clumps into bound clumps in high resolution, 3D simulations of dust and gas in a shearing box, from Johansen et al. (2007), reproduced with permission. A gas cell resolution of 256^3 is used with 8×10^6 dust particles. The x and y axes of each image are the radial and azimuthal position, respectively, in units of the gas scale height. The colour represents dust surface density. In the middle of the figure, four panels shows the distribution of the different sizes of grains used simultaneously in their simulation. The inset in the frames displays a zoom-in of the highest mass clump, which reaches a similar mass as Ceres by the end of the simulation.

1.5.2 Multiple grain sizes

The Johansen et al. (2007) study discussed in the previous section did not consider a large range of particle sizes, and only used grains which span approximately an order of magnitude in size. Bai and Stone (2010b) use a very similar simulation set-up to Johansen et al. (2007), but do not consider the effects of self-gravity on the saturated, non-linearly evolving states. The main objective of this study was to investigate the differences in the aerodynamic interactions of different sized grains within the turbulence generated by the SI. We will only discuss a subset of their simulation suite, with some of the results reproduced here in Figures 1.12 and 1.13.

In order to provide context to the results of this study, we must define the parameter τ_s, which is dimensionless, and is represented by,

$$\tau_s = t_s \Omega \tag{1.1}$$

where t_s is the drag stopping time. The strength of the drag force that dust grains experience is characterized by t_s. Here, Ω is the Keplerian angular velocity which has units of inverse time. The stopping time t_s scales linearly with the grain size (for grains pebble sized and smaller), thus, in numerical experiments, τ_s is typically the parameter which is varied in order to control the grain size and consequently the strength of the drag force experienced by the grains. Johansen et al. (2007) used the notation $\Omega_k \tau_f$ to represent τ_s. We see from the middle panel of Figure 1.11, the authors used four different values for τ_s in their study: 0.25, 0.5, 0.75 and 1.0.

Small grains with a small τ_s will be tightly coupled to the gas, and large dust objects which are not tightly coupled will have large τ_s. Thus motions of the small grains will not deviate much from the motions of the gas, and the large inertia of large dust objects will result in their motions being mostly Keplerian and only slightly modified by the effects of the drag from the headwind they experience orbiting in the disk. Grains with an intermediate size which corresponds to $\tau_s \sim 1$, however, experience a relatively large perturbation from their Keplerian orbit due to the drag force. Johansen et al. (2007) used grains with $\tau_s \sim 1$ because the effects of the SI are most pronounced for grains with a size that corresponds to this value.

These simulations from Bai and Stone (2010b) presented here used 7 different particles sizes corresponding to the range $\tau_s = 10^{-4}$ and $\tau_s = 10^{-1}$. The sizes were chosen to be equally spaced out in a log scale across this range. The colours represent

the different sizes, and going from largest to smallest follow the order: black, green, blue, pink, cyan, yellow, red. Figure 1.12 shows the position of the particles in 3D and 2D simulations, and Figure 1.13 shows the scale heights of each particles species over time. Three different dust mass fractions were used, corresponding to 1%, 2% and 3% of the total gas mass.

We can see from the particle plots in Figure 1.12 that these smaller grains—which are less aerodynamically perturbed than the $\tau_s = \Omega_k \tau_f = 1$ grains from the Johansen et al. (2007) study—do not form dramatically clumped dust regions like the $\tau_s = 1$ grains. The black grains, which have a size near $\tau_s = 0.1$, are the only grains that form significantly dense filaments. In the 2D simulations with higher dust mass fractions, the particle scale heights are much smaller. This is also apparent in the plots of the particle scale height over time in Figure 1.13. Note that the y-axis scale in each row is different.

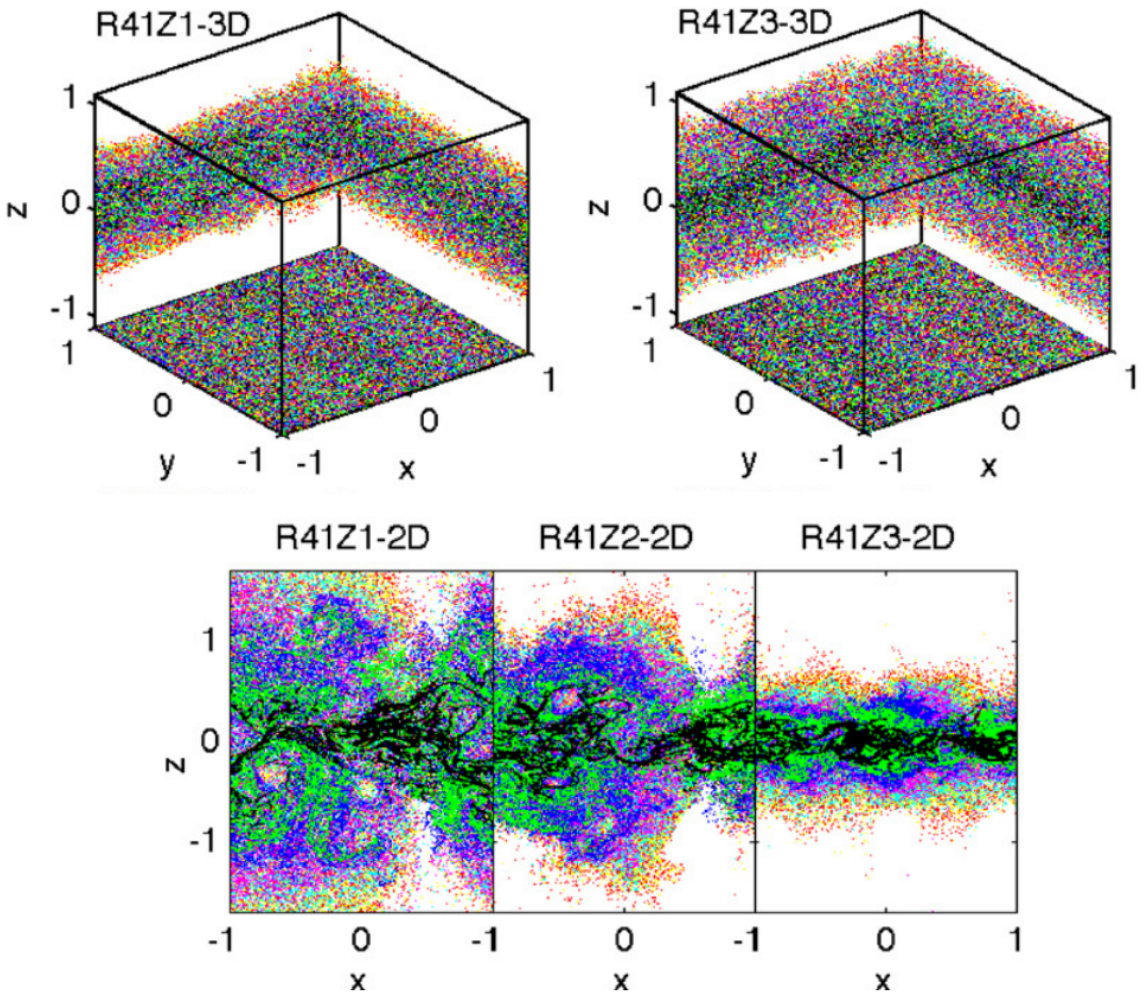

Figure 1.12: Particle distribution plots of the SI simulations from Bai and Stone (2010b) that have reach the saturated, non-linearly evolving stage. This figure is reproduced from Bai and Stone (2010b) with permission. The colours represent different grain sizes, and going from largest to smallest follow the order: black, green, blue, pink, cyan, yellow, red. Seven different particles sizes in the range $\tau_s = 10^{-4}$ and $\tau_s = 10^{-1}$ are used. The top panels are for the 3D simulations, and the bottom panels are for 2D. The labels Z1, Z2, and Z3 in the simulation naming convention refers to dust to gas mass ratios of 1%, 2%, and 3%, respectively.

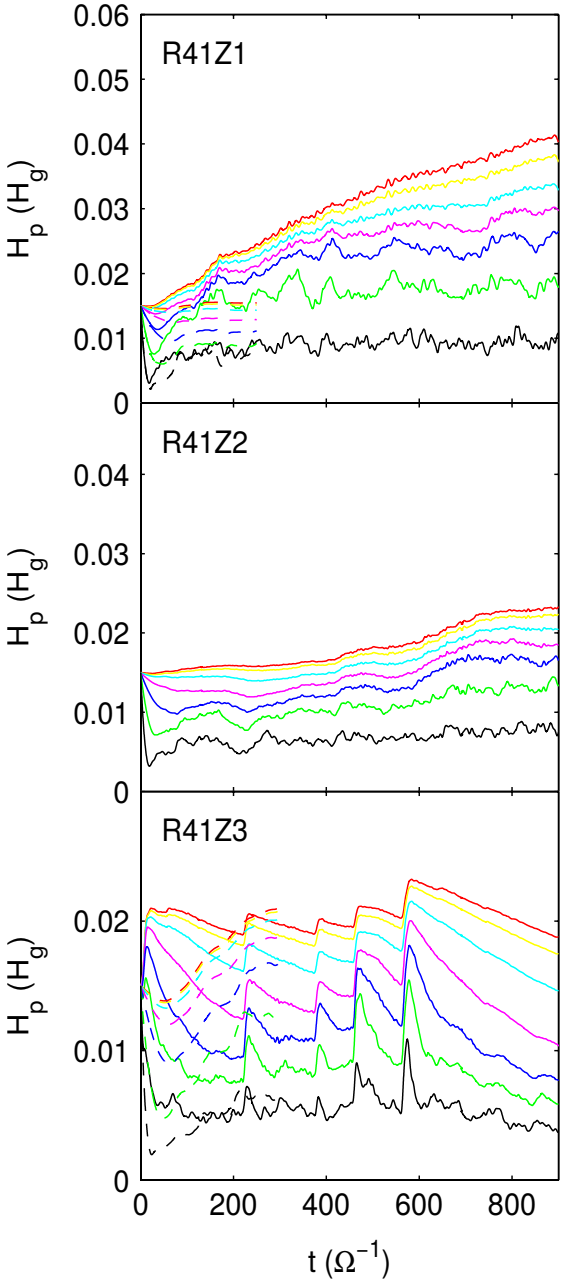

Figure 1.13: Particle scale heights over time for the simulations in Figure 1.12. This figure is reproduced from Bai and Stone (2010b) with permission. The colours represent different grain sizes, and going from largest to smallest follow the order: black, green, blue, pink, cyan, yellow, red. Data from the 2D simulations are represented by solid lines, data from the 3D are represented by the dashed lines. The labels Z1, Z2, and Z3 in the simulation naming convention refers to dust to gas mass ratios of 1%, 2%, and 3%, respectively.

1.6 Thesis overview

This thesis will discuss our research on the early stages of planet formation, where millimetre sized dust pebbles must grow to become kilometre sized planetesimals. However, there is an entire field of research dedicated to studying the late stages of planet formation. Some of the studies in this field involve investigating the gravitational interactions between formed planets and a large disk of planetesimal bodies (e.g. (Thommes et al. 2002), (Capobianco et al. 2011)). These interactions may be required to explain the organization of the planets in our solar system, such as the position of the large bodies Neptune and Uranus at large radial distances from the sun.

Numerical simulations provide a controlled environment where the behaviour of protoplanetary disks and the formation of planetesimals can be studied. The field of numerical simulations which incorporates hydrodynamics and aerodynamic interactions between gas and dust is relatively young, and the remainder of this thesis will report on our assessment and investigation of the state of the art numerical techniques and what we can learn by applying them to simulations of protoplanetary disks. In Chapter 2, we will discuss the two main mathematical models that are used to describe coupled dust-gas systems. In Chapter 3 we will discuss how these models can be implemented in smoothed particle hydrodynamics (SPH), and the issues facing the application of these models to full-scale simulations of protoplanetary disks. Noise present in SPH algorithms impedes the ability of these simulations to evolve small perturbations. The linear evolution regime of the streaming instability, a proposed mechanism for overcoming the aforementioned metre barrier to planet formation which we are interested in studying, requires the ability to numerically integrate such perturbations. Thus, we decided to use an established Eulerian astrophysics simulation code to simulate the streaming instability. In Chapter 4 we discuss the streaming instability in detail including analytical development of expected linear growth rates. We also discuss our investigation of recent updates reported in the literature via both analytical work and simulations, discussions of prominent features in the dust distribution from the non-linearly evolving regime of the streaming instability, and open questions still facing the mechanism. For example, no serious connection has been made between the predictions of the analytical linear growth regime results and the results from the high resolution, 3D simulations of the non-linear regime, and we believe this is a large open question facing this topic that could provide details about

the behaviour of the streaming instability in full protoplanetary disks.

Chapter 2

Modelling Dust

In this chapter we will discuss the mathematical models that we use to describe an interpenetrating dust and gas fluid. The numerical schemes discussed in further chapters will be based off the models described here. This discussion will include a description of the parameters that determine the strength of the aerodynamic drag interaction between the dust and gas, as well as the dynamical timescales present in the system and how these timescales guide the time stepping constraints in our numerical schemes.

2.1 Two Fluid

We can describe a dust-gas mixture as two, interpenetrating fluids, and the equations governing the motions of these fluids can be written as (Harlow and Amsden (1975), Monaghan and Kocharyan (1995), Laibe and Price (2012)),

$$\frac{\partial \boldsymbol{v}_d}{\partial t} + (\boldsymbol{v}_d \cdot \nabla)\boldsymbol{v}_d = \boldsymbol{g} + \boldsymbol{a}_d - \frac{\boldsymbol{F}_{drag}}{\rho_d} \tag{2.1a}$$

$$\frac{\partial \boldsymbol{v}_g}{\partial t} + (\boldsymbol{v}_g \cdot \nabla)\boldsymbol{v}_g = \boldsymbol{g} + \boldsymbol{a}_g - \frac{\nabla P_g}{\rho_g} + \frac{\boldsymbol{F}_{drag}}{\rho_g} \tag{2.1b}$$

$$\frac{\partial \rho_d}{\partial t} + \nabla \cdot \Big(\rho_d \boldsymbol{v}_d\Big) = 0 \tag{2.1c}$$

$$\frac{\partial \rho_g}{\partial t} + \nabla \cdot \Big(\rho_g \boldsymbol{v}_g\Big) = 0 \tag{2.1d}$$

$$\frac{\partial U_d}{\partial t} + (\boldsymbol{v}_d \cdot \nabla) U_d = -\frac{\Lambda_{therm}}{\rho_d} \tag{2.1e}$$

$$\frac{\partial U_g}{\partial t} + (\boldsymbol{v}_g \cdot \nabla) U_g = -\frac{P_g}{\rho_g}(\nabla \cdot \boldsymbol{v}_g) + K(\boldsymbol{v}_d - \boldsymbol{v}_g)^2 + \frac{\Lambda_{therm}}{\rho_g} \tag{2.1f}$$

where $\boldsymbol{v}_d$ is the dust velocity, ρ_d is the dust density, $\boldsymbol{v}_g$ is the gas velocity, and ρ_g is the gas density. Here $\boldsymbol{g}$ is the acceleration due to gravity, and $\boldsymbol{a}_d$ and $\boldsymbol{a}_g$ are accelerations that individually act on the dust and gas phases respectively due to physics other than hydrodynamics, gravity and drag, such as magnetic fields. The specific (per unit mass) internal energy of the gas and dust are given by U_g and U_d respectively, the $K(\boldsymbol{v}_d - \boldsymbol{v}_g)^2$ term is the (non-specific) frictional heating energy associated with drag, and Λ_{therm} is the (non-specific) thermal coupling energy between the dust and the gas phase[1].

In this description we have omitted the buoyancy effects created by the finite size of the dust particles. Previous studies (e.g. Monaghan and Kocharyan (1995), Laibe and Price (2012)) have retained these terms in order to develop a general algorithm for dust-gas mixtures, but in astrophysics the intrinsic density of the dust material is much higher than the volume density of the dust particles, so we can assume the gas pressure gradients do not directly impart a force on the dust.

Equation 2.1b demonstrates that a parcel of gas feels a hydrodynamic pressure (the $-\nabla P_g/\rho_g$ term) that is exerted on it by nearby parcels of gas. In contrast, the dust fluid is pressure-less, and contains no such term. Thus, even in the absence of more exotic forces that would appear in the $\boldsymbol{a}_g$ and $\boldsymbol{a}_d$ terms, there will always be a difference between the net force exerted on the gas and the net force exerted on the dust.

The drag force $\boldsymbol{F}_{drag}$ can be written simply as,

$$\frac{\boldsymbol{F}_{drag}}{\rho_{(g,d)}} = \frac{K}{\rho_{(g,d)}}(\boldsymbol{v}_d - \boldsymbol{v}_g) \tag{2.2}$$

where K is the drag constant. In the Epstein drag regime, where the particle size is much smaller than the mean free path of the gas (typically valid in astrophysics) and the gas and dust velocities are subsonic, K is of the form (Epstein (1924), Baines et al.

[1]For further discussion on these frictional heating and coupling terms, see Harlow and Amsden (1975) and Laibe and Price (2012)

(1965), Laibe and Price (2012)),

$$K = \frac{4\pi}{3}\frac{\rho_d \rho_g}{\rho_{grain} s_d}\sqrt{\frac{8}{\pi\gamma}}c_s \tag{2.3}$$

where c_s is the sound speed of the gas, γ is the adiabatic index in the typical adiabatic equation of state $P = (\gamma - 1)\rho_g U_g$, where U_g is the gas internal energy, ρ_{grain} is the intrinsic density of the dust grains and is approximately 2.6 g cm^{-3} for silicates (Moore and Rose 1973) and s_d is the radius of the dust grains if they are assumed to be spherically shaped. Note that the above prescription for K is independent of $(\boldsymbol{v}_d - \boldsymbol{v}_g)$, so in this case $\boldsymbol{F}_{drag} \propto (\boldsymbol{v}_d - \boldsymbol{v}_g)$. In general, K can contain scaling relations with $(\boldsymbol{v}_d - \boldsymbol{v}_g)$ and the size of the dust grains that makes the overall scaling of the drag force with these quantities non-linear.

The material derivative, which considers the time derivative of some quantity R in the frame moving with a velocity given by $\boldsymbol{V}$, is represented by,

$$\frac{\mathrm{d}R}{\mathrm{d}t} = \frac{\partial R}{\partial t} + \boldsymbol{V}\cdot\nabla R \tag{2.4}$$

This is a general expression for a frame moving with a constant velocity $\boldsymbol{V}$, but for our purposes this velocity will be that of either the gas or the dust fluids. Going forward, when we write this derivative for dust quantities the velocity used in this derivative will be $\boldsymbol{v}_d$, the dust fluid velocity, and for gas quantities this will be $\boldsymbol{v}_g$, the gas fluid velocity. We will not introduce any explicit notation to mark this difference, but instead rely on the context of each equation to imply which velocity is used.

If we note,

$$\nabla\cdot\Big(\rho\boldsymbol{V}\Big) = (\boldsymbol{V}\cdot\nabla)\rho + \rho(\nabla\cdot\boldsymbol{V})$$

and assume no other forces are acting on the system (such as magnetic fields, stellar winds, etc.), then $\boldsymbol{a}_d$ and $\boldsymbol{a}_g$ are zero and the complete equations for the interpenetrating dust and gas fluids become,

$$\frac{\mathrm{d}\boldsymbol{v}_d}{\mathrm{d}t} = \boldsymbol{g} - \frac{K}{\rho_d}(\boldsymbol{v}_d - \boldsymbol{v}_g) \tag{2.5a}$$

$$\frac{\mathrm{d}\boldsymbol{v}_g}{\mathrm{d}t} = \boldsymbol{g} - \frac{\nabla P_g}{\rho_g} + \frac{K}{\rho_g}(\boldsymbol{v}_d - \boldsymbol{v}_g) \tag{2.5b}$$

$$\frac{\mathrm{d}\rho_d}{\mathrm{d}t} = -\rho_d(\nabla \cdot \boldsymbol{v}_d) \tag{2.5c}$$

$$\frac{\mathrm{d}\rho_g}{\mathrm{d}t} = -\rho_g(\nabla \cdot \boldsymbol{v}_g) \tag{2.5d}$$

$$\frac{\mathrm{d}U_d}{\mathrm{d}t} = -\frac{\Lambda_{therm}}{\rho_d} \tag{2.5e}$$

$$\frac{\mathrm{d}U_g}{\mathrm{d}t} = -\frac{P_g}{\rho_g}(\nabla \cdot \boldsymbol{v}_g) + K(\boldsymbol{v}_d - \boldsymbol{v}_g)^2 + \frac{\Lambda_{therm}}{\rho_g} \tag{2.5f}$$

We can see from equations equations 2.5a-b that K must have units of mass density on time. We can rewrite K to be of the form,

$$K = \frac{\rho_d}{t_s}$$

where t_s is a dimensional time parameter that characterizes the "stopping time" that regulates the drag force between the dust and the gas fluids. For the Epstein drag regime where K is given by equation 2.3, the stopping time is,

$$t_s = \frac{3}{4\pi}\frac{\rho_{grain} s_d}{\rho_g c_s}\sqrt{\frac{\pi\gamma}{8}} \tag{2.6}$$

Note that this quantity is dependent on local gas properties like the density ρ_g and the sound speed c_s, and, crucially, the size of the dust grains s_d. As discussed in Section 1.5.2, it is common to in the context of dust and gas orbiting a young star in a protoplanetary disk to define a dimensionless stopping time by multiplying t_s by the disk angular frequency Ω.

It is also useful to define a mass ratio between the dust and gas and rewrite the drag terms using this ratio rather than the dust and gas densities. However, different conventions exist in the literature for what ratio should be represented. At times the ratio between the dust and the gas mass is used, and at other times the fraction of the total fluid mass that is dust is used. We will use both conventions at different sections in this thesis, so we will define both here with their own symbol.

We will represent the fraction of the total mass that is dust with ϵ,

$$\epsilon \equiv \frac{\rho_d}{\rho_d + \rho_g} \tag{2.7}$$

and the dust mass to gas mass ratio, with μ,

$$\mu \equiv \frac{\rho_d}{\rho_g} \tag{2.8}$$

2.2 One-Fluid

An alternative mathematical description for the two interpenetrating fluids can be written. Laibe and Price (2014a) refer to this new description as a "one-fluid" scheme, however, we would like to stress that it is only in a mathematical sense that this description represents a single, mixed fluid. The physical system being studied is still two distinct fluids: a gas fluid, and a pressure-less dust fluid.

Following Laibe and Price (2014a), we will implement a change of variables, and instead of tracking ρ_d and ρ_g, we can track the total density $\rho = \rho_d + \rho_g$ and dust mass ratio ϵ (as defined in equation 2.7). Similarly, instead of evolving $\boldsymbol{v}_g$ and $\boldsymbol{v}_d$, we can follow the differential velocity between the dust and the gas phases, $\boldsymbol{w} \equiv \boldsymbol{v}_d - \boldsymbol{v}_g$ and the barycentric velocity,

$$\boldsymbol{V}_{bc} \equiv \frac{\rho_g \boldsymbol{v}_g + \rho_d \boldsymbol{v}_d}{\rho_g + \rho_d}$$

which is the mass weighted average velocity of the fluid mixture.

We will simply report the results of this rearranging from Laibe and Price (2014a), who determine the new system of equations to be,

$$\frac{\mathrm{d}\rho}{\mathrm{d}t} = -\rho(\nabla \cdot \boldsymbol{V}_{bc}) \tag{2.9a}$$

$$\frac{\mathrm{d}\epsilon}{\mathrm{d}t} = -\frac{1}{\rho}\nabla \cdot \Big(\epsilon(1-\epsilon)\rho \boldsymbol{w}\Big) \tag{2.9b}$$

$$\frac{\mathrm{d}\boldsymbol{V}_{bc}}{\mathrm{d}t} = -\frac{\nabla P_g}{\rho} - \frac{1}{\rho}\nabla \cdot \Big(\epsilon(1-\epsilon)\rho \boldsymbol{w}\boldsymbol{w}\Big) + (1-\epsilon)\boldsymbol{a}_g + \epsilon \boldsymbol{a}_d + \boldsymbol{a} \tag{2.9c}$$

$$\frac{\mathrm{d}\boldsymbol{w}}{\mathrm{d}t} = -\frac{\boldsymbol{w}}{t_s(1-\epsilon)} + (\boldsymbol{a}_d - \boldsymbol{a}_g) + \frac{\nabla P_g}{(1-\epsilon)\rho} - (\boldsymbol{w}\cdot\nabla)\boldsymbol{V}_{bc} - \frac{1}{2}\nabla\Big((2\epsilon-1)\rho\boldsymbol{w}^2\Big) \quad (2.9\mathrm{d})$$

$$\frac{\mathrm{d}U_g}{\mathrm{d}t} = -\frac{P_g}{(1-\epsilon)\rho}\nabla\cdot(\boldsymbol{V}_{bc} - \epsilon\boldsymbol{w}) + \epsilon(\boldsymbol{w}\cdot\nabla)U_g + \epsilon\frac{\boldsymbol{w}^2}{t_s} \quad (2.9\mathrm{e})$$

where, as before, $\boldsymbol{a}_d$ and $\boldsymbol{a}_g$ are accelerations due to physics outside of hydrodynamics, drag, and gravity, that act on either the dust or gas phase, respectively. Accelerations that are applied to both fluids are represented by $\boldsymbol{a}$. In the derivation of these equations we have assumed that the dust and gas are weakly thermally coupled, so that the Λ_{therm} term from before is zero.

2.2.1 Terminal velocity approximation

When the stopping time (equation 2.6) is small compared to all other dynamical timescales in the system, we can assume that the dust rapidly reaches the terminal velocity set by the local dynamics of the gas (pressure forces, magnetic forces, etc.) (Youdin and Goodman 2005).

This approximation is valid for large values of K, or, equivalently, small dust grains (cf. equation 2.3) that are tightly coupled to the gas and feel large drag forces.

In the terminal velocity approximation the relative velocity between the dust and gas, $\boldsymbol{w}$, is not explicitly tracked and we say instead,

$$\boldsymbol{w} \approx t_s\Big(\frac{\nabla P_g}{\rho} + \Delta\boldsymbol{a}\Big) \quad (2.10)$$

and the other one-fluid equations become (Price and Laibe 2015),

$$\frac{\mathrm{d}\rho}{\mathrm{d}t} = -\rho(\nabla\cdot\boldsymbol{V}_{bc}) \quad (2.11\mathrm{a})$$

$$\frac{\mathrm{d}\epsilon}{\mathrm{d}t} = -\frac{1}{\rho}\nabla\cdot\Big(\epsilon(1-\epsilon)\rho t_s\Big(\frac{\nabla P_g}{\rho} + \Delta\boldsymbol{a}\Big)\Big) \quad (2.11\mathrm{b})$$

$$\frac{\mathrm{d}\boldsymbol{V}_{bc}}{\mathrm{d}t} = -\frac{\nabla P_g}{\rho} + (1-\epsilon)\boldsymbol{a}_g + \epsilon\boldsymbol{a}_d + \boldsymbol{a} \quad (2.11\mathrm{c})$$

$$\frac{\mathrm{d}U_g}{\mathrm{d}t} = -\frac{P_g}{(1-\epsilon)\rho}(\nabla\cdot\boldsymbol{V}_{bc}) - \epsilon t_s(\Big(\frac{\nabla P_g}{\rho} + \Delta\boldsymbol{a}\Big)\cdot\nabla)U_g \quad (2.11\mathrm{d})$$

where $\Delta \boldsymbol{a} \equiv \boldsymbol{a}_d - \boldsymbol{a}_g$.

2.3 Timestepping

When discretizing a system of differential equations, one must take great care in ensuring that the separation between adjacent points in the discretized domain (i.e. step size) creates an approximate solution that acceptably reproduces the physical properties of the real system. Typically, smaller step sizes increase the accuracy of the approximation, however, when solving these discretized equations using computer programs, smaller step sizes will require longer computing times. Thus, it is imperative that the programmer employs the largest possible step size that provides a solution which is sufficiently accurate.

Consider a differential equation of the form,

$$\frac{\partial u}{\partial t} + C\frac{\partial u}{\partial x} = 0$$

where u is a quantity that describes a property in the x-t plane, and C is a constant. The Courant-Friedrichs-Lewy (CFL) criterion (Courant et al. (1967), LeVeque (2006)) describes the following constraint that is necessary for the stability of the numerical solution to the above equation,

$$\Delta t \leq \left| \frac{\Delta x}{C} \right| \tag{2.12}$$

where Δt is the step size in the t coordinate and Δx is the step size in the x coordinate.

Differential equations of the above form are common in physics. Particularly, the continuity equation in fluid mechanics is one such equation, represented here in equations 2.1c-d. If we consider equations 2.1c-d and fluid with a steady flow described by a speed c_s, then the CFL criterion becomes,

$$\Delta t \leq \left| \frac{h}{c_s} \right| \tag{2.13}$$

where h is the typical 3-dimensional spatial separation between fluid elements.

Equation 2.13 describes a bare-minimum condition that Δt must comply with[2]. For values of Δt larger than this criterion, the numerical solution is invalid.

[2]This assumes h is not a tuneable parameter. If it were, then it could be adjusted to ensure the CFL criterion remains true.

In the context of astrophysical computer simulations, other time-stepping criteria can be applied to ensure accuracy in the numerical solution. For instance, for a region of the simulation where numerical elements are separated in space by h and exposed to an acceleration a (which could be from a gravitational field, for instance), then one can write a simple time-stepping constraint of the form (Monaghan 1992),

$$\Delta t \leq \eta \sqrt{\frac{h}{a}} \tag{2.14}$$

where η is constant and follows $0 < \eta < 1$.

For aerodynamic drag forces, a simple time-stepping constraint is given by,

$$\Delta t \leq t_s \tag{2.15}$$

where t_s is the stopping time (2.6), and is the characteristic dynamical time for the drag force. For small, tightly-coupled dust grains this becomes a harsh constraint, and can dramatically slow down computer simulations that include drag physics.

The one-fluid formalism with the terminal velocity approximation (section 2.2.1), is well suited to tracking dust in this strong drag regime as it removes the physical dynamics that depend on t_s as a timescale and replaces them with an approximation. An effective dust-gas simulation program would use a two-fluid scheme when t_s is large, and would use a full one-fluid scheme (equations 2.9) or a one-fluid scheme with the terminal velocity approximation when t_s is small.

Chapter 3

Simulations of full protoplanetary disks in SPH

Computer simulations employing the numerical method known as smoothed particle hydrodynamics (SPH) to study the evolution of dust have become prevalent in the planet formation literature over the past few years. Some studies have attempted to directly explain the physical origins of features present in ALMA observations of dust in protoplanetary disks. A few examples of such studies include Dipierro et al. (2015), who recreated the ring and gap systems in HL Tau, and Price et al. (2018), who recreated the axisymmetric "horseshoe" shape of HD 142527. SPH has also been used to study the mechanisms by which planets embedded in dust and gas in protoplanetary disks can create gaps in the dust distribution more generally (Dipierro et al. 2016), and how planetesimals and smaller grains of dust can accumulate in the local gas pressure maxima at the edges of these gaps (Ayliffe et al. 2012). A study published by Lorén-Aguilar and Bate (2016) reports that toroidal vortices that are created when the dust grains settle from to midplane of the disk.

One particularly intriguing study from Gonzalez et al. (2017) claimed to have outlined a mechanism that can overcome the metre barrier problem that faces planet formation. Their study introduces what the authors refer to as a self-induced dust trap, which is created when dust drifting radially inward encounters a local gas pressure maximum. Their description of how these traps are created is as follows: the back-reaction drag force—the momentum that the dust exerts on the gas, via drag—pushes the gas outwards, radially, in opposition to the viscous forces which push gas inwards.

The competition between these two forces enhances the previously existing gas pressure maximum, which allows even more dust to become trapped and enhance the pressure maximum even further.

Their suggestion of a new mechanism to form dust traps has interesting implications for planetesimal formation. Thus, we decided to explore it, which required the implementation dust-gas models in our own SPH programs. Our collaborators Isaac Backus and Tom Quinn at the University of Washington have already begun this work in the highly parallelized SPH code ChaNGa (Menon et al. 2015) which is built upon the same physics algorithms as Gasoline2 (Wadsley et al. 2017). They had developed a module for simulating dust according to the one-fluid prescriptions (see Section 2.2). We decided to try and use this module to explore the results of Gonzalez et al. (2017) by adapting the code to include the grain growth algorithms described in the Gonzalez et al. (2017) study.

We discovered that the one-fluid scheme is overly diffusive. This diffusion is a numerical effect, and artificially limits the ability of the dust mass to clump into high densities. Also, the one-fluid scheme is best suited for tracking small grains, where the relative velocities between the dust fluid and the gas fluid is small. The physical consequences of the Gonzalez et al. (2017) simulations rely on the ability of the dust to form overdense regions and for the simulation to be able to track the dynamics of large solid bodies. Thus, we decided we required a two-fluid dust module in ChaNGa, which was the prescription employed in Gonzalez et al. (2017).

We will begin this chapter with a brief introduction to SPH. We will then discuss how the one-fluid prescription can be implemented in an SPH formalism, including the Gonzalez et al. (2017) grain growth model, and a simple test of the algorithm. We will then discuss the implementation of the two-fluid prescription, and the results of some tests that reveal the difficulties in using this model to simulate the behaviour of the dust fluid in full protoplanetary disks.

3.1 Smoothed Particle Hydrodynamics (SPH)

SPH is a numerical particle method for solving the hydrodynamics equations. It is a Lagrangian method, meaning the equations are solved in the frame of a particle moving with the fluid. A thorough review of the fundamentals of SPH and early SPH work is available in Monaghan (1992), and more a recent overview, including a discussion on

magnetohydrodynamics in SPH, is available in Price (2012).

The fundamental numerical calculation in SPH is the smoothed estimate for physical quantities at the particle location. The simplest example is the density estimator. For a particle identified with the subscript a, the estimate is a weighted sum over the masses of the "neighbours" of a,

$$\rho_a(\boldsymbol{r}) = \sum_{b=1}^{N_{neigh}} m_b W(\boldsymbol{r_a} - \boldsymbol{r}_b, h) \tag{3.1}$$

where the subscript b represents each of the individual neighbours, and there are a total of N_{neigh} neighbours. $W(\boldsymbol{r}_a - \boldsymbol{r}_b, h)$ is the SPH kernel function. For this derivation, the exact details of the functional form of the kernel are not important, but we note that it must be a positively-valued function, properly normalized, and Gaussian-like: spherically symmetric with respect to $(\boldsymbol{r_a} - \boldsymbol{r}_b)$ and spatially localized.

The parameter h is the SPH smoothing length, which is a measure of the local numerical resolution and can be estimated in many ways. In the SPH algorithms in GASOLINE and CHANGA, each SPH particle has the same number of neighbours N_{neigh}, and the value of h for each particle will be such that N_{neigh} particles are encompassed by the domain of W. Outside of the domain of W, the kernel function is identically zero.

With this density estimate, we can create an SPH estimator of the acceleration due to the hydrodynamic force, $-\nabla P_g/\rho_g$ (equation 2.5b). The expression for this force in GASOLINE2 is,

$$\frac{\mathrm{d}\boldsymbol{v}_a}{\mathrm{d}t} = -\sum_b m_b \Big(\frac{P_a + P_b}{\rho_a \rho_b}\Big) \nabla_a \bar{W}_{ab}(h_a) \tag{3.2}$$

where $\nabla_a \bar{W}_{ab}$ represents a symmetrized kernel gradient,

$$\nabla_a \bar{W}_{ab} = \frac{1}{2}\Big(f_a \nabla_a W(r_{ab}, h_a) + f_b \nabla_b W(r_{ab}, h_b)\Big) \tag{3.3}$$

where f_a is a correction term of order unity which applies when the smoothing length h is not constant (c.f. Wadsley et al. (2017)).

Note, equation 3.2 does not include the artificial viscosity term, which is adds numerical dissipation to provide numerical stability when the code encounters discontinuities with widths that are smaller than the resolution scale (c.f. Wadsley et al.

(2017)).

3.2 One fluid dust and gas in SPH

The one fluid dust-gas model requires the quantities ϵ, ρ, $\boldsymbol{V}_{bc}$, and $\boldsymbol{w}$ to be tracked by the SPH particles, which now explicitly represent a mixed mass of dust and gas. The dynamics that govern the motion of these particles are different from gas-only SPH as well (see section 2.2).

Here, we will only provide an SPH representation of the evolution of the dust to total mass fraction ϵ (equation 2.9),

$$\frac{\mathrm{d}\epsilon_a}{\mathrm{d}t} = -\sum_b m_b \Big(\frac{\epsilon_a(1-\epsilon_a)}{\Omega_a \rho_a} \boldsymbol{w}_a \cdot \nabla_a W_{ab}(h_a) + \frac{\epsilon_b(1-\epsilon_b)}{\Omega_b \rho_b} \boldsymbol{w}_b \cdot \nabla_b W_{ab}(h_b) \Big) \tag{3.4}$$

Where Ω_a is similar to f_a in equation 3.2 and is a term related to the gradient of the smoothing length. With this expression for $\mathrm{d}\epsilon_a/\mathrm{d}t$, the mass of dust in the simulation is conserved:

$$\frac{\mathrm{d}M_d}{\mathrm{d}t} = \sum_a m_a \frac{\mathrm{d}\epsilon_a}{\mathrm{d}t} = 0 \tag{3.5}$$

3.2.1 Variable grain size

Many of the results presented in the Gonzalez et al. (2017) study depend on their inclusion of a variable grain size model in their simulation. The size of the dust grains dictates the strength the of the drag interactions between the dust and the gas, as the drag coefficient K and consequently the drag stopping time t_s both depend on the grain size (see equations 2.3 and 2.6). Global dust and gas interactions in protoplanetary disks can vary wildly depending the size of the dust grains involved. Hence, simulations that include a model that permits this parameter to be a variable can potentially reveal details about early planet formation that simulations with static grain sizes cannot.

We developed the capability to include variable grain sizes in ChaNGa, and in this section we outline the two main components of this model.

3.2.2 Local grain growth and destruction

Stepinski and Valageas (1996) present a simple model for grain growth via coagulation that occurs below the numerical resolution scale, and Gonzalez et al. (2017) expand the model to include the potential for this grain size parameter to decrease due to destructive collisions. Since this action occurs below the resolution scale or within the SPH particle, we will refer to it as a "local" effect. The derivatives that guide this local change in the grain size s are,

$$\left.\frac{ds}{dt}\right|_{local} = \begin{cases} +\epsilon\frac{\rho}{\rho_{grain}}V_{rel} & V_{rel} < V_{frag} \\ -\epsilon\frac{\rho}{\rho_{grain}}V_{rel} & V_{rel} > V_{frag} \end{cases} \tag{3.6}$$

where ρ_{grain} is the intrinsic bulk density of the dust grain, $\rho \equiv \rho_d + \rho_g$ and $\epsilon \equiv \rho_d/\rho$ as in Section 2.1 and Section 2.2. V_{rel} is another sub-resolution parameter that describes the average relative velocity between the dust grains themselves, created by gas turbulence. From Stepinski and Valageas (1996), this parameter is of the form,

$$V_{rel} = \sqrt{2\tilde{\alpha}}\frac{\sqrt{\tau_s}}{1+\tau_s}c_s \tag{3.7}$$

where $\tilde{\alpha} \equiv \sqrt{2}\text{Ro}\ \alpha_{ss}$ and α_{ss} is the Shakura & Sunyaev viscosity parameter (Shakura and Sunyaev 1973), Ro is the Rossby number, c_s is the gas sound speed and τ_s is the dimensionless stopping time parameter (equation 1.1).

The Rossby number represents the ratio of the strength of the centrifugal force to the strength of the Coriolis force. For $\text{Ro} \gg 1$, the Coriolis force does not significantly alter motions of the gas from the global rotational flow in the disk, and for $\text{Ro} \ll 1$ the Coriolis force dominates the local motions of the gas (Zeytounian 1991). The intermediate regime is marked by $\text{Ro} \sim 1$, and Stepinski and Valageas (1996) emphasizes as minimum we must have $\text{Ro} > 3/2$ for this local, sub-grid turbulence model to be self-consistent.

The parameter α_{ss} is a dimensionless parameter that characterizes the efficiency of angular momentum transport due to turbulent motions in gaseous disks. In the context of protoplanetary disks, this parameter can be used to construct a turbulent viscosity from dimensional arguments. Following Armitage (2013), we can note the largest length scale for the turbulent motions is the vertical gaseous scale height, H_g. Secondly, the speed of the turbulent motions are subsonic, so the largest velocity would

be the sound speed c_s. Thus a turbulent viscosity ν can be defined as,

$$\nu = \alpha_{ss} c_s H_g \tag{3.8}$$

and in this expression α_{ss} is between 10^{-2} and 10^{-4} depending on the disk model used.

The parameter V_{frag} determines the boundary where collisions are either destructive or constructive. In reality this value would depend on the composition and structural integrity (porous, icy) of the dust grains. Gonzalez et al. (2017) explore various values of V_{frag} in their simulation to determine the effects it has on the results.

From section 2.1 we have $\tau_s \propto s_d$ in the Epstein drag regime. This gives $V_{rel} \propto \sqrt{s_d}/(1 + s_d)$ (holding gaseous properties constant). The form of equation 3.6 guides the dust grains in the simulation towards a state where $V_{rel} = V_{frag}$. In the Epstein drag regime, where $V_{rel} \propto \sqrt{s_d}/(1 + s_d)$, this means growing or fragmenting towards one of two specific grain sizes that will satisfy $V_{rel} = V_{frag}$. This idea is explored in Appendix A of Gonzalez et al. (2017), and the resulting expression that describes these grain sizes s_{frag} are,

$$s^{\pm}_{frag} = s_{drift}\left[\frac{\tilde{\alpha}{c_s}^2}{{V_{frag}}^2} - 1 \pm \frac{\sqrt{\tilde{\alpha}}c_s}{V_{frag}}\sqrt{\frac{\tilde{\alpha}{c_s}^2}{{V_{frag}}^2} - 2}\right] \tag{3.9}$$

where $s_{drift} = \rho_g c_s/(\rho_{grain}\Omega)$ is the grain size for $\tau_s = 1$, Ω is the orbital angular velocity of the grains.

For a protoplanetary disk with a vertical (out of midplane) Gaussian density profile characterized by the scale height, H_g, the midplane gas density is given by,

$$\rho_g\big|_{midplane} = \frac{1}{\sqrt{2\pi}}\frac{\Sigma}{H_g}$$

Note $H_g \equiv c_s/\Omega$. Thus for a radial surface density profile given by a power law $\Sigma_g = \Sigma_0(r/r_0)^{-1}$, we have,

$$s_{drift} = 46 \text{ cm } \left(\frac{\Sigma_0}{300 \text{ g cm}^{-2}}\right)\left(\frac{\rho_{grain}}{2.6 \text{ g cm}^{-3}}\right)^{-1}\left(\frac{r}{r_0}\right)^{-1} \tag{3.10}$$

Since s_{drift} and c_s depend on disk conditions, for protoplanetary disks where density and temperature are a function of radius from the central star, the values for s_{frag} also change with radius. In Appendix A, Gonzalez et al. (2017) plot s_{frag} and s_{drift}

for the two disk models they studied, and their Figure A1 is provided here below in Figure 3.1.

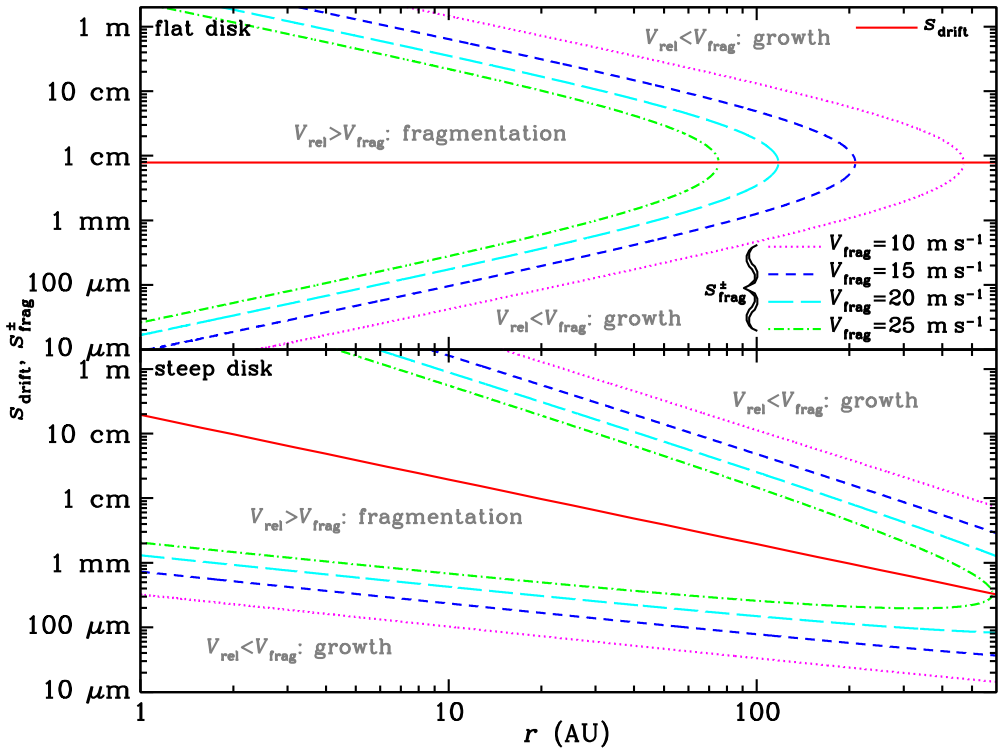

Figure 3.1: Radial profiles for s_{frag} and s_{drift} in the initial conditions of the simulated protoplanetary disks studied by Gonzalez et al. (2017), reproduced with permission. The top panel is for a flat disk, where the surface density does not change with radius, and the bottom panel is for a disk where the surface density scales with r^{-1}.

As labelled in both panels in Figure 3.1, grains with sizes below and above the parabolic curves grains will grow, and for grain sizes in the middle of the parabolic curves grains will fragment. Thus grains below the top half of the curves will attempt to reach the size described by the bottom curve, and grains outside of the radial extent of the curves or above the top half of the curves will grow indefinitely, albeit at a decreasing rate since for large grains with large values of τ_s, the local growth rate (equation 3.6) scales as ${\tau_s}^{-1/2}$.

3.2.3 Advection of grain size for one-fluid SPH

In a one-fluid SPH model, when the dust-gas mixture particle exchanges dust mass with its neighbours as in equation 3.4, the grain size parameter should be modified accordingly.

We can simply modify the grain size to be an average of the grain sizes from the SPH neighbours that each particle exchanges dust mass with, and weight the neighbour sizes by the amount of dust being exchanged in each interaction. For a particle a with a list of neighbours described by the subscript b, this looks like,

$$s'_a = \frac{m_{d,a} s_a + \sum_b \Delta m_{d,<ab,ba>} s_{<a,b>}}{m_{d,a} + \sum_b \Delta m_{d,<ab,ba>}} \tag{3.11}$$

where s'_a is the value of grain size for particle a on the next time step.

The subscript notation $< ab, ba >$ and $< a, b >$ signifies that the particular dust mass or grain size that should be used in the sum depends on whether particle a is giving dust to b, or particle b is giving dust to a.

That is, the grain size that should appear in the weighted sum depends on the direction of the exchanged dust mass. If a is receiving dust from a neighbour b, then the sign of the exchanged dust mass, Δm_d, will be positive: a's dust mass is increasing. In other words, the direction of dust mass transfer is from b to a, so the grain size that should be used in the sum is s_b. We represent the weighted sum of such a transfer as $\Delta m_{d,ba} s_b$. In the opposite scenario, dust is travelling from a to b, so the grain size that needs to be used in this transfer is s_a. Similarly, we represent this transfer with $\Delta m_{d,ab} s_a$. Thus we can split the sum in equation 3.11 into two different sums, one for each of the directions of transfer. This equation becomes,

$$s'_a = \frac{m_{d,a} s_a - \sum_b |\Delta m_{d,ab}| s_a + \sum_b \Delta m_{d,ba} s_b}{m_{d,a} - \sum_b |\Delta m_{d,ab}| + \sum_b \Delta m_{d,ba}} \tag{3.12}$$

and we have written $\Delta m_{d,ab}$ as $-|\Delta m_{d,ab}|$ to emphasize that this is a negative value.

When implementing this weighted sum in our one-fluid dust & gas SPH code, we note that the mass of the dust on each particle $m_{d,a}$ is not explicitly evolved, but the dust mass to total mass fraction ϵ is. The dust mass that exists on a particle can be represented by $\epsilon_a m_a$ where m_a is the SPH particle mass, which represents a combined

dust and gas mass in this formalism. Thus,

$$\Delta m_{d,ab} = \Delta\epsilon_{ab} m_a$$

To compute a $\Delta\epsilon$ in code, we first compute an SPH time derivative for ϵ, $\mathrm{d}\epsilon/\mathrm{d}t$ (as in equation 3.4), which we will relabel here as $\dot{\epsilon}$. We then integrate ϵ forward by one timestep, Δt, to get $\Delta\epsilon$. Explicitly,

$$\Delta m_{d,ab} = \Delta\epsilon_{ab} m_a = \left.\frac{\mathrm{d}\epsilon}{\mathrm{d}t}\right|_{ab} m_a \Delta t = \dot{\epsilon}_{ab} m_a \Delta t \tag{3.13a}$$

where the notation $\dot{\epsilon}_{ab}$ signifies that dust mass is being transferred from particle a to its neighbours b, via a change in ϵ. Similarly, we have,

$$\Delta m_{d,ba} = \dot{\epsilon}_{ba} m_a \Delta t \tag{3.13b}$$

substituting equations 3.13 into equation 3.11 and rearranging gives,

$$s'_a = \frac{(\epsilon_a - \sum_b |\dot{\epsilon}_{ab}|) s_a \Delta t + (\sum_b \dot{\epsilon}_{ba} s_b)\Delta t}{(\epsilon_a - \sum_b |\dot{\epsilon}_{ab}|\Delta t) + \sum_b \dot{\epsilon}_{ba}\Delta t} \tag{3.14}$$

3.2.4 Enforcing physical ranges for dust fraction values

In our one-fluid dust-gas implementation in CHANGA, we have not added an appropriate dust-physics based time stepping criterion (c.f. Section 2.3) that would ensure the numerical stability of the integration for the dust mass fraction ϵ. In neglecting to include this times stepping criterion, ϵ is free to approach non-physical values when integrated forward in time, such as any value below 0 or above 1. In full protoplanetary disk simulations, the values for ϵ in the inner parts of the disk, where the typical variance of density, temperature, etc. between an SPH particle and its neighbours is small, the integration for ϵ remains stable. Recall from equation 3.4 that the SPH time derivative for ϵ is,

$$\frac{\mathrm{d}\epsilon_a}{\mathrm{d}t} = -\sum_b m_b \left(\frac{\epsilon_a(1-\epsilon_a)}{\Omega_a \rho_a} \boldsymbol{w}_a \cdot \nabla_a W_{ab}(h_a) + \frac{\epsilon_b(1-\epsilon_b)}{\Omega_b \rho_b} \boldsymbol{w}_b \cdot \nabla_b W_{ab}(h_b) \right)$$

We can note that the value $\mathrm{d}\epsilon_a/\mathrm{d}t$ will take is a weighted average of $\epsilon_{<a,b>}(1-\epsilon_{<a,b>})$. Thus if the values of ϵ amongst the particle a and its neighbours b are similar, then the

value of the derivative will be within an acceptable range such that ϵ_a remains stable.

However, at the boundaries of the disk the variance in the densities is much larger. To compound this issue, $\mathrm{d}\epsilon_a/\mathrm{d}t$ scales inversely with $\rho_{<a,b>}$, and the densities at the edges of the disk are the lowest densities in the simulation. This means $\mathrm{d}\epsilon_a/\mathrm{d}t$ is free to approach a very large value, and if the timestep is not appropriately limited, ϵ will step beyond physically realistic bounds.

For protoplanetary disk simulations that only span a few dynamical times, this effect will not impact the simulation domain in the regions that are far away from the disk edges. This does tell a cautionary tale, however, for studies that use simulations that span many dynamical times, and those whose results depend on physics that occurs on the outer edge of the disk, such as the previously mentioned paper by Gonzalez et al. (2017).

As a fix for ϵ approaching non-physical values less than 0 or greater than 1, we set a hard-coded floor and ceiling for ϵ. If the value for ϵ at the end of the integration was outside of the acceptable range, it was simply set to the value at the appropriate boundary[1]. This of course invalidates the dust mass conservation that was otherwise guaranteed by the form of equation 3.4.

An obvious solution to this issue would be to come up with an appropriate timestepping criterion for $\mathrm{d}\epsilon_a/\mathrm{d}t$, as is done with many other derivatives in the simulation suite. Unfortunately, this would have dire consequences for the computation time of the simulation, as the temporal integration of the simulation could potentially be limited by the dust physics that occurs at the edge of the simulation domain, where the numerical resolution is poor and the physics should not be trusted.

A better solution would be to write an alternative form for $\mathrm{d}\epsilon_a/\mathrm{d}t$ that remains conservative, yet avoids this numerical instability. For this purpose we investigated a so-called upwinding scheme for ϵ, and the results of this investigation are presented in the following section.

[1]The floor we use is not actually 0, as the computation for the advected grain size (equation 3.14) scales with ϵ^{-1}. Hence we use a small, finite value near machine precision such as 10^{-6}.

3.2.5 Upwinding

From section 3.2, the SPH derivative for the evolution of the dust mass fraction ϵ in the one-fluid scheme is,

$$\frac{\mathrm{d}\epsilon_a}{\mathrm{d}t} = -\sum_b m_b \Big(\frac{\epsilon_a(1-\epsilon_a)}{\Omega_a \rho_a} \boldsymbol{w}_a \cdot \nabla_a W_{ab}(h_a) + \frac{\epsilon_b(1-\epsilon_b)}{\Omega_b \rho_b} \boldsymbol{w}_b \cdot \nabla_b W_{ab}(h_b) \Big)$$

Through the symmetry of the SPH kernel (equation **??**), we can rewrite this as,

$$\frac{\mathrm{d}\epsilon_a}{\mathrm{d}t} = -\sum_b m_b \Big(\frac{\epsilon_a(1-\epsilon_a)}{\Omega_a \rho_a} \boldsymbol{w}_a \cdot \nabla_a W_{ab}(h_a) - \frac{\epsilon_b(1-\epsilon_b)}{\Omega_b \rho_b} \boldsymbol{w}_b \cdot \nabla_a W_{ba}(h_b) \Big)$$

For this section we will rename the second parts of each term to clean up the notation. We will define two terms, G_a and G_b,

$$G_a = \frac{(1-\epsilon_a)}{\Omega_a \rho_a} \boldsymbol{w}_a \cdot \nabla_a W_{ab}(h_a) \; ; \; G_b = \frac{(1-\epsilon_b)}{\Omega_b \rho_b} \boldsymbol{w}_b \cdot \nabla_a W_{ba}(h_b) \tag{3.15}$$

so that we now have, for a single exchange between particle a and one of its SPH neighbours b, the dust fraction derivative $\dot{\epsilon}_{ab}$ is,

$$\dot{\epsilon}_{ab} = -m_b \Big(\epsilon_a G_a - \epsilon_b G_b \Big) \tag{3.16}$$

It is apparent in this form that this exchange in dust mass fractions is a weighted sum of the dust fractions for each particle, ϵ_a and ϵ_b, where the weights are G_a and G_b.

Instead of averaging the two dust fractions, however, we can instead use an upwinding scheme (Laney 1998) when computing this derivative. As explored in the previous discussion in section 3.2.3 concerning the transfer of the grain size property s when dust mass is exchanged, here, we can reconstruct $\dot{\epsilon}_{ab}$ so that the dust mass ($m_a \epsilon_a$) that is used when computing the derivative will depend on the sign the derivative, or the direction that dust is being transferred between particles,

$$\dot{\epsilon}_{ab} = \begin{cases} -\epsilon_b m_b (G_a - G_b), & \text{if } G_a - G_b < 0 \\ -\epsilon_a m_a (G_a - G_b), & \text{if } G_a - G_b > 0 \end{cases} \tag{3.17}$$

In the top case, $\dot{\epsilon}_{ab}$ is positive valued, so a is receiving dust from b and $\epsilon_b m_b$ is used, and in the bottom case $\dot{\epsilon}_{ab}$ is negative, a is losing dust mass to b, so $\epsilon_a m_a$ is used.

We tested each of the two schemes against a simple settling test, which is designed to mimic the action of dust settling to the midplane of a protoplanetary disk from an initially disperse distribution. A collection of one-fluid dust-gas SPH particles was distributed so that a Gaussian density profile in the z-direction was created, and a gravitational acceleration in z towards the midplane was applied. Each particle was given an initial value of $\epsilon = 0.099$, the size of the dust grain are such that $\tau_s \ll 1$, and as the simulation starts, the dust mass—tracked by ϵ—falls towards the $z = 0$ midplane.

In Figure 3.2, we can see a comparison between the shape of the collapsing dust fraction feature over time. The shape in the upwinding scheme is notably smoother than in the original scheme, which we will call the arithmetic mean scheme. The peak is not as high in the upwinding scheme in the final frame, and the sharp, edge features that exist in the arithmetic scheme are not as pronounced in the upwinding scheme. The upwinding scheme is certainly more diffusive.

Importantly, the upwinding scheme conserves dust mass much better than the arithmetic mean scheme with the hard-coded floor and ceiling discussed in the previous section, as can be seen in Figure 3.3.

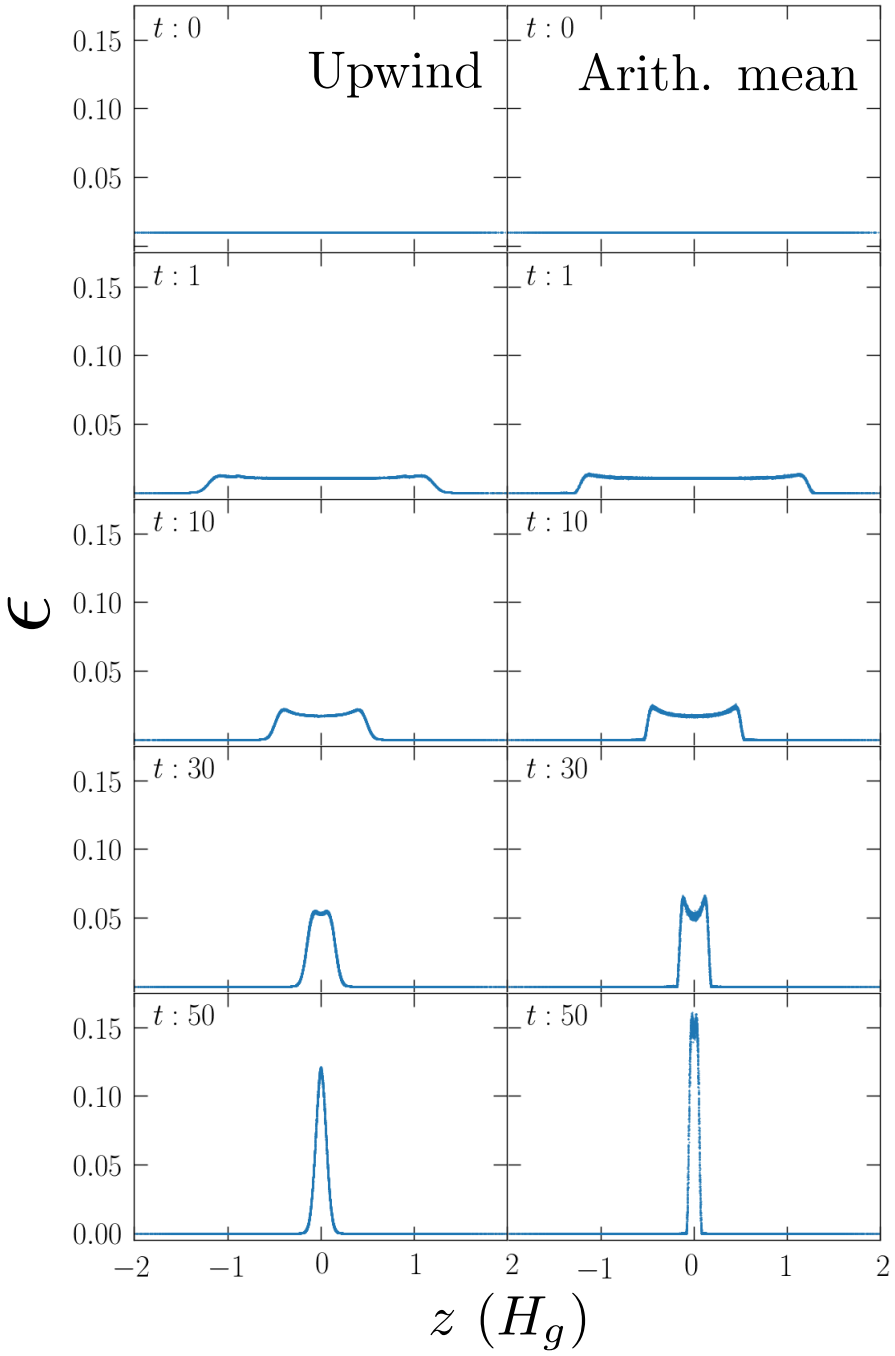

Figure 3.2: Vertical distribution of dust mass fraction ϵ from the dust settling test. The results using the upwinding scheme (equation 3.17) are in the left panels, and the results from the arithmetic average scheme (3.4) are in the right panels. The numbers inset in each panel represent the elapsed time in the simulation in units of the Keplerian orbital period. The data for the vertical position of the dust is in units of the vertical gas scale height.

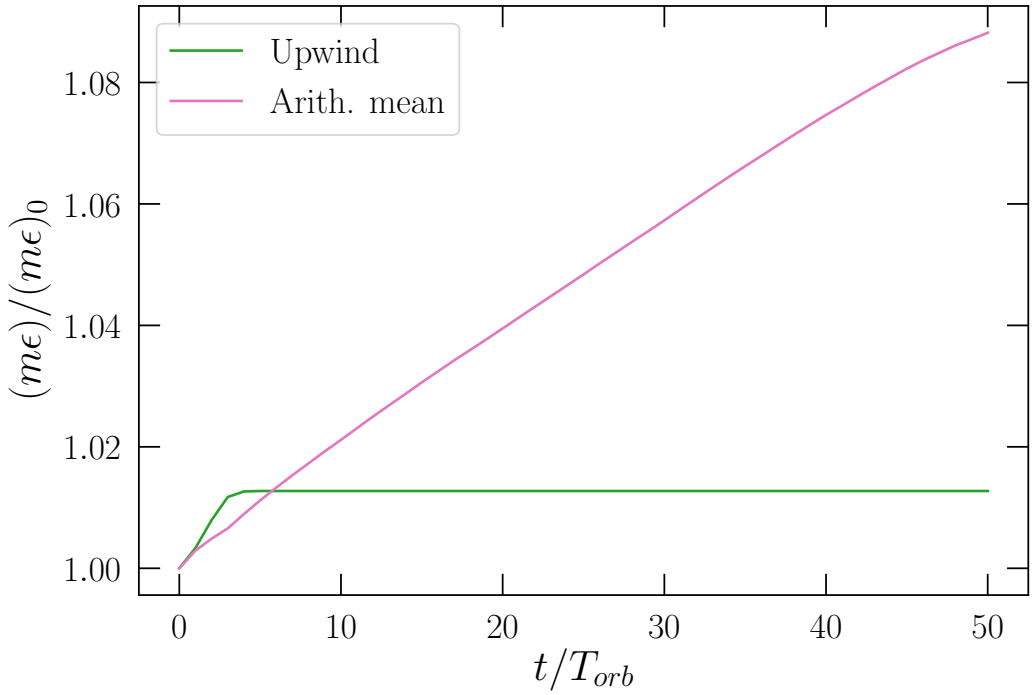

Figure 3.3: Conservation of dust mass $m\epsilon$ in the upwinding and arithmetic average scheme. The y-axis represents the total sum of all the dust mass in the simulation, scaled by the total dust mass in the initial condition.

3.3 Two fluid dust and gas in SPH

To incorporate the two fluid dust-gas model (section 2.1) into an SPH code, another species of SPH particles for the dust fluid must be created. The dust species and the ordinary SPH gas species would obey different equations of motion and their own continuity equation (see equations 2.5).

The primary step to developing an SPH representation of the two-fluid model involves creating an appropriate expression for the drag term (equation 2.2). We can write down a simple expression which smooths the drag force with a sum weighted by the kernel W_{ai}. For the gas particles, this would look like,

$$\left(\frac{\mathrm{d}\boldsymbol{v}_a}{\mathrm{d}t}\right)_{drag} = \frac{K}{\rho_g}(\boldsymbol{v}_d - \boldsymbol{v}_g) = \nu \sum_i m_i \frac{K_{ai}}{\rho_a \rho_i}(\boldsymbol{v}_i - \boldsymbol{v}_a) W_{ai}(h_a) \tag{3.18}$$

where ν is the number of spatial dimensions in the system. K_{ai} is the drag constant (e.g. equation 2.3), which in general depends on properties of the gas particle a or the

dust particles i.

In this expression, and in all other expressions in this subsection, we will denote quantities belonging to gas particles with a, and quantities belonging to dust particles with i. Thus equation 3.18 states that the drag acceleration on the gas particle a involves a sum over only its dust particle neighbours, identified with the subscript i, and not any of gas particle neighbours.

However, equation 3.18 does not conserve angular momentum. An alternate expression for the gas acceleration due to drag that does conserve angular momentum can be written as (Monaghan and Kocharyan 1995),

$$\left(\frac{\mathrm{d}\boldsymbol{v}_a}{\mathrm{d}t}\right)_{drag} = \frac{K}{\rho_g}(\boldsymbol{v}_d - \boldsymbol{v}_g) = \nu \sum_i m_i \frac{K_{ai}}{\rho_a \rho_i}\big(\boldsymbol{w}_{ia} \cdot \hat{\mathbf{r}}_{ia})\hat{\mathbf{r}}_{ia} D_{ai}(h_a) \tag{3.19a}$$

For the dust particles, this looks like,

$$\left(\frac{\mathrm{d}\boldsymbol{v}_i}{\mathrm{d}t}\right)_{drag} = -\frac{K}{\rho_d}(\boldsymbol{v}_d - \boldsymbol{v}_g) = -\nu \sum_a m_a \frac{K_{ai}}{\rho_a \rho_i}\big(\boldsymbol{w}_{ia} \cdot \hat{\mathbf{r}}_{ia})\hat{\mathbf{r}}_{ia} D_{ai}(h_a) \tag{3.19b}$$

Where $\boldsymbol{w}_{ia} \equiv \boldsymbol{v}_i - \boldsymbol{v}_a$ and $\hat{\boldsymbol{r}}_{ia} \equiv (\boldsymbol{r}_i - \boldsymbol{r}_a)/|\boldsymbol{r}_i - \boldsymbol{r}_a|$, i.e. the radial unit vector is oriented to point from the gas particle to the dust particle, and the drag force now points along the direction of $\hat{\boldsymbol{r}}_{ia}$. Note when acting on the gas particle, the drag acceleration points in the direction of $\hat{\boldsymbol{r}}_{ia}(\boldsymbol{w}_{ia} \cdot \hat{\mathbf{r}}_{ia})$, and when acting on the dust particle, the accelerations points in the direction of $-\hat{\boldsymbol{r}}_{ia}(\boldsymbol{w}_{ia} \cdot \hat{\mathbf{r}}_{ia})$.

Figure 3.4 presents an example outlining the difference between these two formulations for the drag.

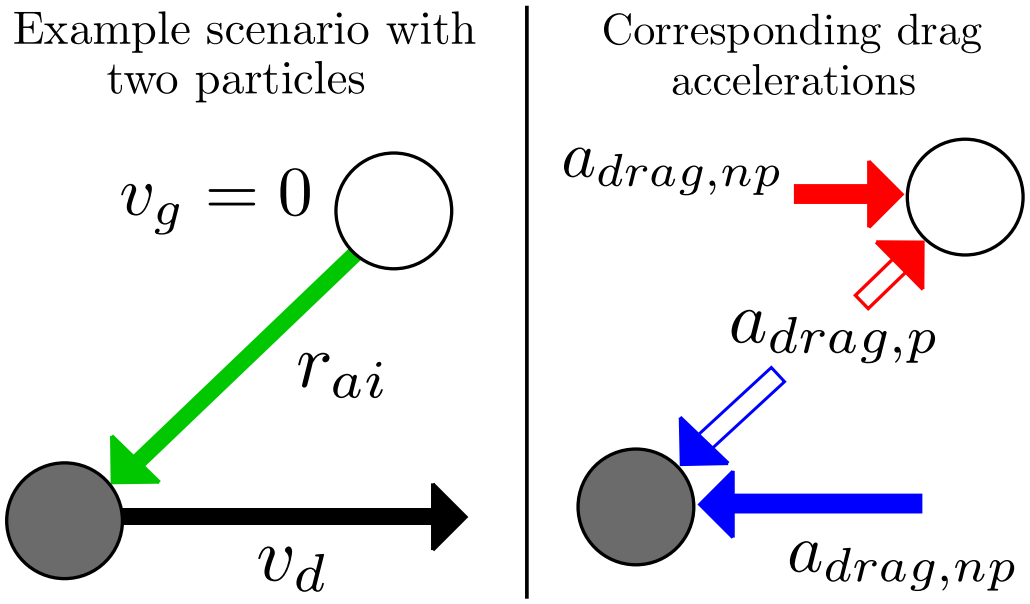

Figure 3.4: A graphical description of the two different forms for the SPH version of the drag term from equations 3.18 and 3.19. In the left frame, a gas particle is shown as a white circle, and a dust particle is shown as a grey circle. The vector r_{ia} which points from the gas particle to the dust particle is shown in green. We impart a velocity on the dust particle towards the right, and the gas particle has no velocity. In the right frame, the drag acceleration imparted on each particle in the non-projected form in equation 3.18 (subscript np) is represented by the solid arrows, and the projected drag, equations 3.19 is represented by the unfilled arrows.

In the drag force prescription from equations 3.19 which conserves angular momentum, the drag force is projected along $\hat{\boldsymbol{r}}_{ia}$. This projected drag acceleration points in a fundamentally different direction from the non-projected prescription, which in the SPH formalism of equation 3.18 does not conserve angular momentum and is oriented in the direction of $\boldsymbol{v}_d - \boldsymbol{v}_g$. Thus, from the perspective a dust particle moving through a cloud of gas, the weights in the sum from equations 3.19 are a maximum for gas particles whose positions are aligned with the velocity of the dust and vanish to zero for gas particles that are perpendicular to the dust velocity. There exists a choice between the model where the direction of the drag force is correct (equation 3.18) or the model where angular momentum is conserved (equations 3.19). Our implementation and that of Laibe and Price (2012) uses the projected prescription which conserves angular momentum. Presumably for a simulation involving many particles the errors introduced by the fact our chosen drag force does not point in the

direction of $\boldsymbol{v}_d - \boldsymbol{v}_g$ will be small and average to zero and not affect the macroscopic results of the simulation.

The final detail to note is the change in notation for the SPH kernel in equations 3.19. The kernel is written as D_{ai} instead of W_{ai} as it was before. Laibe and Price (2012) argue that the kernel used to the smooth the drag force should be different from the standard SPH kernels in order to reduce errors. The details concerning these kernels are available in Laibe and Price (2012).

3.3.1 Radial Drift Test of Two-Fluid Dust in SPH

In order to test numerical codes, the standard practice is to design a simulation where the behaviour of the quantities tracked by the simulation is known analytically. For instance, Laibe and Price (2012) (two fluid) and Laibe and Price (2014a) (one fluid) discuss a"dustywave" and "dustyshock" tests for dust-gas algorithms in SPH. The dustyshock test is an adaptation of the Sod shock tube test (Sod 1978), a widely used test for numerical fluid dynamics algorithms. The shock tube test subjects the numerical suite to discontinuities in fluid properties (density, pressure, velocity) with the objective of observing how accurately the method treats these discontinuities, which in general are difficult for discrete methods with finite resolution to handle. The dustywave test is useful for ensuring the numerical suite produces the appropriate behaviour for dust of different drag coupling strengths.

While the above tests are useful for ensuring an implementation of dust-gas algorithms has been written correctly and offer some insight into how well the algorithms perform in difficult scenarios, we believe they do not provide an honest demonstration of how the numerical suite performs in practical scenarios, such as a protoplanetary disk.

Hence, we devised a radial dust drift test, meant to determine how well the numerical suite is able to reproduce the expected inward radial drift rates of dust particles embedded within a full protoplanetary disk. Following section 4.3 of Armitage (2013), the analytical drift rates can be derived as follows:

Dust particles in a protoplanetary disk obey the following equations of motion,

$$\frac{\mathrm{d}v_r}{\mathrm{d}t} = \frac{{v_\theta}^2}{r} - \Omega^2 r - \frac{1}{t_s}(v_r - v_{r,gas}) \tag{3.20}$$

$$\frac{\mathrm{d}}{\mathrm{d}t}(rv_\theta) = -\frac{r}{t_s}(v_\theta - v_{\theta,gas}) \tag{3.21}$$

where v_r and v_θ are the radial and azimuthal velocities, respectively, of the dust particles, $v_{r,gas}$ and $v_{\theta,gas}$ are the same quantities but for the gas, Ω is the Keplerian angular velocity, t_s is the stopping time (see equation 2.6), and r is the radial coordinate. Radial velocities in this description are positive for motions towards the outside of the disk, away from the star. The radial velocity of the gas due to viscous effects is (Lynden-Bell and Pringle (1974), Birnstiel et al. (2010)),

$$v_{r,gas} = -\frac{3}{\Sigma_g\sqrt{r}}\frac{\partial}{\partial r}\left(\Sigma_g\nu_g\sqrt{r}\right) \tag{3.22}$$

where Σ_g is the gas surface density and ν_g is the gas viscosity. Note that the product $\Sigma_g\nu_g\sqrt{r}$ is, on average, a decreasing function of radius, so that overall $v_{r,gas}$ is positive, and the radial motion of the gas is away from the star.

If we recognize that deviations for the dust particles from circular, Keplerian orbits will be small, and that the $\mathrm{d}v_r/\mathrm{d}t$ term on the left side of equation 3.20 is also negligible, than we can say,

$$v_r = \frac{{\tau_s}^{-1}v_{r,gas} - \eta v_K}{\tau_s + {\tau_s}^{-1}} \tag{3.23}$$

where v_K is the Keplerian azimuthal velocity, $\tau_s = t_s\Omega$ as before, and

$$\eta = n\left(\frac{c_s}{v_K}\right)^2 \tag{3.24}$$

If we assume the midplane gas pressure in the protoplanetary disk can be written as a power law in radius, then n is the exponent in the that power law, $P \propto r^{-n}$. The parameter η measures how much the azimuthal velocity of the gas deviates from the expected Keplerian rotational velocity due to the pressure gradient that points in the outwards radial direction,

$$v_{\theta,gas} = v_K(1-\eta)^{1/2} \tag{3.25}$$

A plot of $-v_r/v_k$ as a function of τ_s is shown in Figure 3.5, which matches Figure 4.2 from Armitage (2013). This shows that the velocity of the inward radial drift is a strongly peaked function of τ_s, and peaks for dust grains of the size that gives $\tau_s = 1$.

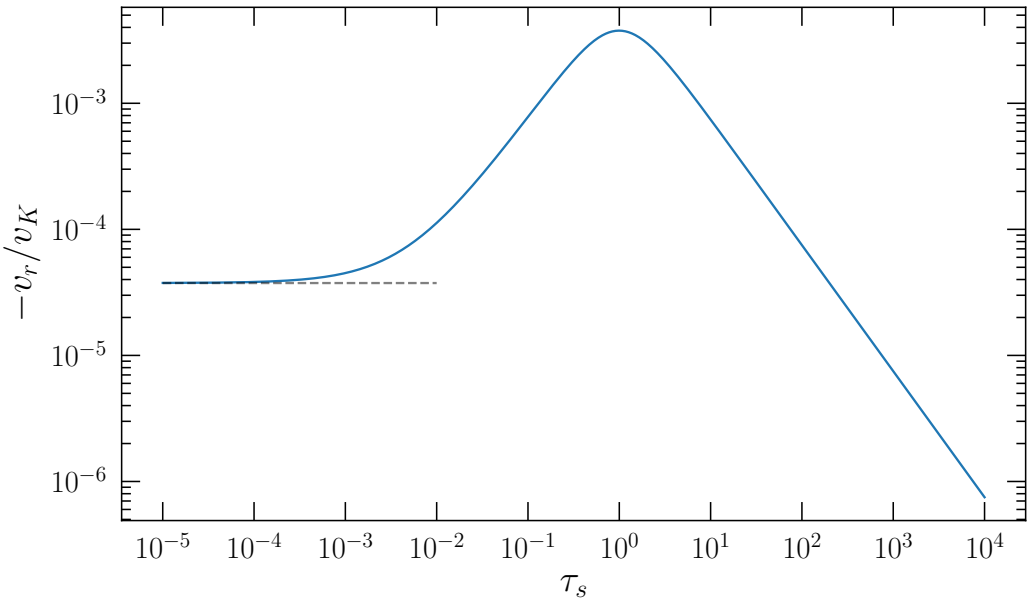

Figure 3.5: Velocity of the radial of drift of dust particles as described by equation 3.23, results match Figure 4.2 from Armitage (2013). Here we use $\eta = 7.5 \times 10^{-3}$ and $v_{r.gas}/v_K = -3.75 \times 10^{-5}$. The dashed line is the value for $v_{r.gas}/v_K$, and is provided to show that radial velocity the dust tracks the radial velocity of the gas for small τ_s.

We tested the ability of our two-fluid dust-gas implementation in CHANGA to produce the expected radial drift velocity of equation 3.23. Our simulation consisted of a protoplanetary disk with a 1 solar mass star at the centre, and 10^5 SPH gas particles comprising a 5×10^{-3} solar mass gaseous disk orbiting it. The gaseous disk has a surface density profile $\Sigma_g \propto r^{-1}$ and the inner radial boundary was 5 AU and the outer radial boundary was 200 AU initially.

In the initial condition, 1000 SPH dust particles (individually with a mass that was a factor of 10^{-6} less than the gas particle masses so that they did not impart much momentum on the gas) were evenly dispersed in the midplane of the gaseous disk around a ring of radius 20 AU centred on the star.

The positions of these dust particles in the rotational $(x - y)$ plane of the disk over the course of the simulation are shown in Figure 3.6. Simulations from two different sizes of dust grains are shown. We can see that in only a few orbital times, the ring of dust rapidly loses its shape, and breaks off into scattered clumps.

We chose to simulate 1000 dust particles so that well defined averaged properties can be investigated. For the $\tau_s = 1$ simulation, the radial velocity of the dust particles,

v_r, is shown in Figure 3.7, and the radius of the dust particles, r, is shown in Figure 3.8.

There is a large dispersion in both v_r and r for the $\tau_s = 1$ simulation, which is unsurprising, considering the significant positional scatter that is present in the dust particles in Figure 3.6. This dispersion is imparted by the relatively large velocity dispersion that is present in the SPH gas particles in the protoplanetary disk. This intrinsic dispersion and velocity noise is discussed in the following section, section 3.3.2, and a technique for reducing it is discussed in section 3.3.3.

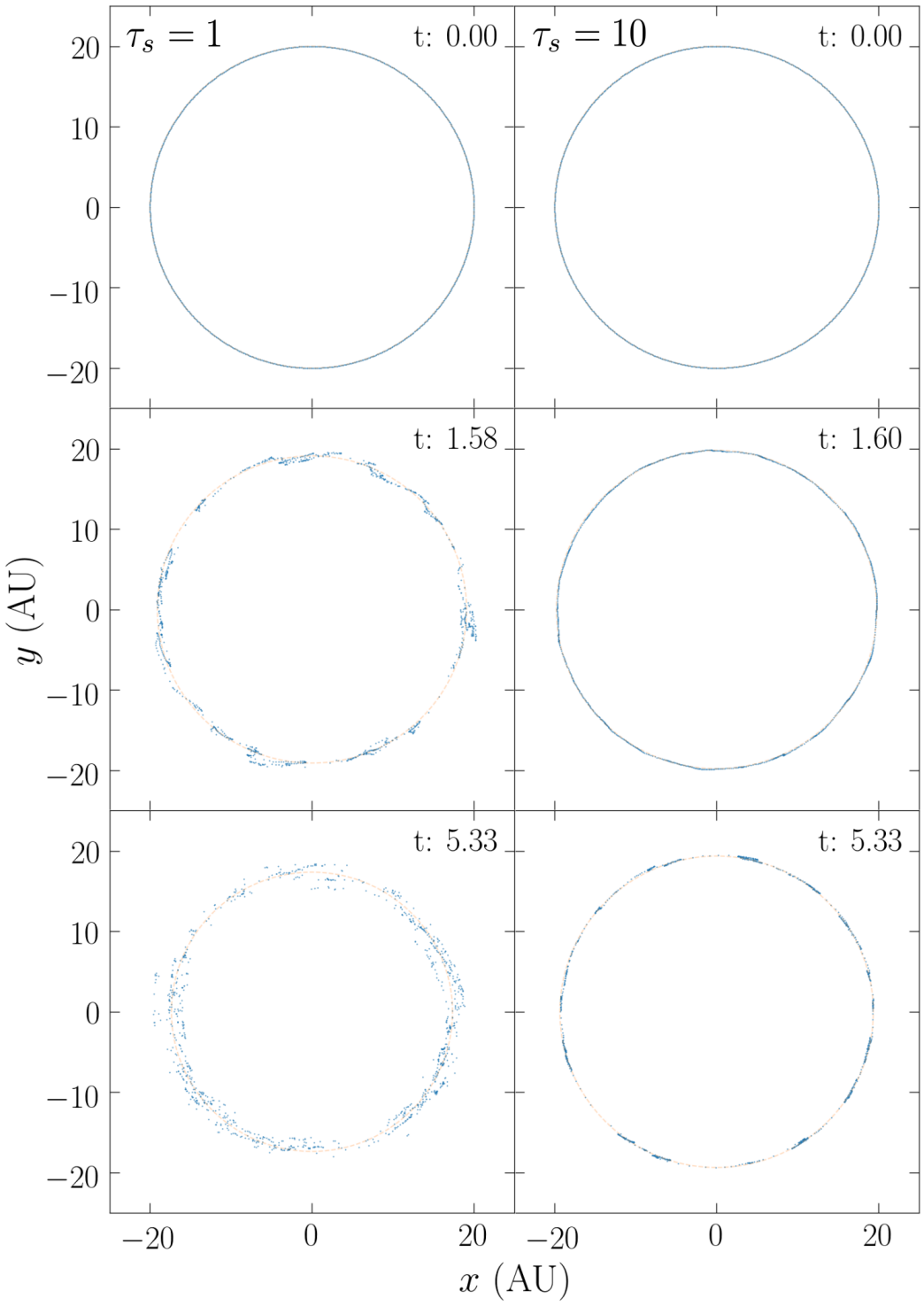

Figure 3.6: Evolution of the dust particle position in the x-y plane for the radial drift test with a 1,000 particle dust ring. Two different sizes of grains were tested, one with a size that gives $\tau_s = 1$ (left) and one with $\tau_s = 10$ (right).

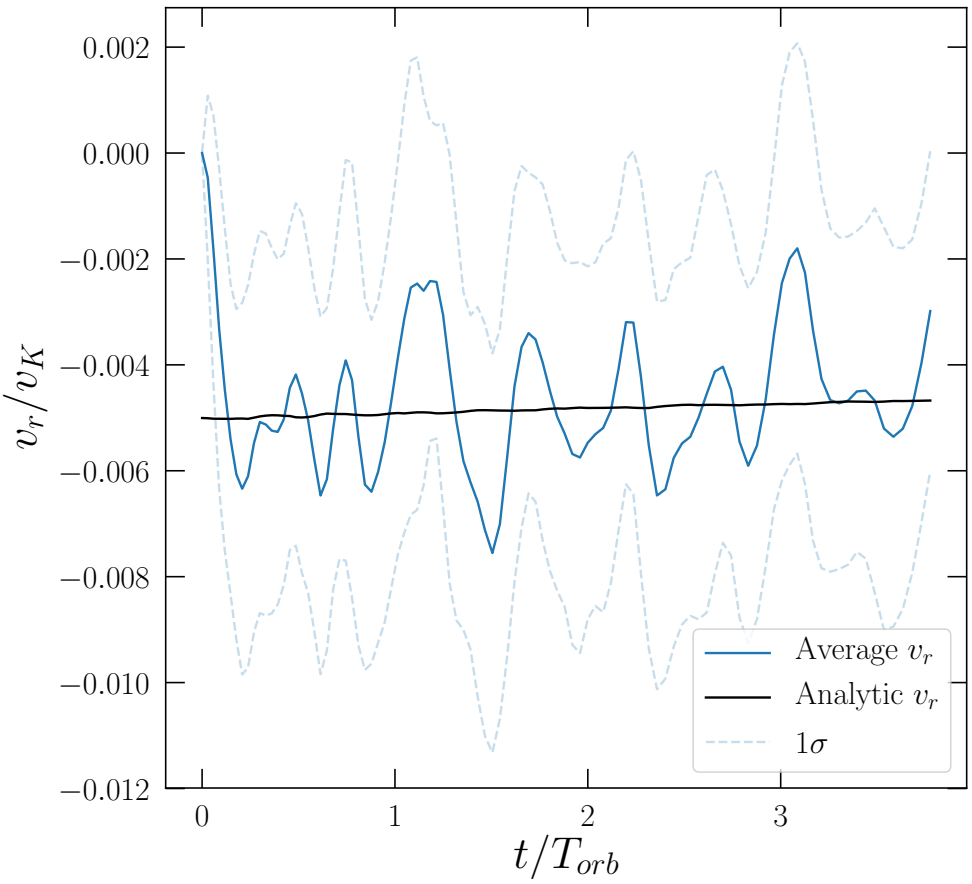

Figure 3.7: Averaged radial velocity of the dust particles in the $\tau_s = 1$ dust ring radial drift test as a function of elapsed time in the simulation, in units of the Keplerian orbital period, where this period is computed using the average radial position of the particles.

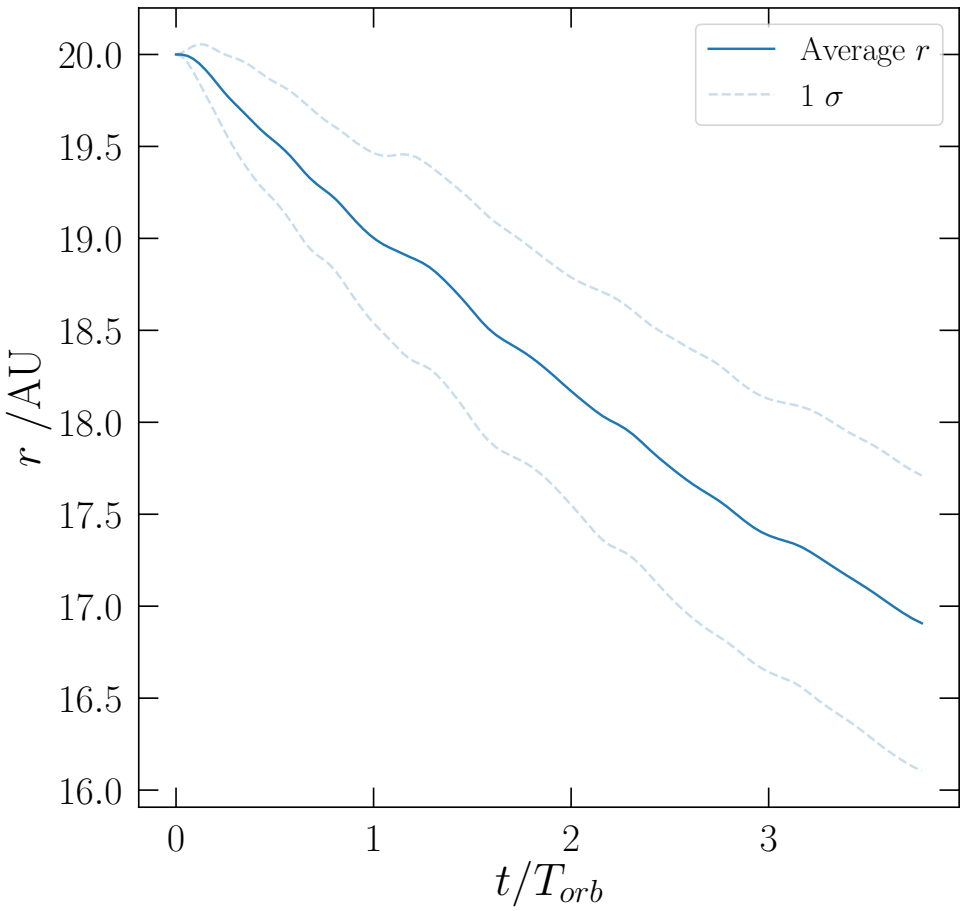

Figure 3.8: Averaged radial position of the dust particles in the $\tau_s = 1$ dust ring radial drift test as a function of elapsed time in the simulation, in units of the Keplerian orbital period, where this period is computed using the average radial position of the particles.

3.3.2 Gas particle random walk

In this section we will investigate the source of the velocity dispersion in the radial drift dust ring test seen in Figure 3.7. In our simulations, the only forces acting on the dust particles are the gravity from the central star and the aerodynamic drag imparted on the dust by the gas. Thus, the velocity dispersion seen in the dust must have come from dispersion in the gas as the gravity from the star would not create this dispersion. In Figure 3.9, the velocity dispersion in the dust and gas, in terms of the r, θ and z components, is shown for the dust particles in the middle frames of Figure 3.6. Also

included in this plot is the magnitude of the predicted radial velocity from equation 3.23.

We see the dispersion of the gas is between 2% and 5% of the azimuthal Keplerian velocity, and this is sufficiently large to stir up the dust particles in the $\tau_s = 1$ test such that the dispersion in the dust radial velocity is larger than the radial drift velocity that we are attempting to measure. We can observe a different measure of the gas velocity dispersion by observing the path the SPH gas particles take in the r-z plane over the course of a simulation. Examples of this are presented in Figure 3.10. We plot the path for three representative particles at three different orbital radii, and observe that the SPH particles perform a random walk through the r-z plane. For increasing radial position, the amount of turns and sharp corners in the path decreases, as the dynamical timescales decrease for increasing distance from the central star.

The dispersion in the $\tau_s = 10$ simulation is much smaller, and we can see in Figure 3.6 that the positions of the dust particles in the $\tau_s = 10$ test are significantly less perturbed from the ring shape than the $\tau_s = 1$ particles. The $\tau_s = 1$ grains represent the grain sizes that are maximally aerodynamically perturbed in the disk. In the radial drift rates in Figure 1.8 from Weidenschilling (1977), these are the grains for which the radial drift is a maximum. While $\tau_s = 1$ grains will be the most disturbed by the gas velocity dispersion, they also represent the grains which are the most active in the streaming instability, a proposed mechanism for overcoming the metre barrier that is introduced in Section 1.5 and covered in more detail in Chapter 4. Thus, while it may be tempting to use grains with sizes that are either much smaller or larger than $\tau_s = 1$ to avoid the velocity dispersion issue, it is precisely these grains which drive much of the interesting dust-gas dynamics in the disk.

It appears for global disk simulations in SPH, the density noise—which is responsible for generating this dispersion and random walk in the gas particles—is too large to measure any small signals or perturbations in the dust fluid. As is discussed in the next section, increasing the numerical resolution (adding SPH particles) should diminish the noise, but dramatically increased resolution would be required to observe effects such as the streaming instability. Studies using Eulerian grid codes (discussed briefly in Section 4.2) employ a physically smaller simulation domain, such as a shearing box (see Section 4.3.1) in order to represent a very small portion of a protoplanetary disk. Such adjustments are necessary in order to study physical effects which require high resolution such as the streaming instability. Presently, no shearing box module exists

in CHANGA, thus we plan to develop one, and use it to explore the ability of SPH to simulate the non-linearly evolving regime of the SI once implemented.

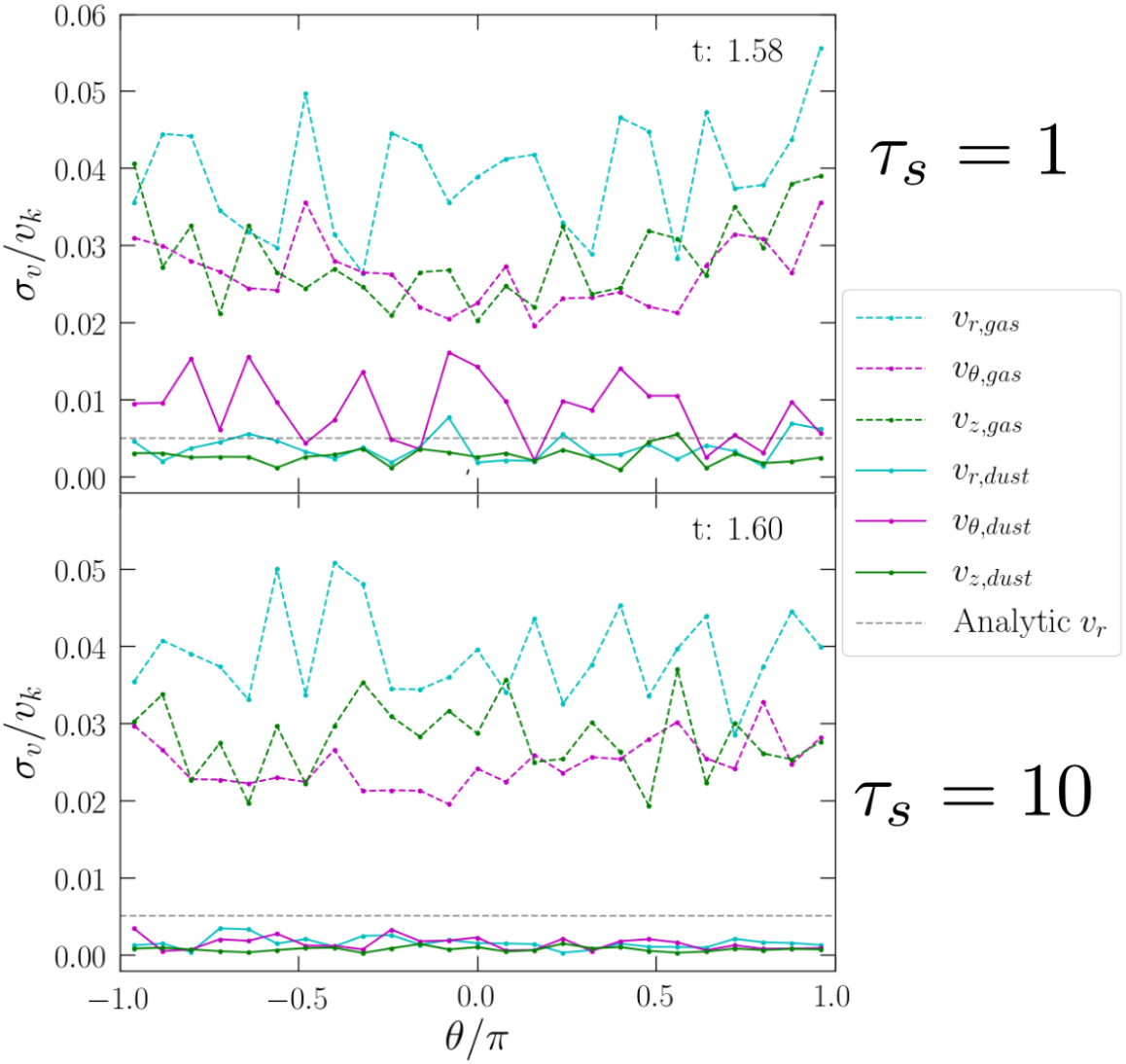

Figure 3.9: Velocity dispersion, σ_v, in units of the azimuthal Keplerian velocity, v_k, in the radial drift ring test. The top frame is for the $\tau_s = 1$ test, and the bottom frame is for the $\tau_s = 10$ test. The different coloured lines represent a different component of the velocity, and the dashed and solid lines represent the data for the gas and dust fluids, respectively. The analytically predicted dust radial velocity from equation 3.23 is given by the grey dashed line.

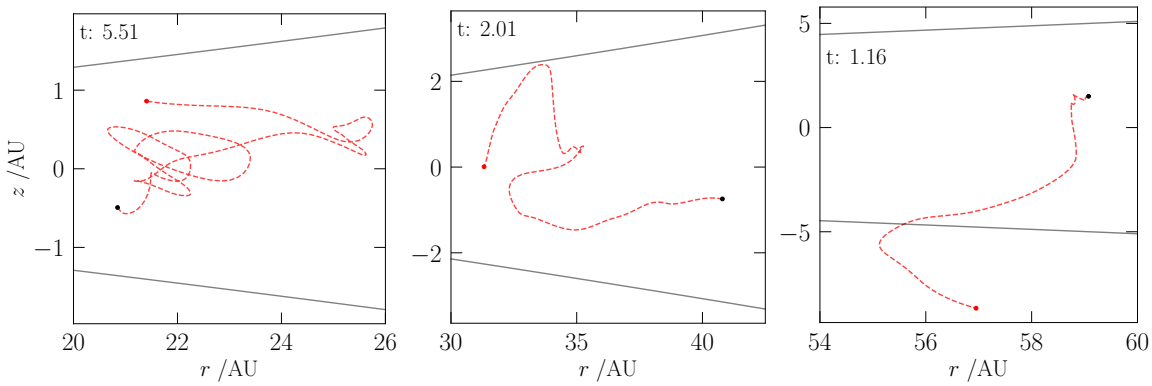

Figure 3.10: Random walk of gaseous SPH particles in the radial and vertical direction in a simulated protoplanetary disk. The numbers represented in the upper-left corner of each panel represent the elapsed time in the simulation, in units of the Keplerian orbital period, where this orbital period is calculated for each of the separate panels/particles individually, according to the particles' initial radial position. The initial particle positions are given by the black dots, the path the particle random walks is given by the red dotted line, the final position is given by the red dot, and the grey lines represent the vertical disk scale heights.

3.3.3 Increased resolution via particle splitting

The magnitude of the random walk discussed in the previous section, and the scale of the velocity dispersion, can be somewhat mitigated by increasing the numerical resolution of gaseous SPH particles in the simulation. For the purposes of this radial drift test, we would only benefit from an increase in gaseous resolution in the vicinity of the ring of dust, and increasing the global resolution of the disk would unnecessarily increase the required computing time of the simulation.

A method for locally increasing SPH resolution known as particle splitting can be used for this test. This method is introduced in Kitsionas and Whitworth (2002). The main principle of particle splitting is to replace single SPH particles by multiple SPH particles, taking care to ensure to the total mass represented by the new particles is equivalent to the mass of the original particle, and that the spatial distribution of the new distribution minimally disturbs the original density profile of the domain governed by the single particle. Kitsionas and Whitworth (2002) discuss an in depth method for splitting particles into 13 new particles, but we considered a simpler scheme that splits particles into pairs. For a given single particle with a smoothing length h_a and mass m_a, the split pair of particles will be separated from each other by h_a. To ensure

no new net mass is added to the simulation, each of the new particles will have mass $m_a/2$.

To test whether an increase in resolution could reduce the dispersion of the dust particles radial velocity for our drifting ring test, we decided to create a locally increased resolution region in our protoplanetary disk by splitting the gaseous SPH particles until the smoothing lengths in the new region were roughly half of the original smoothing lengths. In a three dimensional simulation, this requires an eight-fold increase in the number of particles.

Using the same protoplanetary disk initial condition as in section 3.3.1 which has 10^5 SPH particles, we created a region between approximately 40 and 70 AU where the local number of particles was increased by a factor of 8. We decided to create a buffer zone between this region and the edges of the disk, so that the numerical experiment of the radially drifting dust ring is shielded from any problems associated with the abrupt change in resolution. Thus we created a few regions where the resolution was decreased in steps from 8 times as many particles to the original number of particles. This is represented in Figure 3.12. In the region between approximately 40 and 70 AU where the numerical radial drift dust ring experiment is conducted, the average distance between particles in low resolution disk is roughly twice that of the particles in the new, high resolution disk. Inside 20 AU and outside 90 AU, the number of particles is unchanged, and the typical separation between the particles (computed as $l = (m\rho)^{(1/3)}$) is the same in the unsplit and split disks. Beyond ~ 25 AU the ratio of the separation in the unsplit disk and the split disk, l_u/l_s, increases to ~ 1.25 in a region where there are twice as many particles in the split disk as there are in the unsplit disk, and then to ~ 1.6 where there are four times as many particles.

A particle plot of the SPH particles in the midplane of the disk within 60 AU is provided in Figure 3.11 to show how this increase in resolution manifests itself visually in terms of spatial particle distributions.

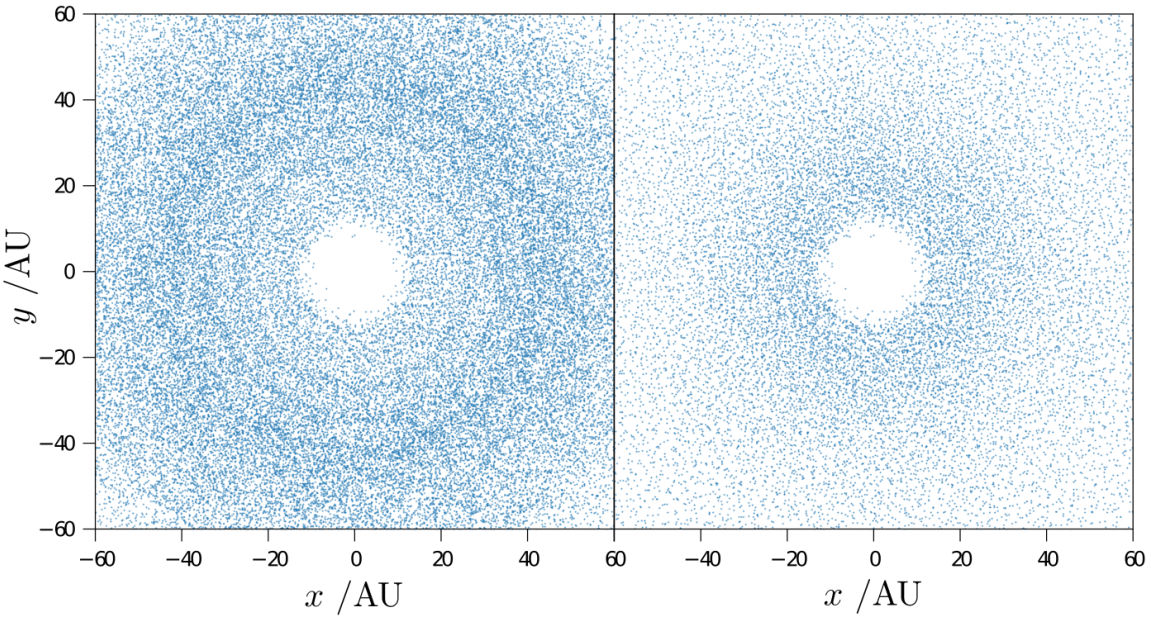

Figure 3.11: Position of the SPH particles in the rotational (x-y) plane of the disk for the high resolution disk with particle splitting (left) and the original, unsplit disk (right). Only particles near the disk midplane (within one smoothing length of $z = 0$) are shown.

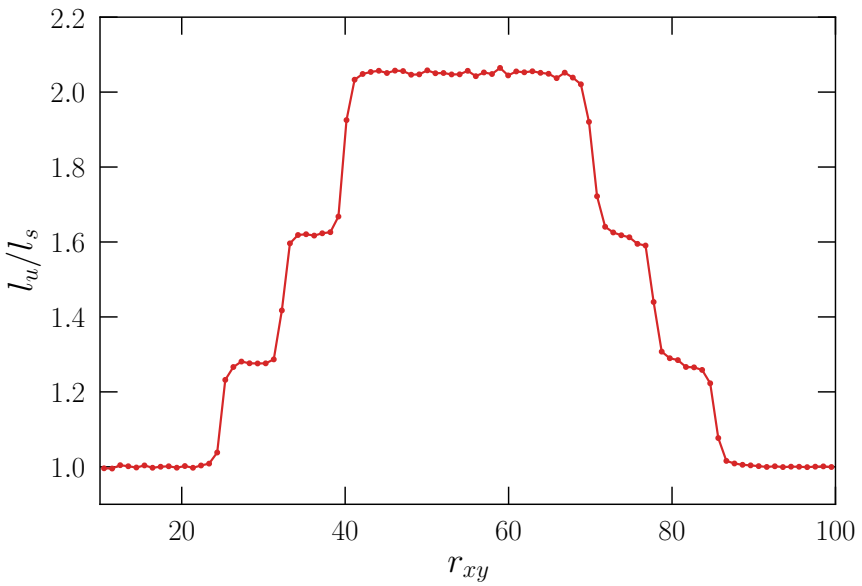

Figure 3.12: A histogram comparing the particle spacing, binned by midplane radius (r_{xy}), in the high resolution disk with particle splitting and the original, unsplit disk. The separation is estimated as $l = (m\rho)^{(1/3)}$, and the value on the y-axis the ratio of l in the unsplit disk to the split disk, l_u/l_s.

With this new protoplanetary disk, modified with an inner region of increased numerical resolution, we repeated the same ($\tau_s = 1$) radial drift dust ring test as described in Section 3.3.1. For this test, however, the dust ring was placed at 52 AU instead of 20 AU. The timescales which drive the physics are longer for larger radii, and we wanted to see if slower dynamics would mitigate the dispersion in the dust. Figures 3.13 and 3.14 show the radial velocity and the radial position, respectively, of the dust ring particles, as before. We note that there remains a considerable amount of scatter in the data, and any improvements in decreasing the scatter are minimal.

In Figures 3.15 and 3.16, we explicitly plot the standard deviation, σ, for the radial velocity and radial position, respectively. Here it is apparent that the increase in resolution offers a reduction in the scatter present in the dust particles, but it is not sufficient enough to offer the ability to clearly measure the expected radial drift signal of equation 3.23.

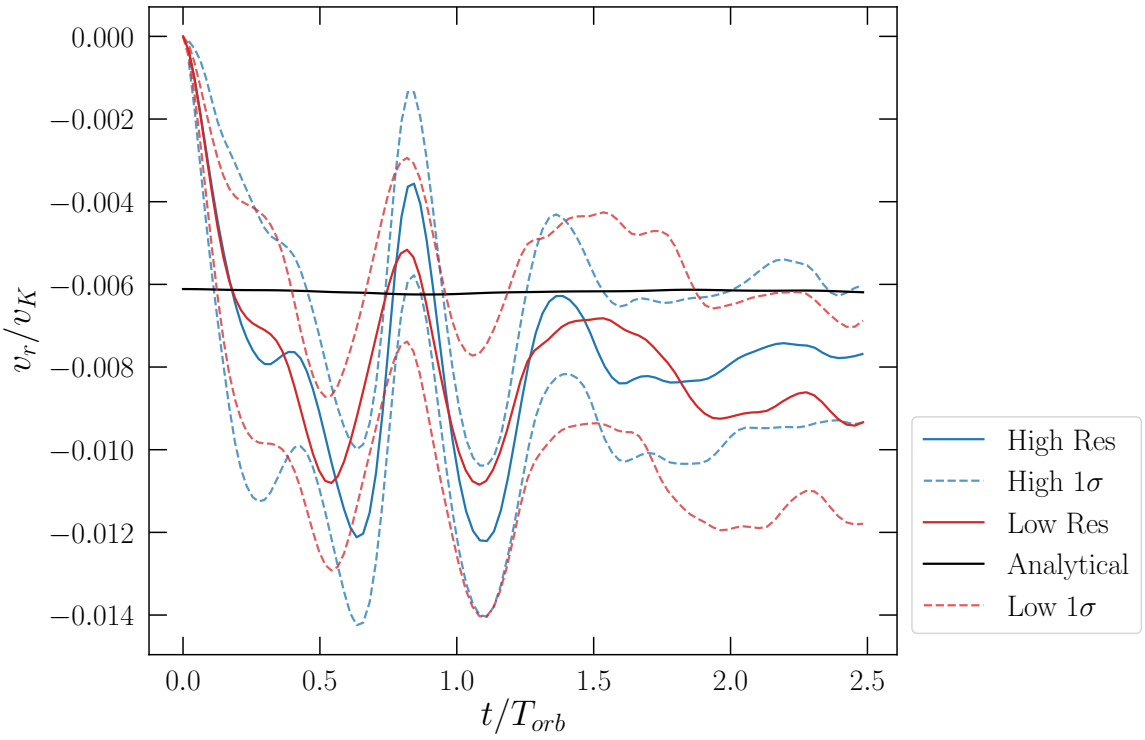

Figure 3.13: Averaged radial velocity of the dust particles in the $\tau_s = 1$ dust ring radial drift test, where the results for the higher resolution disk and the original, lower resolution disk are both shown. The x-axis represents the of elapsed time in the simulation, in units of the Keplerian orbital period, where this period is computed using the average radial position of the particles.

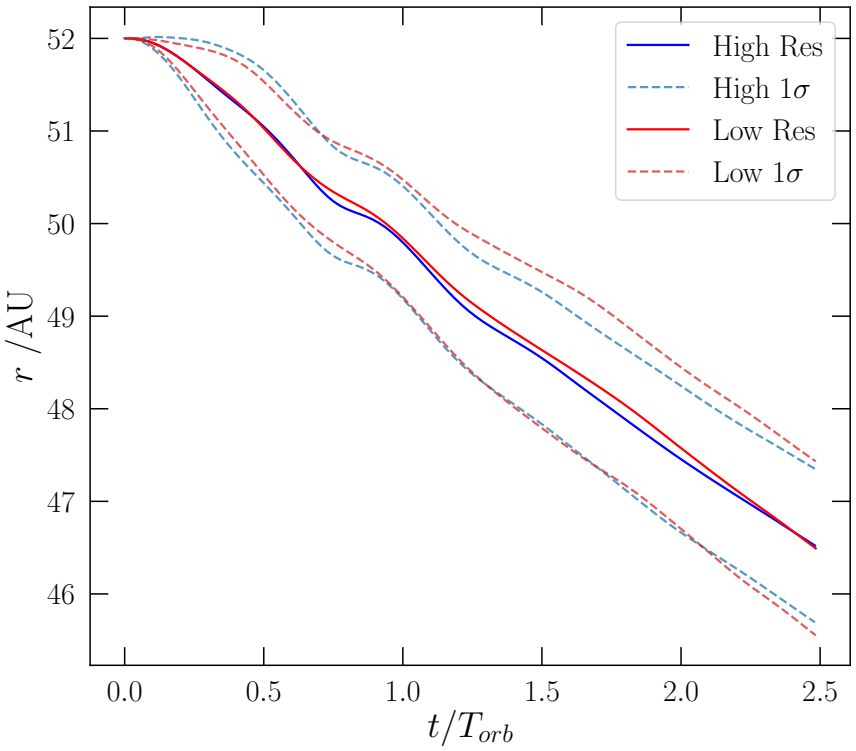

Figure 3.14: Averaged radial position of the $\tau_s = 1$ dust particles in the dust ring radial drift test, where the results for the higher resolution disk and the original, lower resolution disk are both shown. The time axis is in units of the Keplerian orbital period.

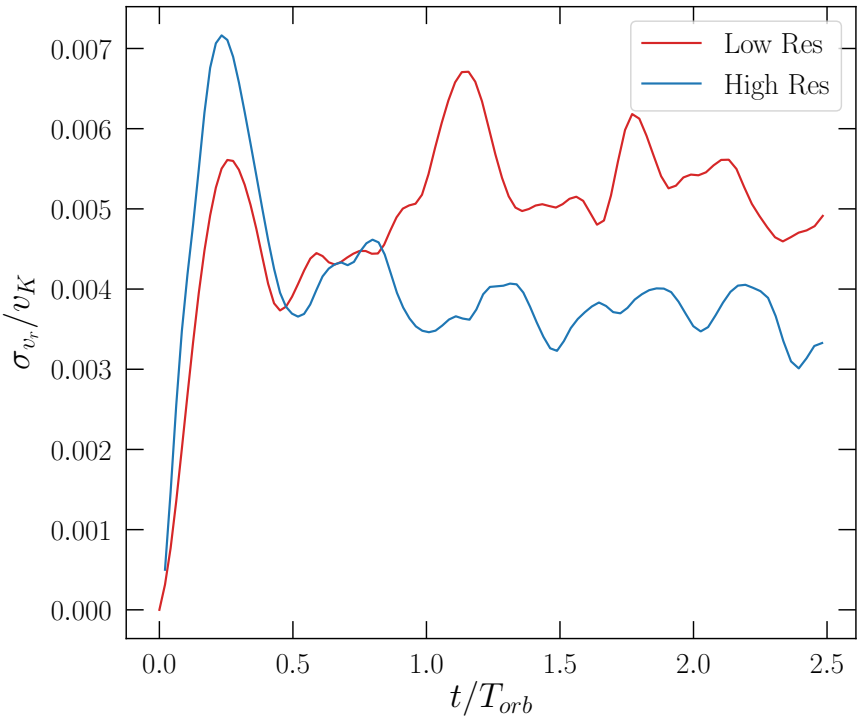

Figure 3.15: Time evolution of the standard deviation of the radial velocity of the dust particles in the $\tau_s = 1$ dust ring radial drift test, where the results for the higher resolution disk and the original, lower resolution disk are both shown. The time axis is in units of the Keplerian orbital period.

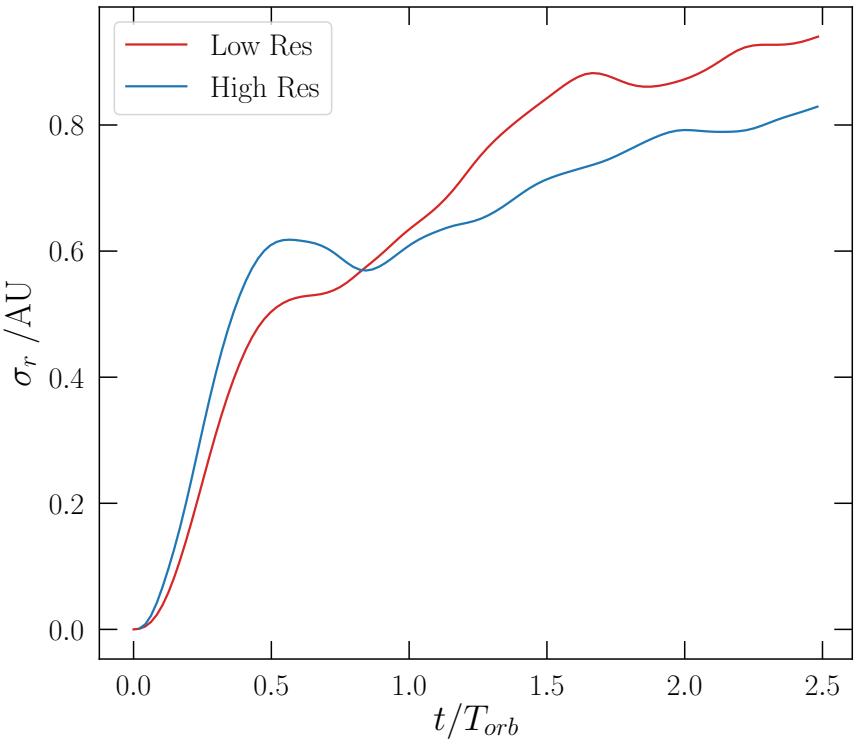

Figure 3.16: Time evolution of the standard deviation of the radial position of the dust particles in the $\tau_s = 1$ dust ring radial drift test, where the results for the higher resolution disk and the original, lower resolution disk are both shown. The time axis is in units of the Keplerian orbital period.

3.4 Conclusions

In SPH and in any numerical simulation scheme, it is important to avoid extracting physical interpretations from behaviour near the resolution limit. Individual SPH particles are not meant to represent the motions of gas directly. In order to obtain an accurate representation of the gas motions, an average over many particles must be computed. As discussed in Section 3.3.2, the error in the SPH density estimator results in a minimum level of velocity dispersion in the gas particles that can make it impossible to track subtle dust motions. In studies published by D. J. Price, who is one of the main researchers in the field of dust simulations in SPH, and his group, they are careful to avoid integrating the simulation over many dynamical times in cases with large outside drivers (such as a perturbing planet or binary), so that these errors do not compromise the simulation. For any study of full protoplanetary disks

where small perturbations are key to the result, even with state-of-the-art resolution, only large scale behaviour and dynamics with timescales smaller than a few orbits can be studied.

In investigating the results from the Gonzalez et al. (2017) study, we find that the results of their numerical simulations are apparently inconsistent with the predictions from the analytical analysis presented in the Appendix of the Gonzalez et al. (2017) paper (and in Figure 3.1 here). However, the analytic derivation applied to the midplane properties of the disk, so the results from their study may have originated from parts of the disk away from the midplane. In order to explore their proposed dust trap mechanism ourselves, we attempted to reproduce their numerical results in our own simulations, but were unable to. We did not see the dramatic grain growth and dust trap described in their study. Gonzalez et al. (2017) ran their simulations for hundreds of orbits and began with a quiet, featureless disk. As discussed above, integrating simulations of full three-dimensional disks for many orbital times may introduce macroscopic features in the disk that are purely due to numerical noise. Thus, we decided to pursue a different planetesimal formation mechanism which is more established in the literature.

The streaming instability which is introduced in Section 1.5 is a promising mechanism for overcoming the metre barrier problem. The ability to accurately reproduce the analytical growth rates from the linear phase of the instability with a numerical code is seen as an important test for dust and gas simulation codes. However, prominent researchers in the field have been unable to reproduce these growth rates in SPH (D. J. Price and G. Laibe, private communications). As mentioned in Section 3.3.2, it may be possible to study the non-linearly evolving phase of the streaming instability with SPH, but there is no module for the requisite shearing box boundary conditions in ChaNGa currently.

Thus, we decided to use Athena (Stone et al. 2008), an Eulerian code developed by J. Stone and his group which already has all the required computer code to simulate the streaming instability implemented and tested. We will discuss the streaming instability and the results of our investigations in the next chapter.

Chapter 4

Streaming Instability

The streaming instability (SI) was introduced in Section 1.5 as a potential solution to the metre barrier problem facing the earliest stages of planet formation, where micron sized grains must become kilometre sized planetesimals. In this chapter we will discuss the SI in detail.

The streaming instability was first introduced by Youdin and Goodman (2005), who demonstrated via linear perturbation analysis that in protoplanetary disks, plane waves which are aligned in the radial and vertical (normal to the rotational plane) directions can experience substantial growth in amplitude under the right disk conditions. These rapidly growing waves would then create regions of high dust density, potentially triggering gravitational collapse, the formation of planetesimals, and laying the seeds for planet formation. In Section 1.5.1 we discussed results from Johansen et al. (2007), one of the seminal studies on this topic, which demonstrates the SI (with the help of gravity) could drive the formation of a Ceres mass object directly from a disperse distribution of dust. This result garnered much attention from the planet formation community, and demonstrated that the streaming instability as a planet formation mechanism deserves to be studied thoroughly.

Following the original Youdin and Goodman (2005) introduction to the SI, Youdin and Johansen (2007) summarize the requirements of the linear plane wave analysis and describe methods for testing the analytical predictions in a numerical simulation suite. In a companion study, Johansen and Youdin (2007) use high resolution 3-D numerical simulations to investigate the properties of systems which have evolved beyond the linear growth stage of the SI and hence feature a collection of non-linearly

evolving dust clumps. Eventually this non-linearly evolving system saturates, and the densest clumps of dust do not increase in density. The Johansen and Youdin (2007) study is concerned with characterizing high level properties of these saturated states in simulations with differing dust properties such as total dust to gas mass ratio, and grain size. The properties they investigated include maximum dust density achieved, the population distribution of dust densities, and the radial drift of the dust particles. Bai and Stone (2010b) used similar high resolution 3-D simulations to demonstrate dust grains that vary in size by orders of magnitude participate in the streaming instability on different timescales, and settle to different vertical scale heights in the disk.

Recently, Squire and Hopkins (2018) suggested the SI should be reclassified to be one sub-group of a broader range of so-called resonant drag instabilities (RDI). The authors argue, via a matrix perturbation analysis, that instabilities like the SI will develop whenever the projection of the relative velocity between the dust and the gas along a particular direction matches a characteristic speed or timescale present within the system. This could be the sound speed of the gas, for example, or the orbital velocity, as is the case in the streaming instability as described by Youdin and Goodman (2005) and Youdin and Johansen (2007). Interestingly, Squire and Hopkins (2018) show that the growth rates predicted by the original linear perturbation analysis work with the SI—which assumed the only steady relative velocity between the dust and gas is in the radial and azimuthal direction, within the disk midplane—are greatly enhanced if a non-zero vertical component to the relative velocity is also considered. As promising as the original SI results are, one serious caveat within that work was that the growth rates were only sufficiently large for a very specific set of dust parameters. This Squire and Hopkins (2018) result offers a solution to this problem. Vertical relative velocities between the dust and gas will naturally be present everywhere within a protoplanetary disk as the dust settles to the disk midplane, streaming through the gas. We will discuss and investigate the utility of this prediction further in Section 4.4.

While a solid foundation of theoretical work has been constructed in the literature, we believe crucial questions regarding the behaviour of the instability in full protoplanetary disks, in nature, remain unanswered. The high resolutions simulations in Johansen and Youdin (2007) and Bai and Stone (2010b) require the use of shearing boxes (see Section 4.3.1), and it is unclear how well behaviour in such a truncated domain can be extrapolated to the behaviour of a full protoplanetary disk. Also, when

the non-linear evolution of the streaming instability in the previously mentioned high resolution shearing box simulations first activates, a particular, striped pattern in the radial-azimuthal (r-θ) direction appears. This pattern eventually gives way to a different r-θ pattern and the turbulent evolution of a saturated state. Currently there are no explanations for the prevalence of any resonant modes in the r-θ plane that create those patterns.

The original linear analysis of Youdin and Goodman (2005) was strictly axisymmetric; in r-z. Thus, physically, any structures that would form in this analysis represent axisymmetric rings when they are extrapolated to the full disk. This is similar to the classic gravitational instability analysis of Toomre (1964) which likewise employed axisymmetric perturbations. The issue with non-axisymmetric perturbations—those with an azimuthal component—is the differential rotation in the (nearly) Keplerian protoplanetary disks, which creates time-dependent perturbation terms when an analogous plane wave perturbation analysis is conducted. This will be demonstrated in Section 4.6, where we will also discuss techniques for probing this system for information about the growth of the r-θ modes of the SI. We believe this is crucial for understanding the global implications of the streaming instability, especially since it appears the dominant mode in the initial non-linear evolution is in r-θ and not r-z.

In this chapter, we will start with an overview of the linear plane-wave perturbation analysis, then discuss the enhanced growth rates predicted by Squire and Hopkins (2018) and our confirmation of these enhancements in numerical simulations. We will conclude by motivating our planned future work which will tackle the unanswered questions regarding the impact of the truncated of domain of the shearing boxes and r-θ modes of the SI which were mentioned above.

4.1 Linear plane wave perturbation

In this section we will retrace the original linear plane wave analysis of the streaming instability from Youdin and Goodman (2005)and Youdin and Johansen (2007), and explicitly explore some of the mathematical details left out by these papers.

We can rewrite the equations of the two-fluid dust and gas prescription (see equations 2.5) in terms of the dust to gas mass ratio μ and stopping time t_s,

$$\frac{\mathrm{d}\boldsymbol{v}_d}{\mathrm{d}t} = -\frac{1}{t_s}(\boldsymbol{v}_d - \boldsymbol{v}_g) \tag{4.1a}$$

$$\frac{\mathrm{d}\boldsymbol{v}_g}{\mathrm{d}t} = -\frac{\nabla P_g}{\rho_g} + \frac{\mu}{t_s}(\boldsymbol{v}_d - \boldsymbol{v}_g) \tag{4.1b}$$

$$\frac{\mathrm{d}\rho_g}{\mathrm{d}t} = -\rho_g(\nabla \cdot \boldsymbol{v}_g) \tag{4.1c}$$

$$\frac{\mathrm{d}\rho_d}{\mathrm{d}t} = -\rho_d(\nabla \cdot \boldsymbol{v}_d) \tag{4.1d}$$

These equations above can be rewritten to represent a fluid in a rotating frame where the azimuthal velocity is given by $\boldsymbol{V}_0 = -(3/2)\Omega x\hat{\mathbf{y}}$ as (e.g. Goldreich and Lynden-Bell (1965a), Youdin and Johansen (2007)),

$$\frac{\partial \boldsymbol{v}}{\partial t} + (\boldsymbol{v}\cdot\nabla)\boldsymbol{v} - \frac{3}{2}\Omega x\frac{\partial \boldsymbol{v}}{\partial y} = 2\Omega v_y\hat{x} - \frac{1}{2}\Omega v_x\hat{y} - \frac{\Omega}{\tau_s}(\boldsymbol{v}-\boldsymbol{u}) \tag{4.2a}$$

$$\frac{\partial \boldsymbol{u}}{\partial t} + (\boldsymbol{u}\cdot\nabla)\boldsymbol{u} - \frac{3}{2}\Omega x\frac{\partial \boldsymbol{u}}{\partial y} = 2\Omega u_y\hat{x} - \frac{1}{2}\Omega u_x\hat{y} - {c_s}^2\nabla\ln\rho_g + 2\eta v_K\Omega\hat{x} - \frac{\mu\Omega}{\tau_s}(\boldsymbol{u}-\boldsymbol{v}) \tag{4.2b}$$

$$\frac{\partial \rho_g}{\partial t} + \boldsymbol{u}\cdot\nabla\rho_g - \frac{3}{2}\Omega x\frac{\partial \rho_g}{\partial y} = -\rho_g\nabla\cdot\boldsymbol{u} \tag{4.2c}$$

$$\frac{\partial \rho_d}{\partial y} = -\rho_d\nabla\cdot\boldsymbol{v} \tag{4.2d}$$

where we have made changes to the notation from Chapter 2 which we will use for the remainder of this chapter.

Equations 4.2 have been written to represent a local spatial expansion about a point within the rotating planetary disk (as in Goldreich and Lynden-Bell (1965a)). That is, we have a point with a radial, azimuthal, and vertical coordinate given by (R, θ, z_0), where $R = 0$ at the position of the star in the centre of the disk and $z_0 = 0$ in the disk midplane. We then write a new set of coordinates (x, y, z) which represent radial, azimuthal and vertical displacements from the original (R, θ, z_0) co-ordinates. Thus the position of any point referenced by equations 4.2 with respect to the central is ($R + x$, $\theta + y$, $z_0 + z$). For the entirety of this linear perturbation analysis, we will work within the rotating frame of this local expansion.

The dust velocity is now represented by $\boldsymbol{v}$, and the gas velocity by $\boldsymbol{u}$. As before ρ_d

and ρ_g are the dust and gas densities, respectively, c_s is the gas sound speed, Ω is the Keplerian angular velocity.

As in Section 3.3.1, v_K is the Keplerian azimuthal velocity, and η is given by,

$$\eta = n\left(\frac{c_s}{v_K}\right)^2 \tag{4.3}$$

where we have assumed the midplane gas pressure follows $P \propto r^{-n}$.

The analytical growth rate analysis for the SI (Youdin and Goodman (2005)) begins with a linear plane wave perturbation to equations 4.2. The perturbations will be represented by the following notation, using the dust velocity as an example,

$$\boldsymbol{v} = \overline{\boldsymbol{v}} + \delta\boldsymbol{v} \tag{4.4}$$

here $\overline{\boldsymbol{v}}$ represents a steady, background dust velocity, and $\delta\boldsymbol{v}$ is a small perturbation to that value. The perturbation of the dust velocity can be broken down into each of its components, so, for the x direction,

$$v_x = \overline{v}_x + \delta v_x \tag{4.5}$$

The perturbations to the density will look a little different,

$$\rho_d = \rho_{p0}[1 + \delta\rho_d] \tag{4.6}$$

so we note here that $\delta\rho_d$ is a dimensionless quantity. The gas velocity $\boldsymbol{u}$ and the gas density ρ_g will also have similar perturbations.

The functional form of the perturbation is a plane wave travelling in the x-z (radial-vertical) directions,

$$\delta f(x,z) = \widetilde{f}\exp[i(k_x x + k_z z - \omega t)] \tag{4.7}$$

where f is a placeholder symbol that would represent any of the velocity or (dimensionless) density perturbations in the same manner. Note that the complex-valued amplitudes associated with these perturbations, $\widetilde{f}$, will be much smaller than the background values.

For coupled dust and gas fluids orbiting in a Keplerian protoplanetary disk, the

steady state equilibrium or background velocities are given by (Nakagawa et al. 1986),

$$\overline{u}_x = \frac{2\mu\tau_s}{(1+\mu)^2 + {\tau_s}^2}\eta v_K \tag{4.8a}$$

$$\overline{u}_y = -\left[1 + \frac{\mu {\tau_s}^2}{(1+\mu)^2 + (\tau_s)^2}\right]\frac{\eta v_K}{1+\mu} \tag{4.8b}$$

$$\overline{v}_x = -\frac{2\tau_s}{(1+\mu)^2 + {\tau_s}^2}\eta v_K \tag{4.8c}$$

$$\overline{v}_y = -\left[1 - \frac{{\tau_s}^2}{(1+\mu)^2 + (\tau_s)^2}\right]\frac{\eta v_K}{1+\mu} \tag{4.8d}$$

from Section 2.1, $\mu \equiv \rho_d/\rho_g$ and $\tau_s \equiv t_s\Omega$ is the dimensionless stopping time. Recall the dust velocity is now represented by $\boldsymbol{v}$, and the gas velocity by $\boldsymbol{u}$. Note, as discussed in the introduction to this chapter, there is no vertical steady-state relative velocity between the two fluids in the original SI analysis of Youdin and Goodman (2005) and Youdin and Johansen (2007). This will be changed in the Squire and Hopkins (2018) results we discuss later.

In regimes where the dust mass fraction is low ($\mu \ll 1$) and the dust grains are small ($\tau_s \ll 1$, typically valid for $\sim \mu$m to mm grains) the y velocities are of order ηv_K for both fluids, and the x velocities are of order $\mu\tau_s\eta v_K$ and $\tau_s\eta v_K$ for the gas and dust, respectively. The parameter η is typically of order 10^{-3} Armitage (2013). Note that in the global frame of the protoplanetary disk, these velocities are measured with respect to the Keplerian velocity at the radial position R that the local expansion is centred on.

These background velocities are ultimately generated by the radial pressure gradient that the gas fluid experiences. The acceleration generated by this gradient is represented in the $2\eta v_K\Omega\hat{x}$ term in equation 4.2b, which does not appear in the equation of motion of the dust particles (equation 4.2a) as the dust particles do not feel this gradient directly, but will experience it indirectly via the drag force. The $-{c_s}^2\nabla \ln \rho_g$ term is also a hydrodynamic force that the dust does not experience that is related to local gradients in the gas density. We assume that there are no local, macroscopic background gas density gradients, so the $2\eta v_K\Omega\hat{x}$ term is the only hydrodynamic term that generates a stable scenario where the dust is perpetually streaming through the

gas with a steady state relative velocity. The streaming instability and the other resonant drag instabilities reported by Squire and Hopkins (2018) cannot not operate if the dust is not streaming through the gas with a stable relative velocity.

4.1.1 Assumptions and simplifications

In this section we will highlight simplifications that can be applied to equations 4.2 for our purposes.

The full form of the $(\boldsymbol{v}\cdot\nabla)\boldsymbol{v}$ terms are,

$$(\boldsymbol{v}\cdot\nabla)\boldsymbol{v} = \left(v_x\frac{\partial}{\partial x} + v_y\frac{\partial}{\partial y} + v_z\frac{\partial}{\partial z}\right)\boldsymbol{v}$$

Here, the $\partial/\partial y$ term is zero, because we will assume there are no y gradients in the dust or gas velocity, and in general all properties within the disk are axisymmetric. Recall from equation 4.7 that the plane wave perturbation is only in the x-z direction. Without this assumption of axisymmetry, non-linear terms that are explicit functions of time would be required (Goldreich and Lynden-Bell (1965b), see also Section 4.6). Thus we now have,

$$(\boldsymbol{v}\cdot\nabla)\boldsymbol{v} = \left(v_x\frac{\partial}{\partial x}\boldsymbol{v} + v_z\frac{\partial}{\partial z}\boldsymbol{v}\right)$$

Furthermore, the equilibrium components of the velocity, $\overline{\boldsymbol{v}}$, have no spatial gradients, so we can replace $\boldsymbol{v}$ with just $\delta\boldsymbol{v}$ in the above, leaving us with

$$(\boldsymbol{v}\cdot\nabla)\boldsymbol{v} = \left(v_x\frac{\partial}{\partial x}\delta\boldsymbol{v} + v_z\frac{\partial}{\partial z}\delta\boldsymbol{v}\right)$$

Finally, we note that there is no equilibrium velocity in the z direction, i.e. $v_z = \delta v_z$. Hence the $\partial/\partial z$ term is proportional to the perturbation squared, so it can be ignored. For the same reason, the perturbation term in $v_x = \overline{v_x} + \delta v_x$, can be ignored. Thus, the simplified form of the $(\boldsymbol{v}\cdot\nabla)\boldsymbol{v}$ term is,

$$(\boldsymbol{v}\cdot\nabla)\boldsymbol{v} = \overline{v_x}\frac{\partial}{\partial x}\delta\boldsymbol{v} \tag{4.9}$$

an identical line of reasoning produces an analogous form for the $(\boldsymbol{u}\cdot\nabla)\boldsymbol{u}$ terms.

The gas pressure term $\nabla \ln \rho_g$ in equation 4.2b can be simplified with the knowledge

ρ_g is of the form in equation 4.6. We can use the logarithm identity,

$$\ln(a+c) = \ln(a) + \ln\left(1 + \frac{c}{a}\right)$$

to write $\ln \rho_g$ as,

$$\ln \rho_g = \ln \rho_{g0} + \ln(1 + \delta\rho_g)$$

When evaluating $\nabla \ln \rho_g$, since ρ_{g0} is a constant value, $\nabla \ln \rho_{g0} = 0$, giving

$$\nabla \ln \rho_g = \nabla \ln(1 + \delta\rho_g) = \frac{1}{1+\delta\rho_g}\nabla(1 + \delta\rho_g) = \frac{1}{1+\delta\rho_g}\nabla\delta\rho_g$$

We can expand the leading factor $1/(1 + \delta\rho_g) \sim 1 - \delta\rho_g$ to get,

$$\nabla \ln \rho_g \sim (1 - \delta\rho_g)\nabla\delta\rho_g$$

as before, the $-\delta\rho_g$ term can be ignored as that will give us a term of order the perturbation squared, leaving us with a final, simplified expression,

$$\nabla \ln \rho_g \sim \nabla\delta\rho_g \tag{4.10}$$

We can ignore the terms with a partial derivative in y, such as

$$-\frac{3}{2}\Omega x\frac{\partial \boldsymbol{v}}{\partial y}$$

because we assume there are no gradients for any quantities in y in this analysis. (This will be changed in our analysis in Section 4.6.)

There are terms in the momentum equations (4.2a and 4.2b) which involve particular components of the velocity,

$$2\Omega v_y \hat{x} - \frac{1}{2}\Omega v_x \hat{y}$$

The form of the equilibrium velocities from equations 4.8 guarantees that the background components ($\overline{v}_x$, $\overline{v}_y$) in these terms will completely cancel the background components that are contributed by the drag terms, which scale with $-(1/\tau_s)(\boldsymbol{v} - \boldsymbol{u})$. The result is in each term that involves the velocities or a component of the velocities,

such as

$$2\Omega v_y \hat{x} - \frac{1}{2}\Omega v_x \hat{y}$$

and the drag terms,

$$-\frac{1}{\tau_f}(\boldsymbol{v} - \boldsymbol{u})$$

we may simply substitute the perturbation in for the full expression which would normally include the background, equilibrium component. By the same effect, the $2\eta v_K \Omega \hat{x}$ term in equation 4.2b is cancelled by terms from the equilibrium velocities from equation 4.8.

4.1.2 Plane wave assumption

We will explicitly rewrite equations 4.2 using the simplifications from Section 4.1.1. The density continuity equations will be normalized by ρ_{p0}, ρ_{g0}, and we note $\partial\rho/\partial t = \partial\delta\rho/\partial t$ and $\nabla\rho = \nabla\delta\rho$. The new equations are,

$$\frac{\partial \delta\rho_d}{\partial t} + \boldsymbol{v} \cdot \nabla\delta\rho_d = -(1 + \delta\rho_d)\nabla \cdot \boldsymbol{v} \tag{4.11a}$$

$$\frac{\partial \boldsymbol{v}}{\partial t} + \overline{v_x}\frac{\partial}{\partial x}\delta\boldsymbol{v} = 2\Omega\delta v_y\hat{x} - \frac{1}{2}\Omega\delta v_x\hat{y} - \frac{\Omega}{\tau_s}(\boldsymbol{\delta w} - \boldsymbol{\delta u}) \tag{4.11b}$$

$$\frac{\partial \delta\rho_g}{\partial t} + \boldsymbol{u} \cdot \nabla\delta\rho_g = -(1 + \delta\rho_g)\nabla \cdot \boldsymbol{u} \tag{4.11c}$$

$$\frac{\partial \boldsymbol{u}}{\partial t} + \overline{u_x}\frac{\partial}{\partial x}\delta\boldsymbol{u} = 2\Omega\delta u_y\hat{x} - \frac{1}{2}\Omega\delta u_x\hat{y} - {c_s}^2\nabla\delta\rho_g + -\frac{\Omega}{\tau_s}(\delta\boldsymbol{u} - \delta\boldsymbol{v}) \tag{4.11d}$$

With the perturbations for each variable given by equation 4.7, for each of the derivatives involving perturbations, we have,

$$\nabla\delta f = i\boldsymbol{k}\delta f$$

$$\nabla \cdot \delta\boldsymbol{f} = i\boldsymbol{k} \cdot \delta\boldsymbol{f}$$

$$\frac{\partial f}{\partial t} = -i\omega\delta f$$

where $\boldsymbol{k} = k_x\hat{x} + k_z\hat{z}$. Evaluating the derivatives from equations 4.11, the system of

equations becomes,

$$-i\omega\delta\rho_d + i(\overline{\boldsymbol{v}}\cdot\boldsymbol{k})\delta\rho_d = -i(\delta\boldsymbol{v}\cdot\boldsymbol{k}) \tag{4.12a}$$

$$-i\omega\delta\boldsymbol{v} + i\overline{v}_x k_x\delta\boldsymbol{v} = 2\Omega\delta v_y\hat{x} - \frac{1}{2}\Omega\delta v_x\hat{y} - \frac{\Omega}{\tau_s}(\boldsymbol{\delta w} - \boldsymbol{\delta u}) \tag{4.12b}$$

$$-i\omega\delta\rho_g + i(\boldsymbol{u}\cdot\boldsymbol{k})\delta\rho_g = -i(\delta\boldsymbol{u}\cdot\boldsymbol{k}) \tag{4.12c}$$

$$-i\omega\delta\boldsymbol{u} + i\overline{u}_x k_x\delta\boldsymbol{u} = 2\Omega\delta u_y\hat{x} - \frac{1}{2}\Omega\delta u_x\hat{y} - ic_s{}^2\boldsymbol{k}\delta\rho_g - \frac{\Omega\mu}{\tau_s}\Big(\delta\boldsymbol{u} - \delta\boldsymbol{v} - (\delta\rho_d - \delta\rho_g)(\overline{\boldsymbol{v}} - \overline{\boldsymbol{u}})\Big) \tag{4.12d}$$

4.1.3 Eigenvalue problem

To emphasize the eigenvalue problem that is involved in this perturbation analysis, we will write out the full eight equations described by equations 4.12 explicitly. Here, the complex exponential wave factor of each perturbation δf—which exists in every term—has been dropped, leaving the complex amplitudes $\widetilde{f}$ only. Also wherever there would be a term proportional to the perturbation squared, it is dropped. These equations are not explicitly detailed in Youdin and Goodman (2005) or Youdin and Johansen (2007), but they are essential for numerical studies of the linear regime of the SI. The amplitudes of each of the fluid properties given by the eigenvector must be known to a few digits of accuracy in order for the eigenmode to be produced properly in a simulation.

In full, we have,

$$-i\omega\widetilde{\rho_d} + i\overline{v}_x k_x\widetilde{\rho_d} + ik_x\widetilde{v}_x + ik_z\widetilde{v}_z = 0 \tag{4.13a}$$

$$-i\omega\widetilde{v}_x + i\overline{v}_x k_x\widetilde{v}_x - 2\Omega\widetilde{v}_y + \frac{\Omega}{\tau_s}\widetilde{v}_x - \frac{\Omega}{\tau_s}\widetilde{u}_x = 0 \tag{4.13b}$$

$$-i\omega\widetilde{v}_y + i\overline{v}_x k_x\widetilde{v}_y + \frac{1}{2}\Omega\widetilde{v}_x + \frac{\Omega}{\tau_s}\widetilde{v}_y - \frac{\Omega}{\tau_s}\widetilde{u}_y = 0 \tag{4.13c}$$

$$-i\omega\widetilde{v}_z + i\overline{v}_x k_x\widetilde{v}_z + \frac{\Omega}{\tau_s}\widetilde{v}_z - \frac{\Omega}{\tau_s}\widetilde{u}_z = 0 \tag{4.13d}$$

$$-i\omega\widetilde{\rho_g} + i\overline{u}_x k_x \widetilde{\rho_g} + ik_x\widetilde{u}_x + ik_z\widetilde{u}_z = 0 \tag{4.13e}$$

$$\begin{aligned} &-i\omega\widetilde{u}_x + i\overline{u}_x k_x \widetilde{u}_x - 2\Omega\widetilde{u}_y + ic_s{}^2 k_x\widetilde{\rho_g} \\ &\qquad - \frac{\Omega\mu}{\tau_s}(\overline{v}_x - \overline{v}_x)\delta\rho_d + \frac{\Omega\mu}{\tau_s}(\overline{v}_x - \overline{v}_x)\delta\rho_g + \frac{\Omega\mu}{\tau_s}\widetilde{u}_x - \frac{\Omega\mu}{\tau_s}\widetilde{v}_x = 0 \end{aligned} \tag{4.13f}$$

$$\begin{aligned} &-i\omega\widetilde{u}_y + i\overline{u}_x k_x \widetilde{u}_y + \frac{1}{2}\Omega\widetilde{u}_x \\ &\qquad - \frac{\Omega\mu}{\tau_s}(\overline{v}_y - \overline{v}_y)\delta\rho_d + \frac{\Omega\mu}{\tau_s}(\overline{v}_y - \overline{v}_y)\delta\rho_g + \frac{\Omega\mu}{\tau_s}\widetilde{u}_y - \frac{\Omega\mu}{\tau_s}\widetilde{v}_y = 0 \end{aligned} \tag{4.13g}$$

$$-i\omega\widetilde{u}_z + i\overline{u}_x k_x \widetilde{u}_z + ic_s{}^2 k_z\widetilde{\rho_g} + \frac{\Omega\mu}{\tau_s}\widetilde{u}_z - \frac{\Omega\mu}{\tau_s}\widetilde{v}_z = 0 \tag{4.13h}$$

These equations can be written in matrix form, as an eigenvalue equation,

$$[\underline{\mathbf{T}} - i\omega\underline{\mathcal{I}}]\boldsymbol{v} = \mathbf{0} \tag{4.14}$$

where the eigenvector is the complex amplitudes of the perturbations,

$$\boldsymbol{v} = \begin{bmatrix} \widetilde{\rho}_p \\ \widetilde{v}_x \\ \widetilde{v}_y \\ \widetilde{v}_z \\ \widetilde{\rho}_g \\ \widetilde{u}_x \\ \widetilde{u}_y \\ \widetilde{u}_z \end{bmatrix}$$

and the matrix $\underline{\mathbf{T}}$ that defines the system has four parts:

$$\underline{\mathbf{T}} = \begin{bmatrix} \mathcal{A} & \mathcal{C}_p \\ \mathcal{C}_g & \mathcal{F} \end{bmatrix}$$

$\mathcal{A}$ are coefficients for the dust fluid,

$$\mathcal{A} = \begin{bmatrix} i\overline{v}_x k_x & ik_x & 0 & ik_z \\ 0 & i\overline{v}_x k_x + \Omega/\tau_s & -2\Omega & 0 \\ 0 & \Omega/2 & i\overline{v}_x k_x + \Omega/\tau_s & 0 \\ 0 & 0 & 0 & i\overline{v}_x k_x + \Omega/\tau_s \end{bmatrix}$$

$\mathcal{C}_p$ are coefficients for coupling between the dust and the gas,

$$\mathcal{C}_p = \begin{bmatrix} 0 & 0 & 0 & 0 \\ 0 & -\Omega/\tau_s & 0 & 0 \\ 0 & 0 & -\Omega/\tau_s & 0 \\ 0 & 0 & 0 & -\Omega/\tau_s \end{bmatrix}$$

$\mathcal{C}_g$ are coefficients for coupling between the gas and the dust,

$$\mathcal{C}_g = \begin{bmatrix} 0 & 0 & 0 & 0 \\ -(\Omega\mu/\tau_s)(\overline{v}_x - \overline{v}_x) & -\Omega\mu/\tau_s & 0 & 0 \\ -(\Omega\mu/\tau_s)(\overline{v}_y - \overline{v}_y) & 0 & -\Omega\mu/\tau_s & 0 \\ 0 & 0 & 0 & -\Omega\mu/\tau_s \end{bmatrix}$$

and $\mathcal{F}$ are coefficients for the gas fluid,

$$\mathcal{F} = \begin{bmatrix} i\overline{u}_x k_x & ik_x & 0 & ik_z \\ ic_s{}^2 k_x + (\Omega\mu/\tau_s)(\overline{v}_x - \overline{v}_x) & i\overline{u}_x k_x + \Omega\mu/\tau_s & -2\Omega & 0 \\ (\Omega\mu/\tau_s)(\overline{v}_y - \overline{v}_y) & \Omega/2 & i\overline{u}_x k_x + \Omega\mu/\tau_s & 0 \\ ic_s{}^2 k_z & 0 & 0 & i\overline{u}_x k_x + \Omega\mu/\tau_s \end{bmatrix}$$

The linear wave perturbation SI analyses of Youdin and Goodman (2005), Youdin and Johansen (2007) and Squire and Hopkins (2018) explore the solutions to the eigenvalue equation given by equation 4.14.

Specifically, the imaginary component of the eigenvalue ω, which we will label s, represents the exponential growth rate of the amplitude of the plane wave (i.e. $\widetilde{f}(t) \propto e^{st}$). The full system described by equations 4.13 is fully characterized by four values[1]: τ_s, μ, k_x, and k_z. For any set of four parameters, there are eight eigenvalues

[1]This excludes the gas properties, which determine c_s and η, and in most studies are not treated as tuneable parameters. Bai and Stone (2010c) study the effects of the strength of the radial pressure

and eigenmodes, and only some of these modes produce a positive value for s.

Figure 4.1 below shows one result from the Youdin and Goodman (2005) study. The parameters μ and τ_s are presented on the x and y axes respectively. The value for k_z is fixed, and k_x is selected to represent the fastest growing mode, or the mode with the largest value of s. These maximum values of s for each choice of μ and τ_s are shown in the left panel of Figure 4.1, where s is in units of the Keplerian angular frequency, Ω. Hence a value of $\log(2\pi s/\Omega) = -1.0$ represents a mode with an e-folding growth timescale of 10 orbits.

The general trends from the left panel of Figure 4.1 conclude that modes with rapid growth timescale of $\lesssim 10$ orbits are only widely available when $\tau_s > 0.1$ or $\mu > 1$ and $\tau_s > 0.005$. The right panel of Figure 4.1 shows what values of k_x produced the highest value for s. The trend presented in this figure shows that for decreasing values of τ_s, an increasing value of k_x is required to produce the fastest growing mode. The perturbation becomes increasingly shallow, towards the purely radial direction where k_x/k_z is large, and the vertically travelling component is small.

gradient (characterized by η) on non-linear SI growth, and find large radial gradients suppress growth in regions with high dust mass fractions.

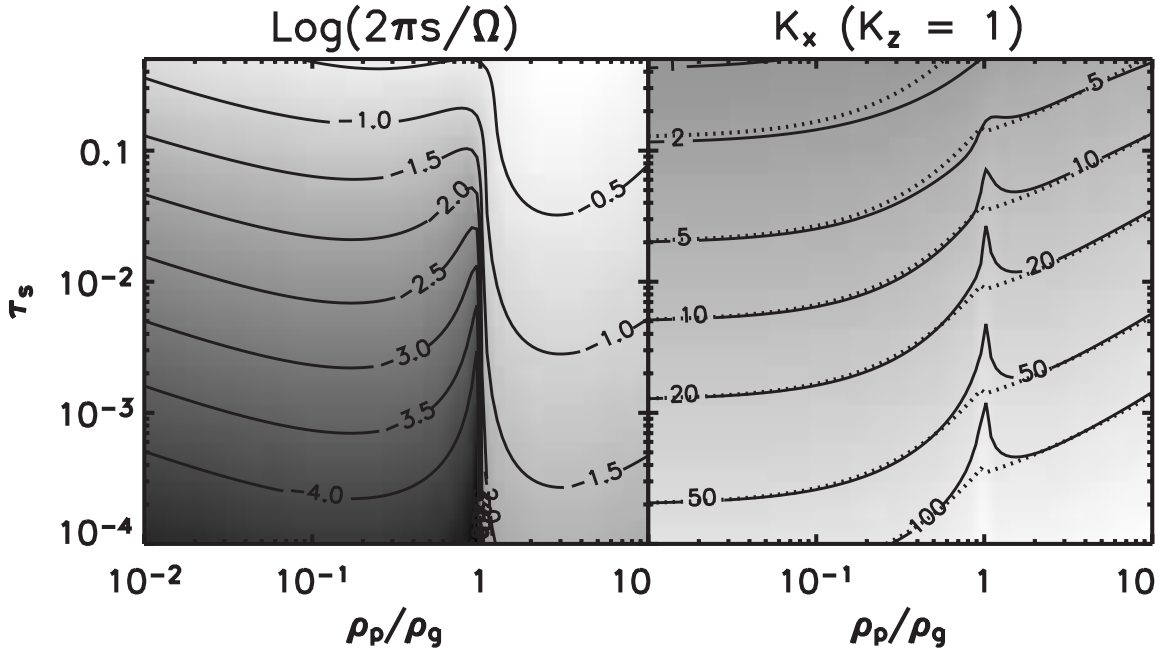

Figure 4.1: *Left.* Growth rates, s, of the linear wave perturbation amplitudes due to the fastest growing mode of the streaming instability. Note, the growth rates are scaled by a factor $2\pi/\Omega$. The growth rates are marked by the contours, and the parameters space being explored are the dust properties: $\mu \equiv \rho_d/\rho_g$ on the x-axis, and τ_s on the y-axis. *Right.* The value of k_x which produces the fastest growing mode according to the same parameter space as the left panel, when k_z is fixed at a particular value. From Youdin and Goodman (2005), reproduced with permission.

Figure 4.2 shows a similar analysis of the fastest growing modes in the original SI, generated from our eigenvalue analysis, which matches results from Squire and Hopkins (2018). This plot assumes an angle of $\theta_k \equiv \tan^{-1}(k_x/k_z) = 30°$ and explores growth rates over the range of $k \equiv \sqrt{{k_x}^2 + {k_z}^2}$ and a select few choices of τ_s and μ. This figure highlights the dependence of the SI growth rate on the wavelength of the perturbation, which scales as k^{-1}. Indeed, in the original Youdin and Goodman (2005) and Youdin and Johansen (2007) linear perturbation analysis, only astrophysical systems with a very specific grain size (characterized by τ_s), dust to gas mass ratio μ, and perturbation wavelengths could experience growth with timescales shorter than 100 orbits. The specificity of the action of the SI presents a problem when considering the instability as an answer to the metre-barrier problem facing planet formation.

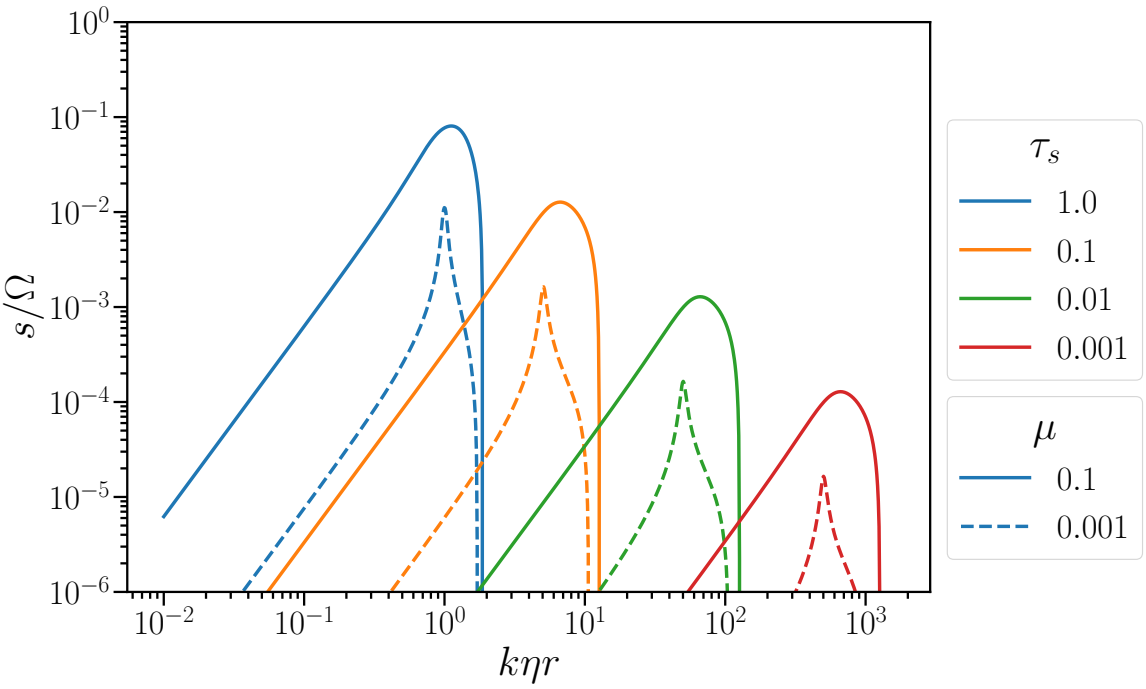

Figure 4.2: Growth rates of the linear wave perturbation amplitudes due to the fastest growing mode of the streaming instability. Here, the angle between the perturbation wave vector components is fixed at $\theta_k \equiv \tan^{-1}(k_x/k_z) = 30°$. The magnitude of the wave vector is plotted on the x-axis, with the growth rate s of the fastest growing mode plotted on the y-axis. A range of systems with various values of τ_s and μ are considered. These results match Squire and Hopkins (2018).

From the right panel of Figure 4.1 and Figure 4.2 we can identify a general trend: as τ_s decreases, the perturbation wavenumber $k \equiv \sqrt{{k_x}^2 + {k_z}^2}$ which corresponds to the peak growth rate increases, which means the corresponding wavelength λ decreases. The sound crossing time across the peak perturbation wavelength, which we will call t_c, is given by,

$$t_c = \frac{\lambda}{c_s} \tag{4.15}$$

where c_s is the sound speed. The properties of the gas such as c_s are held constant in Figure 4.1 and Figure 4.2. Thus, the propagation speed for any of the modes present in either of the individual figures will be the same, given by c_s. The timescales which describe the dynamics of the propagation of the perturbation wave and the drag force should be similar in order for the linear plane wave grow via the streaming instability. For small grains which are tightly coupled to the gas, the timescale which governs the

aerodynamic drag force, the stopping time, is short compared to the stopping time for larger grains. Thus, the sound crossing time given by equation 4.15 should by similarly short. Since c_s is the same for all modes in Figures 4.1 and 4.2, this means λ must become smaller, and k must become larger.

4.1.4 Enhanced growth rates due to vertical dust settling

The primary result from Squire and Hopkins (2018) concerning the SI proposes that when a vertical component to the relative streaming velocity between the dust and gas is considered, instead of just a radial-azimuthal streaming velocity, the growth rates predicted by an identical linear wave perturbation analysis as described above are noticeably enhanced. That is, the values for the growth rates are higher, and remain high even for large values of k or small grains with small values of τ_s, contrary to the previous analysis that produced the results in Figure 4.2.

We will briefly highlight the differences in the linear perturbation analysis above that arise from a non-zero vertical streaming velocity. In nature, dust will settle to the midplane in gaseous protoplanetary disks which have vertically stratified density profiles that monotonically decrease for vertical positions away from the midplane. Hence, in our analysis we will decide to apply the steady vertical velocity to the dust fluid, and we will revisit the simplifications from Section 4.1.1 and derivatives from Section 4.1.2 assuming that $\overline{v}_z$ is not zero. These details are not included in Squire and Hopkins (2018), however, we believe they are useful for a complete description of the origin of the enhanced growth rates.

In the $(\boldsymbol{v}\cdot\nabla)\boldsymbol{v}$ term, we can no longer neglect the $\partial/\partial z$ term so we have,

$$(\boldsymbol{v}\cdot\nabla)\boldsymbol{v} = \overline{v}_x\frac{\partial}{\partial x}\delta\boldsymbol{v} + \overline{v}_z\frac{\partial}{\partial z}\delta\boldsymbol{v}$$

evaluating the derivatives gives,

$$(\boldsymbol{v}\cdot\nabla)\boldsymbol{v} = i\overline{v}_x k_x\delta\boldsymbol{v} + i\overline{v}_z k_z\delta\boldsymbol{v} \tag{4.16}$$

The dot product $\overline{\boldsymbol{v}}\cdot\boldsymbol{k}$ from equation 4.12a now has a term from the z component,

$$\overline{\boldsymbol{v}}\cdot\boldsymbol{k} = \overline{v}_x k_x + \overline{v}_z k_z$$

and in the $(\delta\rho_d - \delta\rho_g)(\overline{\boldsymbol{v}} - \overline{\boldsymbol{u}})$ term in equation 4.12d, $\overline{\boldsymbol{v}}$ now has a z component.

The full eight equations, analogous to equations 4.13, now look like,

$$-i\omega\widetilde{\rho_d} + i(\overline{v}_x k_x + \overline{v}_z k_z)\widetilde{\rho_d} + ik_x\widetilde{v}_x + ik_z\widetilde{v}_z = 0 \tag{4.17a}$$

$$-i\omega\widetilde{v}_x + i(\overline{v}_x k_x + \overline{v}_z k_z)\widetilde{v}_x - 2\Omega\widetilde{v}_y + \frac{\Omega}{\tau_s}\widetilde{v}_x - \frac{\Omega}{\tau_s}\widetilde{u}_x = 0 \tag{4.17b}$$

$$-i\omega\widetilde{v}_y + i(\overline{v}_x k_x + \overline{v}_z k_z)\widetilde{v}_y + \frac{1}{2}\Omega\widetilde{v}_x + \frac{\Omega}{\tau_s}\widetilde{v}_y - \frac{\Omega}{\tau_s}\widetilde{u}_y = 0 \tag{4.17c}$$

$$-i\omega\widetilde{v}_z + i(\overline{v}_x k_x + \overline{v}_z k_z)\widetilde{v}_z + \frac{\Omega}{\tau_s}\widetilde{v}_z - \frac{\Omega}{\tau_s}\widetilde{u}_z = 0 \tag{4.17d}$$

$$-i\omega\widetilde{\rho_g} + i\overline{u}_x k_x\widetilde{\rho_g} + ik_x\widetilde{u}_x + ik_z\widetilde{u}_z = 0 \tag{4.17e}$$

$$\begin{aligned} &-i\omega\widetilde{u}_x + i\overline{u}_x k_x\widetilde{u}_x - 2\Omega\widetilde{u}_y + ic_s{}^2 k_x\widetilde{\rho_g} \\ &\quad - \frac{\Omega\mu}{\tau_s}(\overline{v}_x - \overline{v}_x)\delta\rho_d + \frac{\Omega\mu}{\tau_s}(\overline{v}_x - \overline{v}_x)\delta\rho_g + \frac{\Omega\mu}{\tau_s}\widetilde{u}_x - \frac{\Omega\mu}{\tau_s}\widetilde{v}_x = 0 \end{aligned} \tag{4.17f}$$

$$\begin{aligned} &-i\omega\widetilde{u}_y + i\overline{u}_x k_x\widetilde{u}_y + \frac{1}{2}\Omega\widetilde{u}_x \\ &\quad - \frac{\Omega\mu}{\tau_s}(\overline{v}_y - \overline{v}_y)\delta\rho_d + \frac{\Omega\mu}{\tau_s}(\overline{v}_y - \overline{v}_y)\delta\rho_g + \frac{\Omega\mu}{\tau_s}\widetilde{u}_y - \frac{\Omega\mu}{\tau_s}\widetilde{v}_y = 0 \end{aligned} \tag{4.17g}$$

$$\begin{aligned} &-i\omega\widetilde{u}_z + i\overline{u}_x k_x\widetilde{u}_z + ic_s{}^2 k_z\widetilde{\rho_g} \\ &\quad - \frac{\Omega\mu}{\tau_s}\overline{v}_z\delta\rho_d + \frac{\Omega\mu}{\tau_s}\overline{v}_y\delta\rho_g + \frac{\Omega\mu}{\tau_s}\widetilde{u}_z - \frac{\Omega\mu}{\tau_s}\widetilde{v}_z = 0 \end{aligned} \tag{4.17h}$$

A simple expression for the steady vertical dust streaming velocity and a settling timescale can be derived as follows, as in Chiang and Youdin (2010).

The equation of motion for the dust grains in the vertical direction is a simple ordinary differential equation,

$$\ddot{z} = -\dot{z}/t_s - \Omega^2 z$$

where z is the vertical position, $\dot{z}$ and $\ddot{z}$ denote first and second derivatives with respect to time, respectively, and t_s is the dimensional stopping time (c.f. equation 2.6). This is an equation for a damped harmonic oscillator, which would have a characteristic damping time (which physically represents a characteristic settling time),

$$t_{settle} \sim \frac{1}{\Omega}\left(\frac{2{\tau_s}^2 + 1}{\tau_s}\right) \tag{4.18}$$

For grains falling from one gas scale height, $H_g \equiv c_s/\Omega$, the steady vertical dust streaming velocity can be written as,

$$\overline{v}_z = \frac{H_g}{t_s} = c_s\left(\frac{\tau_s}{2{\tau_s}^2 + 1}\right) \tag{4.19}$$

Figure 4.6 shows the expected growth rates from an eigenvalue analysis that we have applied to equations 4.17, where a vertical dust streaming velocity according to equation 4.19 has been considered. The same sets of parameters as in Figure 4.2 are investigated. The peak growth rates for all sets of parameters are much higher than those in Figure 4.2, especially in systems with small dust grains (small τ_s). The off-peak growth rates in each set of parameters plateau at relatively high values—as high as $s/\Omega \sim 0.03$ in $\tau_s = 1.0$, $\mu = 0.1$—instead of rapidly decreasing for values of k greater than the peak value as in Figure 4.2.

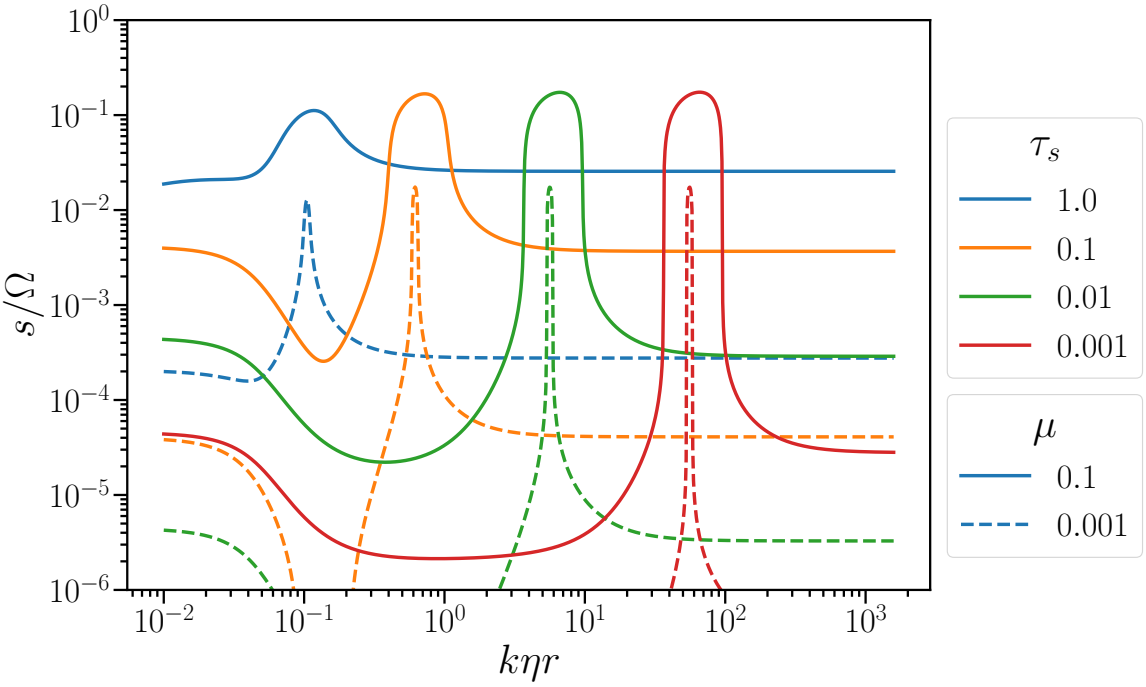

Figure 4.3: Growth rates of the linear wave perturbation amplitudes due to the fastest growing mode of the streaming instability, as in Figure 4.2. However, this analysis was completed including a vertical component to the steady-state background dust velocity according to equation 4.19. These results match Squire and Hopkins (2018).

These results suggest the previously mentioned issue concerning the limited range of parameters for which the SI is effective is mitigated by the addition of a vertical dust streaming velocity to the system. Grains of all sizes, even those with small values of τ_s, can grow rapidly in this scenario, provided the growth timescales are shorter than the settling timescale. Once the dust particles settle to the midplane, the vertical velocities will decrease and the enhanced SI growth rates will not apply.

4.1.5 Settling timescale versus growth timescales

We present a quick calculation which investigates whether the growth timescales will indeed be smaller than the settling timescales outlined in equation 4.18.

We can define a growth timescale simply as $t_{growth} \equiv 1/s$. Then, we want to

investigate the ratio t_{growth}/t_{settle},

$$\frac{t_{growth}}{t_{settle}} = \frac{1}{s} \Big/ \Big(\frac{1}{\Omega} \Big(\frac{2{\tau_s}^2 + 1}{\tau_s} \Big) \Big) = \frac{\Omega}{s} \Big(\frac{\tau_s}{2{\tau_s}^2 + 1} \Big)$$

For the enhanced SI growth rates from vertical dust streaming to apply, we require as a minimum constraint $t_{growth}/t_{settle} < 1$, which translates to,

$$\frac{s}{\Omega} > \frac{\tau_s}{2{\tau_s}^2 + 1} \tag{4.20}$$

For the values of τ_s in Figure 4.6, namely, $1, 0.1, 0.01, 0.001$, the right side of equation 4.20 evaluates to approximately $0.33, 0.1, 0.01, 0.001$ respectively. Taking a glance at Figure 4.6, we can see that for $\tau_s = 1$ the condition in equation 4.20 is not satisfied for any value of k, but for smaller grain sizes/stopping times, the peak growth rates are large enough to satisfy this condition. Since all the peak values for each grain size are nearly the same, this condition is easily met for small grains as $t_{settle} \sim \tau_s \Omega$ for $\tau_s \ll 1$. For the peak growth rates for the $\tau_s = 0.001$ grains, we have $t_{growth}/t_{settle} \sim 0.01$. From this quick analysis we see that only small dust grains will be able to experience these increased growth rates, as it takes a long time for these grains to fully settle to the midplane.

4.2 Eulerian codes for simulation dust and gas

One method for numerically solving the hydrodynamics equations involves Eulerian or grid-based domain decompositions. The discrete elements in these methods are fixed, and do not move with the fluid, unlike Lagrangian methods such as smoothed particle hydrodynamics. The fluid quantities (density, momentum, etc.) in these schemes represent the average of each quantity in the volume occupied by the discrete grid or cell elements. The movement or transfer of each quantity is created by approximating the fluxes that would be present at the shared interfaces between each cell and its direct neighbours, and modifying the averaged quantities within the cells according to that flux.

The most popular grid codes in astrophysics are Godunov type schemes (e.g. Athena, Stone et al. (2008)), the most popular of these being the Piece-wise Parabolic

Method from Colella and Woodward (1984). An alternative grid scheme uses a finite difference approach, one example being the Pencil Code (Brandenburg 2003) employed by A. Johansen and his group, who feature heavily in the streaming instability work presented in this chapter. The Pencil code uses sixth order accurate derivatives in space and is thus formally very accurate, however, finite difference schemes are not conservative, which creates issues when they are used for non-linear evolving systems or are integrated for many dynamical times.

To illustrate the behaviour of the evolution of fluid quantities in grid schemes, we will write down a general equation of the evolution, and pair it with a schematic representation of these grid elements, following Stone et al. (2008). We will let the vector $\boldsymbol{U}$ represent the volume averaged fluid quantities, and let the vectors $\boldsymbol{F}$, $\boldsymbol{G}$, $\boldsymbol{H}$ represent the flux of these quantities through the x, y, and z boundaries of each grid cell, respectively. The diffusion equation that guides the evolution of these vectors is simply,

$$\frac{\partial \boldsymbol{U}}{\partial t} + \frac{\partial \boldsymbol{F}}{\partial x} + \frac{\partial \boldsymbol{G}}{\partial y} + \frac{\partial \boldsymbol{H}}{\partial z} = 0 \tag{4.21}$$

This a general expression used for Eulerian schemes. (Note that there are no material derivatives in this expression, which were denoted by $\mathrm{d}/\mathrm{d}t$ in Chapters 2 and 3, c.f. equation 2.4.) Figure 4.4 presents a graphical representation of a 3-D grid cell element. The quantities $\boldsymbol{U}$ represent the average density, momentum, etc. within each discrete cell, and the fluxes are approximated directly at the boundaries of each cell.

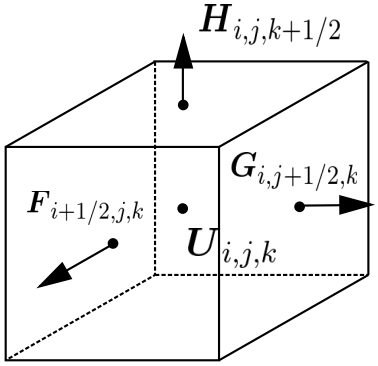

Figure 4.4: Schematic representation of a 3-D grid code resolution element. Modified from Stone et al. (2008)

When simulating dust particles in grid codes, a common method is to generate particles which are free to move throughout the gas cells (Youdin and Johansen (2007),

Bai and Stone (2010a)). In this sense, the Eulerian (grid) and Lagrangian (SPH) representation of dust are essentially the same. These particles interact with the fluid grid via momentum exchanges from aerodynamic drag. As discussed in Section 2.1, the drag force is proportional to the difference in velocity between the dust phase and the gas phase, which is $\boldsymbol{v} - \boldsymbol{u}$ in the notation from this chapter. When computing the velocity difference between the free moving particles and the fixed grid, the velocities must be measured at the same position in space. The positions of the dust particles are in general different from the centre of each of the gas cells. Therefore computing these drag forces accurately requires the use of an interpolation function W_1 to translate gas velocities to the location of the gas particles. Following Youdin and Johansen (2007), the interpolated gas velocity at each of the dust particle positions $\boldsymbol{x}_d^{(i)}$ is,

$$\overline{\boldsymbol{u}(\boldsymbol{x}_d^{(i)})} = \sum_a W_I(\boldsymbol{x}_d^{(i)} - \boldsymbol{x}_g^{(a)})\boldsymbol{u}^{(a)} \tag{4.22}$$

where i and a are superscripts for the dust particles and gas cells respectively, $\boldsymbol{u}^{(a)}$ is the uninterpolated gas velocity and $\boldsymbol{x}_g^{(a)}$ is the position of the centre of the gas cell. The weighted sum is computed over the gas cells denoted by a that are direct neighbours of the cell which contains $\boldsymbol{x}_d^{(i)}$.

The drag force on each particle is then simply the difference between the particle velocity and the gas velocity interpolated to this particle position,

$$\boldsymbol{f}_d^{(i)} = -\frac{\boldsymbol{v}^{(i)} - \overline{\boldsymbol{u}(\boldsymbol{x}_g^{(a)})}}{t_s} \tag{4.23}$$

Computing the backreaction drag force on the gas also requires an interpolation function, to interpolate back to the cell positions from the particle positions. We will label this function W_2. The form of the drag force on the gas cells is then,

$$\boldsymbol{f}_g^{(a)} = -\frac{m_d}{\rho_g^{(a)} V_{cell}} \sum_i W_A(\boldsymbol{x}_d^{(i)} - \boldsymbol{x}_g^{(a)})\boldsymbol{f}_d^{(i)} \tag{4.24}$$

In this drag scheme, linear momentum is conserved,

$$V_{cell} \sum_a \rho_g^{(a)} f_g^{(a)} + m_d \sum_i f_d^{(i)} = 0 \tag{4.25}$$

However, angular momentum is typically not conserved exactly (for drag, or any

other forces) in grid codes.

So long as the particles do not interact with each other (e.g. gravitationally), W_1 and W_2 can be chosen independently without violating linear momentum conservation. However, Youdin and Johansen (2007) comment that choosing $W_1 = W_2$ is safest so that the smoothing of both drag forces is symmetric[2]. The exact shape of the interpolation functions is a design choice in the construction of this algorithm, with a common preference being the triangular-shaped cloud scheme (Hockney and Eastwood (1981)).

4.3 3D Simulations in a shearing box

Some of the most relevant research concerning the streaming instability has been conducted using high resolution 3-D simulations. The linear SI analysis summarized in Figures 4.1 and 4.2 suggest that the physical size of the perturbations that can grow the quickest are quite small, and this presents a significant resolution challenge for large scale protoplanetary disk simulations.

For instance, the peak growth rate possible in the original SI analysis without the vertical component of the dust streaming velocity occurs for a system with $k\eta r \sim 1$. The wavelength this corresponds to is $\lambda = 2\pi/k = 2\pi\eta r$, or $\lambda/r \sim 0.01$ for $\eta \sim 10^{-3}$. Youdin and Johansen (2007) suggest 64 resolution elements per wavelength are required to resolve the SI accurately. Thus a resolution of 64 elements per 1 percent radial increments are required to resolve the fastest growing mode of the SI, which is a resolution scale wholly inaccessible to global disk simulations.

For the enhanced growth rates from vertical dust settling summarized in Figure 4.6, the same analysis for the fastest growing mode for the $\tau_s = 0.001$ grains gives $\lambda/r \sim 1$.

In order to faithfully simulate the streaming instability in 3D, studies have had to rely on domains with periodic boundary conditions. The idea is to simulate a small portion of the disk which is meant to be representative of the hydrodynamic and aerodynamic behaviour of the dust and gas on the smallest length scales. These simulation domains in these studies represent very small spatial domains when compared to the

[2]There is a noteworthy similarity between the role of the interpolation function W_1 and the SPH kernel function from Section 3.1. Both decide the weights of quantities for individual resolution elements in a sum, and the main argument is a spatial separation distance.

size of full protoplanetary disks, and this allows for sufficient numerical resolution to observe the SI.

The boundary conditions used in these simulations must be more intricate than typical periodic conditions. The radial boundary of the boxes must be shear-periodic to represent the radial gradient in the azimuthal velocity of the dust and gas, which is predominantly Keplerian. These shearing box simulation domains will be briefly discussed in the next section.

Lastly, it is important to note that the evolution of the streaming instability studied in these 3D shearing box simulations is non-linear. The dust density perturbations in the initial conditions of these studies are too large to be applicable to the linear growth theory, which requires the amplitude of the perturbations to be much smaller than the background values.

4.3.1 Shearing box simulation domain

In standard periodic boundary conditions, particles and cells interact with other cells through the boundaries as though copies of the cubic simulation domain have been translated beside the original domain. For instance, for a simulation box in 2-D that has x boundaries at -1 and 1 and y boundaries at -1 and 1, cells at (0.25,1) interact with cells at (0.25, -1), and cells at (1, 0.25) interact with the cells at (-1,0.25), etc.[3] Likewise, particles that would move outside the simulation domain reappear on the opposite side, and interact with particles on the opposite side of the simulation domain through the periodic boundary.

In the local expansion described in Section 4.1 and equations 4.2—and in any Keplerian rotating disk—a radial gradient exists in the azimuthal velocities in the simulation. For a given radial position R from the central star, material interior to R has a larger azimuthal velocity than the material at R, and material exterior to R has a smaller azimuthal velocity. Hawley et al. (1995) designed a simulation domain which could emulate this shearing, local expansion. At the radial boundary of this domains, the connections between cells across the periodic boundary shift in the azimuthal direction over time. This is illustrated in Figure 4.5. In the left panel of this figure, we see that copies that exist at the two boundaries in the radial direction must shift in opposing azimuthal directions in order to maintain the shear correctly. A correction

[3]The concept is easily extrapolated to three dimensions, with analogous behaviour occurring at the z boundary to that described for the x and y boundaries.

to the azimuthal velocity within the shearing box simulation domain must also be applied so that the radial shear exists within the box as well.

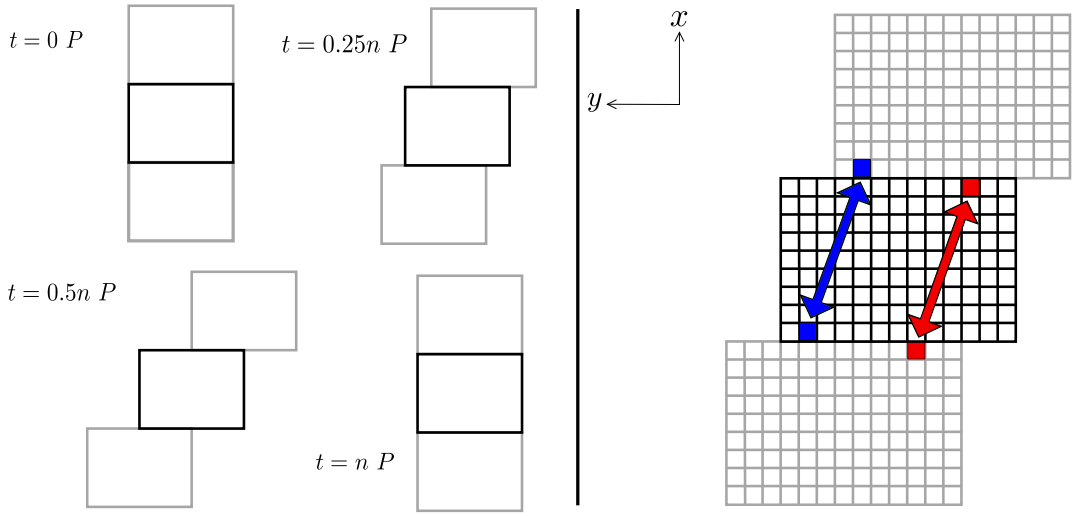

Figure 4.5: Schematic representation of the shearing box set-up, based on a similar figure from Hawley et al. (1995). In both frames, the simulation domain is represented by the bold rectangles, and the shear-periodic copies of the domain are more transparent. *Left.* The copies of the simulation domain on the radial direction (labelled x in the figure) shift in the azimuthal direction as the simulation moves forward in time. On the positive-side radial boundary, the image of the domain must move in the negative azimuthal ($-y$) direction, and on the negative-side radial boundary, the domain must move in the positive azimuthal direction. Once the copies of the simulation domain shift across the entire azimuthal length, the image is recentred so that the images and the simulation domain are aligned, and the process restarts. *Right.* A visual representation of how the connection between cells or grid points across the shear periodic boundary must in general cross the simulation domain diagonally. The only exception is when $t = 0$ or an integer number of the shearing periods (represented by P in the left frame), in which case the simulation domain and the images in the radial direction are exactly aligned as in the standard periodic boundary set-up.

4.4 Confirmation of enhanced SI growth rates in numerical simulations

The crosses marked on Figure 4.6 represent growth rates that were measured from numerical experiments. We tested the enhanced SI growth rates predicted in Figure 4.6 using the Eulerian astrophysics simulation code Athena (Stone et al. 2008). This

experiment was slightly modified from those used in Youdin and Johansen (2007) and Bai and Stone (2010a) to confirm the original SI growth rates from Figures 4.1 and 4.2. These experiments involve a 2-D box with periodic boundary conditions and a radial pressure gradient. To date, no confirmation of the enhanced SI growth rates from the Squire and Hopkins (2018) analysis in numerical experiments have been reported in the literature. Whether or not these enhancements are applicable in the evolution of full 3-D protoplanetary disks is an open question worthy of further research.

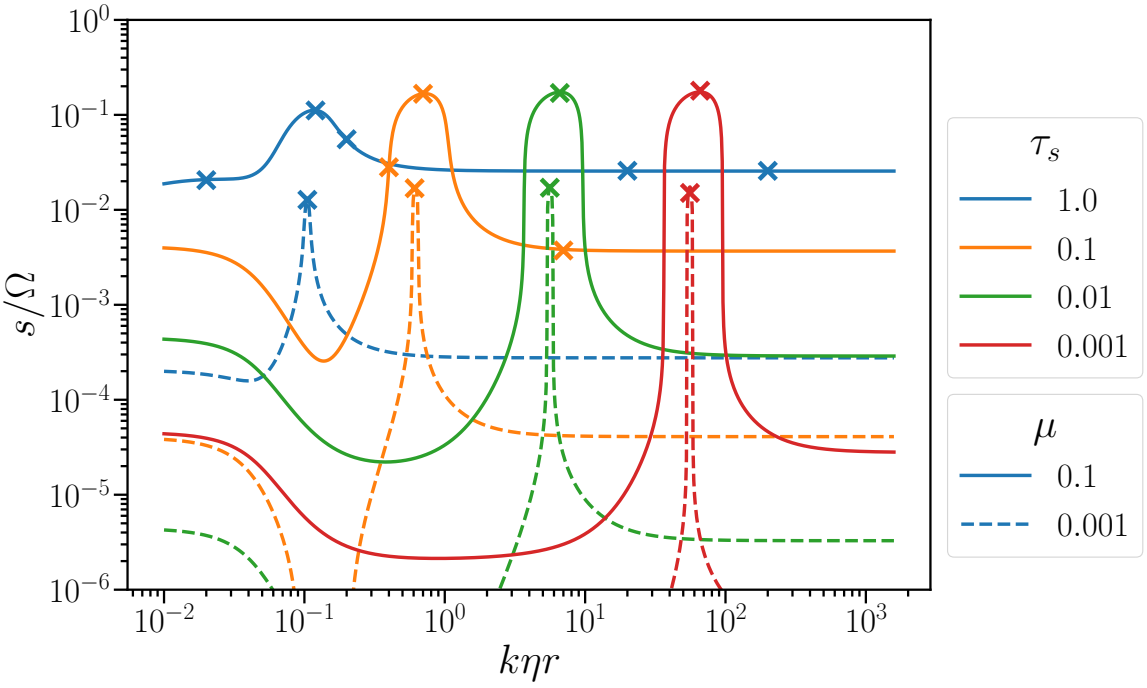

Figure 4.6: Confirmation of the enhanced growth rates of the linear wave perturbation amplitudes from numerical simulations. Crosses mark the numerical results from a 2-D (r-z) periodic box.

4.5 Characteristics of 3-D simulations of the non-linear SI

In this section we present distributions of dust particles from high resolution simulations of the non-linear evolution of the streaming instability. We created these simulations using a shear-periodic box in Athena (Stone et al. 2008). The parameters of the simulation are described in the caption of Figure 4.7, and are similar to those explored

by Bai and Stone (2010b). In each of Figures 4.7, 4.8 and 4.9, we present the position of dust particles, coloured by their local density. These plots demonstrate the three-dimensional dust structures created by the streaming instability.

Figure 4.7 shows an early stage of the non-linear evolution of the SI. The dust in this simulation begins dispersed above and below the disk midplane (see Figure 4.9), and once it settles to a thin layer near $z = 0$ after 6.25 orbits, the SI activates and the pattern shown in Figure 4.7 appears. The shape of this pattern in the x-y and y-z plane are shown in Figure 4.8 and 4.9, respectively. We can discern, even by eye, an angled, striped pattern in the middle frame of Figure 4.8 that suggests the presence of some dominant resonant mode with a wavevector with an x *and* y component. Indeed, when the 2-D fast Fourier transform is applied to the vertically integrated dust surface density, shown in Figure 4.10, we can observe the prevalence of modes which lie on an angle θ_k in the k_x-k_y plane. This angle is not constant in time but evolves. A full study would examine to what extent it is tied to the box parameters or numerical choices rather than purely physical considerations. However, we lack the starting point of theoretical predictions for the planar, non-axisymmetric case. These modes were not explored in the axisymmetric linear perturbation analyses of Youdin and Goodman (2005), Youdin and Johansen (2007) or Squire and Hopkins (2018). A non-axisymmetric analysis is more difficult. As is discussed in Section 4.6, the growth rates vary with time and the long term outcomes are difficult to characterize in simple terms as in the axisymmetric (r-z) case.

In the Johansen et al. (2007) study introduced in Section 1.5.1, they activated self-gravity in a very similar simulation to that presented here once a saturated state of the non-linearly evolving SI was reached. An example of the dust distribution in such a state is shown in the right panels of Figures 4.8 and 4.9. The dust at this point of the simulation is clumped into long, dense, filamentary structures. Turning on self-gravity caused these structures to fragment into more compact bound clumps. A recent study, Simon et al. (2017), explored the mass distribution of the clumps formed from this method. They conclude that this distribution follows a power-law, $dN/dM_p \propto M_p^{-q}$, where $q \sim 1.6$ and the mass of the clumps or planetesimals is given by M_p. Interestingly, they claim this power-law may be universal, and is applicable in simulations with different dust fractions and very different grain sizes.

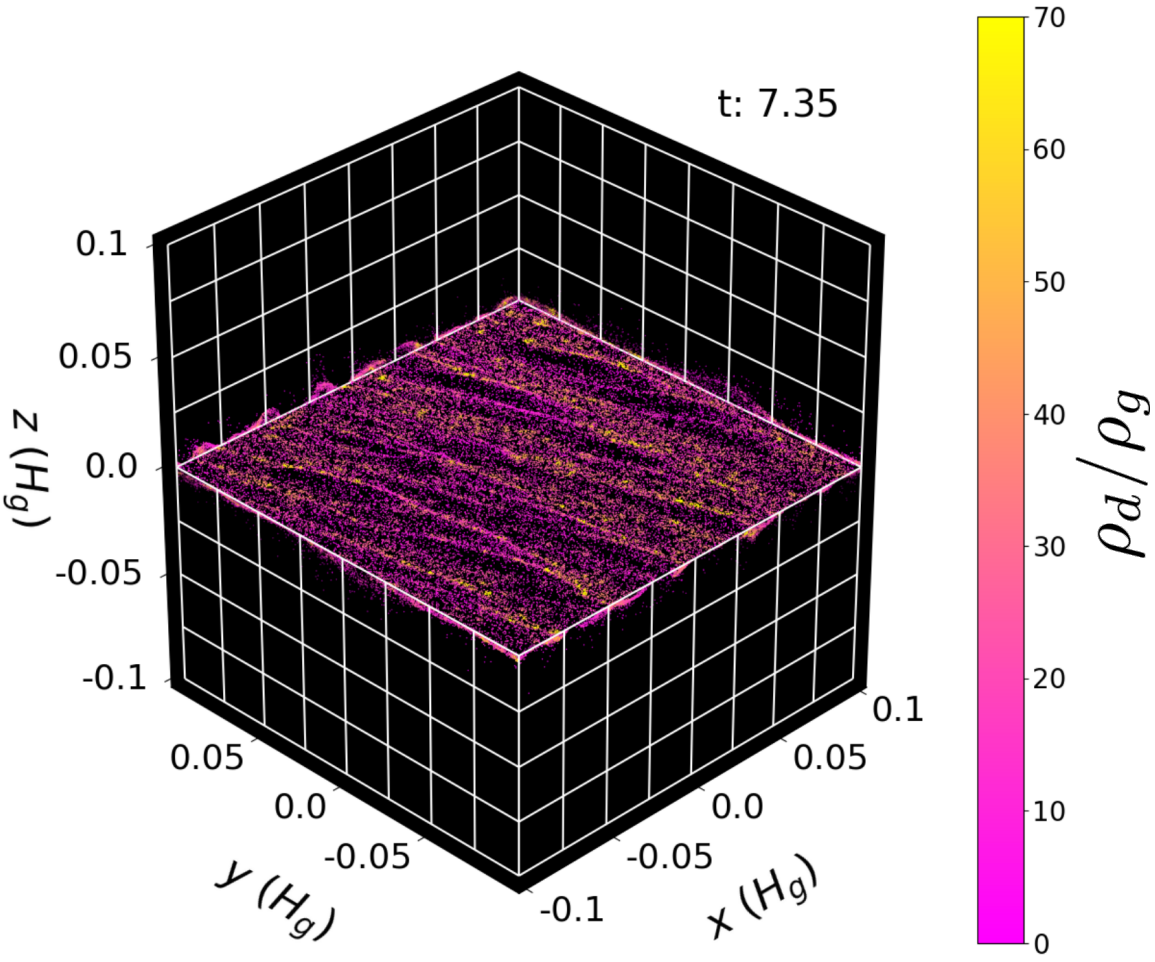

Figure 4.7: Distribution of dust in a high-resolution 3-D simulation of dust and gas in shearing box generated using the Athena astrophysics code. Dust particles are coloured by the dust density. The number of grid points in x, y and z are 256, 256 and 384, respectively, and 1.8×10^7 dust particles are used. Only particles within the vicinity of the midplane ($|z| < 0.03$) are shown in the middle square, and the particles that are shown on the boundaries of the domain, on top of the white mesh, are the particles within a similar tolerance of each boundary. Note that the true domain of the simulation extends to $\pm 0.15 H_g$ is z, but only $\pm 0.10 H_g$ is shown in z. A dust to gas mass ratio of $\mu = 0.03$ is used, and the dust grain size is such that $\tau_s = 1$. The radial pressure gradient for the gas is represented by $\eta v_K = 0.05$ (see equation 3.24). The time inset in the top right corner is in units of the orbital period.

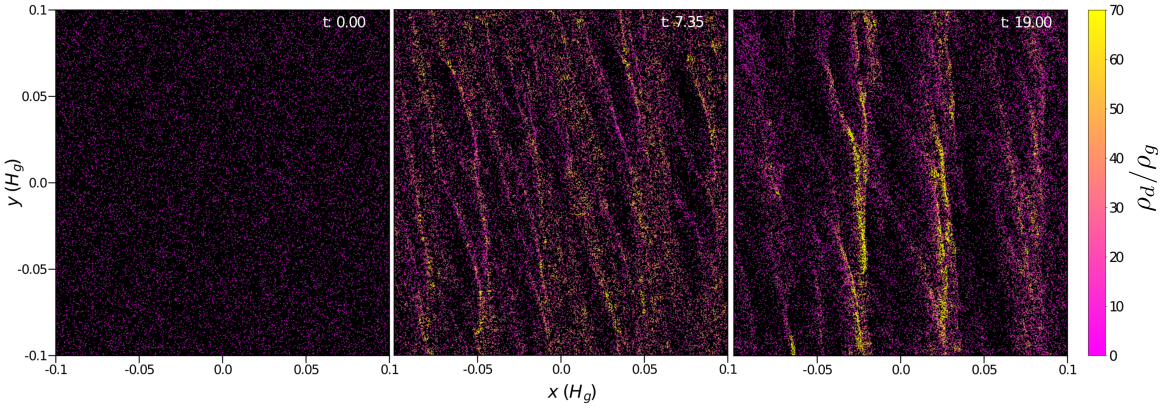

Figure 4.8: Distribution of dust from the same simulation in Figure 4.7, but only positions in the r-θ (x-y) plane and with $|z| < 0.03$ are shown. The time inset in the top right corner is in units of the orbital period.

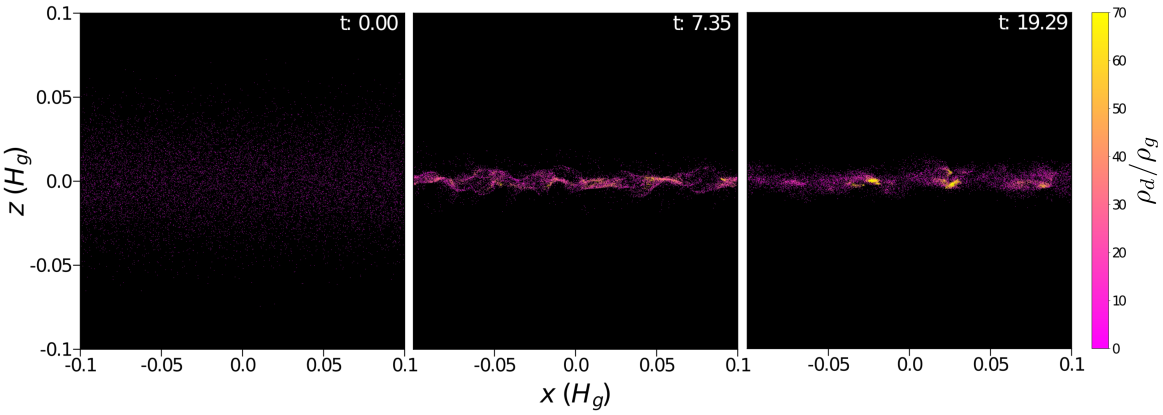

Figure 4.9: Distribution of dust from the same simulation in Figure 4.7, but only positions in the r-z (x-z) plane and with $|\theta| < 0.03$ are shown. The time inset in the top right corner is in units of the orbital period.

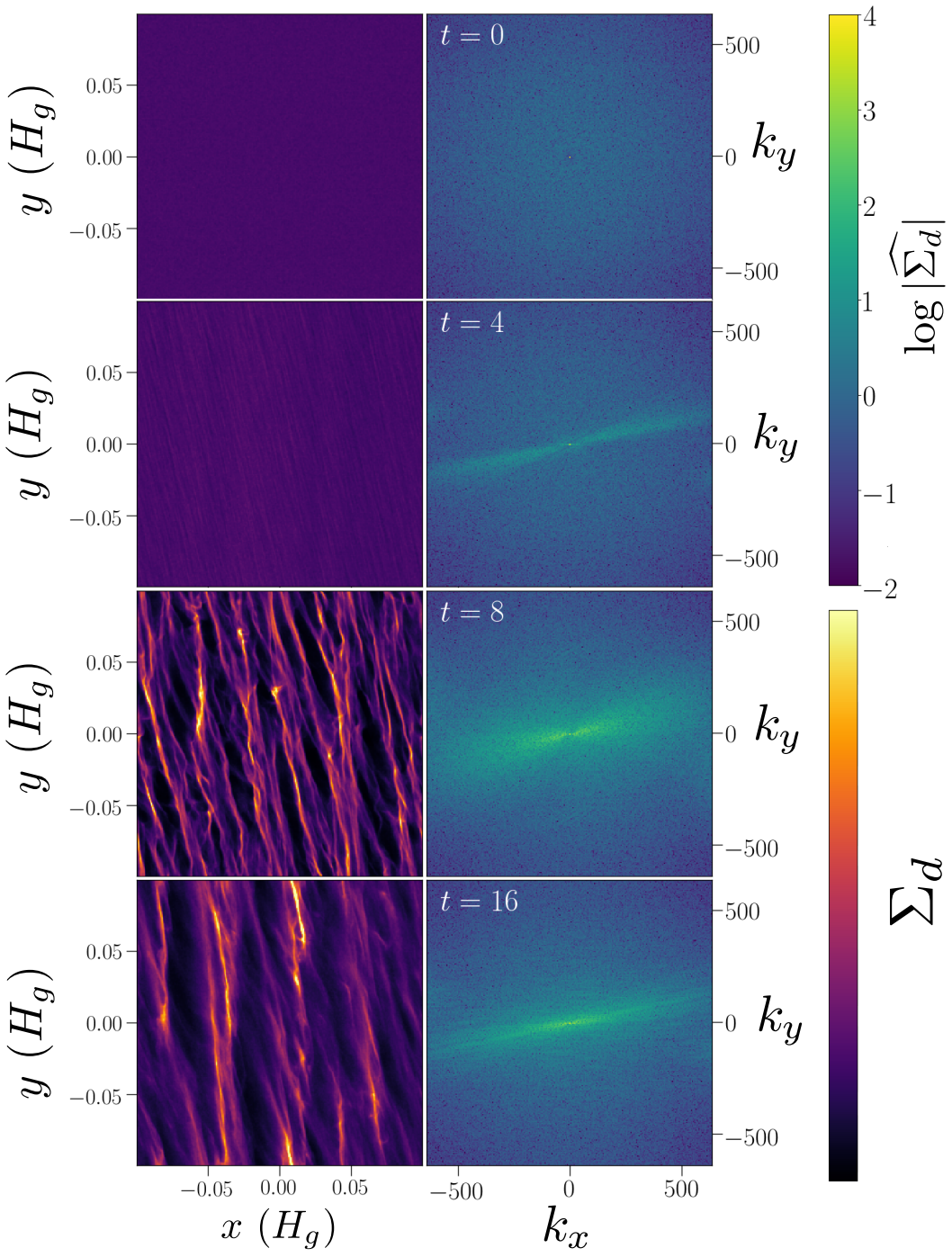

Figure 4.10: Distribution of dust surface density from the same simulation in Figure 4.7 and the 2-D FFT of the surface density. The left panels represent the vertically integrated dust surface density Σ_d in the x-y plane of the simulation, and the right panels represent the magnitude of the 2-D FFT of Σ_d in the k_x-k_y plane. The time inset is in units of the orbital period.

4.6 Non-axisymmetric perturbations

In this section, we will explore the linear plane wave perturbation analysis as in Section 4.1, but this time we will retain any terms that involve gradients in the y direction as we will perturb the equations in the x and y direction. Note that there will be no simple solution as in the axisymmetric case. An exact eigenvector analysis will not be possible, and we will have to solve the coupled differential equations numerically.

We can start with the equations 4.2, which represent a local expansion of a coupled dust and gas system in a rotating frame. This time we will retain the $\partial/\partial y$ term, which is associated with advection by the local shear, $\boldsymbol{V}_0 = (3/2)\Omega x\hat{\mathbf{y}}$. We will note a change in the sign convention in this shear flow to point in the positive y direction (for positive valued x). As a consequence the $-(1/2)\Omega w_x\hat{y}$ term becomes $(1/2)\Omega w_x\hat{y}$. This is similar to the analysis of Goldreich and Lynden-Bell (1965b), who investigated a non-axisymmetric perturbation to a gaseous disk. Thus, we have,

$$\frac{\partial \rho_d}{\partial t} + \boldsymbol{v}\cdot\nabla\rho_d + \frac{3}{2}\Omega x\frac{\partial \rho_d}{\partial y} = -\rho_d\nabla\cdot\boldsymbol{v} \tag{4.26a}$$

$$\frac{\partial \boldsymbol{v}}{\partial t} + (\boldsymbol{v}\cdot\nabla)\boldsymbol{v} + \frac{3}{2}\Omega x\frac{\partial \boldsymbol{v}}{\partial y} = 2\Omega w_y\hat{x} + \frac{1}{2}\Omega w_x\hat{y} - \frac{1}{\tau_f}(\boldsymbol{v}-\boldsymbol{u}) \tag{4.26b}$$

$$\frac{\partial \rho_g}{\partial t} + \boldsymbol{u}\cdot\nabla\rho_g + \frac{3}{2}\Omega x\frac{\partial \rho_g}{\partial y} = -\rho_g\nabla\cdot\delta\boldsymbol{u} \tag{4.26c}$$

$$\frac{\partial \boldsymbol{u}}{\partial t} + (\boldsymbol{u}\cdot\nabla)\boldsymbol{u} + \frac{3}{2}\Omega x\frac{\partial \boldsymbol{u}}{\partial y} = 2\Omega u_y\hat{x} + \frac{1}{2}\Omega u_x\hat{y} - {c_s}^2\nabla\ln\rho_g + 2\eta v_k\Omega\hat{x} - \frac{\epsilon}{\tau_f}(\boldsymbol{u}-\boldsymbol{v}) \tag{4.26d}$$

As before, we will apply a small perturbation to the system, and all perturbations will be represented by a δ. As in Section 4.1, we represent perturbations to the velocities and densities as,

$$\boldsymbol{v} = \overline{\boldsymbol{v}} + \delta\boldsymbol{v} \tag{4.27}$$

$$w_x = \overline{w}_x + \delta w_x \tag{4.28}$$

$$\rho_d = \rho_{p0}[1 + \delta\rho_d] \tag{4.29}$$

where the overbarred values and values with a subscript 0 are the background values. For now, we will not prescribe a specific functional form for the perturbations, but we still require the magnitude of the perturbations to be much smaller than the background.

Following similar simplifications as Section 4.1.1, the full six equations (note we are now neglecting vertical gradients entirely) are,

$$\frac{\partial \delta\rho_d}{\partial t} + \Big(\overline{w}_x \frac{\partial}{\partial x} + \overline{w}_y \frac{\partial}{\partial y}\Big)\delta\rho_d + \frac{3}{2}\Omega x \frac{\partial(\delta\rho_d)}{\partial y} = -\Big(\frac{\partial}{\partial x}\delta w_x + \frac{\partial}{\partial y}\delta w_y\Big) \tag{4.30a}$$

$$\frac{\partial w_x}{\partial t} + \Big(\overline{w}_x \frac{\partial}{\partial x} + \overline{w}_y \frac{\partial}{\partial y}\Big)\delta w_x + \frac{3}{2}\Omega x \frac{\partial(\delta w_x)}{\partial y} = 2\Omega \delta w_y \hat{x} - \frac{\Omega}{\tau_s}(\delta w_x - \delta u_x) \tag{4.30b}$$

$$\frac{\partial w_y}{\partial t} + \Big(\overline{w}_x \frac{\partial}{\partial x} + \overline{w}_y \frac{\partial}{\partial y}\Big)\delta w_y + \frac{3}{2}\Omega x \frac{\partial(\delta w_y)}{\partial y} = \frac{1}{2}\Omega \delta w_x \hat{y} - \frac{\Omega}{\tau_s}(\delta w_y - \delta u_y) \tag{4.30c}$$

$$\frac{\partial \delta\rho_g}{\partial t} + \Big(\overline{u}_x \frac{\partial}{\partial x} + \overline{u}_y \frac{\partial}{\partial y}\Big)\delta\rho_g + \frac{3}{2}\Omega x \frac{\partial(\delta\rho_d)}{\partial y} = \Big(\frac{\partial}{\partial x}\delta u_x + \frac{\partial}{\partial y}\delta u_y\Big) \tag{4.30d}$$

$$\begin{aligned}\frac{\partial u_x}{\partial t} + \Big(\overline{u}_x \frac{\partial}{\partial x} + \overline{u}_y \frac{\partial}{\partial y}\Big)\delta u_x + \frac{3}{2}\Omega x \frac{\partial(\delta u_x)}{\partial y} &= 2\Omega \delta u_y \hat{x} \\ &- {c_s}^2 \frac{\partial(\delta\rho_g)}{\partial x} - \frac{\Omega\epsilon}{\tau_s}\Big(\delta u_x - \delta w_x - (\delta\rho_d - \delta\rho_g)(\overline{w_x} - \overline{u_x})\Big)\end{aligned} \tag{4.30e}$$

$$\begin{aligned}\frac{\partial u_y}{\partial t} + \Big(\overline{u}_x \frac{\partial}{\partial x} + \overline{u}_y \frac{\partial}{\partial y}\Big)\delta u_y + \frac{3}{2}\Omega x \frac{\partial(\delta u_y)}{\partial y} &= \frac{1}{2}\Omega \delta u_x \hat{y} \\ &- {c_s}^2 \frac{\partial(\delta\rho_g)}{\partial y} - \frac{\Omega\epsilon}{\tau_s}\Big(\delta u_y - \delta w_y - (\delta\rho_d - \delta\rho_g)(\overline{w_y} - \overline{u_y})\Big)\end{aligned} \tag{4.30f}$$

4.6.1 Sheared axis perturbation

Following Goldreich and Lynden-Bell (1965b), we transform to sheared axes, which we'll denote with a $'$,

$$x' = x \tag{4.31a}$$
$$y' = y - (3/2)\Omega x t \tag{4.31b}$$
$$t' = t \tag{4.31c}$$

The derivatives in this sheared frame are,

$$\frac{\partial}{\partial x} = \frac{\partial}{\partial x'} - (3/2)\Omega t' \frac{\partial}{\partial y'} \tag{4.32a}$$
$$\frac{\partial}{\partial y} = \frac{\partial}{\partial y'} \tag{4.32b}$$
$$\frac{\partial}{\partial t} = \frac{\partial}{\partial t'} - (3/2)\Omega x' \frac{\partial}{\partial y'} \tag{4.32c}$$

We will consider the inclusion of these sheared-frame derivatives with just one equation, for now: equation 4.30. First, we will add the $\partial/\partial t$ time derivative, and change the variable x to x',

$$\Big(\frac{\partial}{\partial t'} - \frac{3}{2}\Omega x' \frac{\partial}{\partial y'}\Big)\delta\rho_d + \Big(\overline{w}_x \frac{\partial}{\partial x} + \overline{w}_y \frac{\partial}{\partial y}\Big)\delta\rho_d + \frac{3}{2}\Omega x' \frac{\partial(\delta\rho_d)}{\partial y'} = -\Big(\frac{\partial}{\partial x}\delta w_x + \frac{\partial}{\partial y}\delta w_y\Big)$$

which cancels the following term,

$$-\frac{3}{2}\Omega x' \frac{\partial(\delta\rho_d)}{\partial y'}$$

leaving us with,

$$\frac{\partial \delta\rho_d}{\partial t'} + \Big(\overline{w}_x \frac{\partial}{\partial x} + \overline{w}_y \frac{\partial}{\partial y}\Big)\delta\rho_d = -\Big(\frac{\partial}{\partial x}\delta w_x + \frac{\partial}{\partial y}\delta w_y\Big)$$

Now, consider this factor:

$$\overline{w}_x \frac{\partial}{\partial x} + \overline{w}_y \frac{\partial}{\partial y}$$

with the addition of the sheared frame derivatives:

$$\overline{w}_x\Big(\frac{\partial}{\partial x'} - (3/2)\Omega t'\frac{\partial}{\partial y'}\Big) + \overline{w}_y\frac{\partial}{\partial y'}$$

$$\overline{w}_x\frac{\partial}{\partial x'} + \Big(\overline{w}_y - \overline{w}_x(3/2)\Omega t'\Big)\frac{\partial}{\partial y'} \tag{4.33}$$

Now, we assume the functional form of the perturbation is a plane wave, in the sheared axes (with unknown time dependence). Explicitly,

$$\delta f(t) \propto \exp i(k_x x' + k_y y')$$

so that,

$$\frac{\partial \delta f}{\partial x'} = ik_x\delta f$$
$$\frac{\partial \delta f}{\partial y'} = ik_y\delta f$$

Thus, returning to the factor in equation 4.33 and applying it to $\delta\rho_d$, we now have,

$$\begin{aligned}\Big(\overline{w}_x\frac{\partial}{\partial x'} + \Big(\overline{w}_y - \overline{w}_x(3/2)\Omega t'\Big)\frac{\partial}{\partial y'}\Big)\delta\rho_d &= i\Big(\overline{w}_x k_x + \Big(\overline{w}_y - \overline{w}_x(3/2)\Omega t'\Big)k_y\Big)\delta\rho_d \\ &= ik_y\Big(\overline{w}_y - \overline{w}_x((3/2)\Omega t' - k_x/k_y)\Big)\delta\rho_d\end{aligned}$$

as in Goldreich and Lynden-Bell (1965b), we define

$$\tau \equiv (3/2)\Omega t' - k_x/k_y \tag{4.34}$$

Now, the previous term is,

$$ik_y(-\overline{w}_x\tau + \overline{w}_y)\delta\rho_d$$

Through a similar process,

$$\frac{\partial}{\partial x'}\delta w_x + \frac{\partial}{\partial y'}\Big(\delta w_y - (3/2)\Omega t'\delta w_x\Big) = ik_y(-\delta w_x\tau + \delta w_y)$$

Finally, we will change the time derivatives to derivatives in τ. Via chain rule,

$$\frac{\partial f}{\partial t'} = \frac{\partial f}{\partial \tau}\frac{\partial \tau}{\partial t'}$$

From equation 4.34, we have,

$$\frac{\partial \tau}{\partial t'} = \frac{3}{2}\Omega$$

and we will define,

$$k \equiv \frac{2}{3\Omega}k_y$$

Now, returning to equations 4.30, the final six equations that describe the perturbed system are,

$$\frac{\partial \delta\rho_d}{\partial \tau} + ik(-\overline{w}_x\tau + \overline{w}_y)\delta\rho_d = -ik(-\delta w_x\tau + \delta w_y) \tag{4.35a}$$

$$\frac{\partial \delta w_x}{\partial \tau} + ik(-\overline{w}_x\tau + \overline{w}_y)\delta w_x = \frac{4}{3}\delta w_y - \frac{2}{3}\frac{1}{\tau_s}(\delta w_x - \delta u_x) \tag{4.35b}$$

$$\frac{\partial \delta w_y}{\partial \tau} + ik(-\overline{w}_x\tau + \overline{w}_y)\delta w_y = \frac{1}{3}\delta w_x - \frac{2}{3}\frac{1}{\tau_s}(\delta w_y - \delta u_y) \tag{4.35c}$$

$$\frac{\partial \delta\rho_g}{\partial \tau} + ik(-\overline{u}_x\tau + \overline{u}_y)\delta\rho_g = -ik(-\delta u_x\tau + \delta u_y) \tag{4.35d}$$

$$\frac{\partial \delta u_x}{\partial \tau} + ik(-\overline{u}_x\tau + \overline{u}_y)\delta u_x = \frac{4}{3}\delta u_y - ikc_s{}^2(-\tau)\delta\rho_g - \frac{2}{3}\frac{\epsilon}{\tau_s}\Big(\delta u_x - \delta w_x - (\delta\rho_d - \delta\rho_g)(\overline{w_x} - \overline{u_x})\Big) \tag{4.35e}$$

$$\frac{\partial \delta u_y}{\partial \tau} + ik(-\overline{u}_x\tau + \overline{u}_y)\delta u_y = \frac{1}{3}\delta u_x - ikc_s{}^2\delta\rho_g - \frac{2}{3}\frac{\epsilon}{\tau_s}\Big(\delta u_y - \delta w_y - (\delta\rho_d - \delta\rho_g)(\overline{w_y} - \overline{u_y})\Big) \tag{4.35f}$$

4.6.2 Exploring the non-axisymmetric perturbed system

As mentioned earlier, solving equations 4.35 is more complicated than solving the axisymmetric equations sets of 4.13 and 4.17 due to the presence of terms which are time varying. (Note the terms of the form $ik(-\overline{u}_x\tau + \overline{u}_y)$.) Solving this system is

not possible with an eigenvalue analysis, and it will be more difficult to discover a single growth rate for any set of perturbation parameters. However, outside of the gas parameters c_s and η, the system is still uniquely described by the same four values as before: μ, τ_s, k_x, k_y.

We are interested in exploring the dynamics of this perturbed system by solving equations 4.35 directly with standard coupled different equation methods such as Runge-Kutta methods. Integrating this system over the dimensionless time parameter τ will be computationally inexpensive. Thus the parameter space laid out by (μ, τ_s, k_x, k_y) can be explored by brute force. We have already explored a few cases, but it is clear that a systematic study which is able to fully characterize the outcomes is needed. In particular, we would like to identify preferred wavevectors if present and relate those to the simulation results of Section 4.5. Due to time constraints we were unable to go further along this path but we intend to in future work.

Chapter 5

Conclusions

Planet formation is a multi-stage process that follows the growth of micron sized dust grains to full sized planets that span thousands of kilometres. The earliest stages of this process, as grains grow to become kilometre sized planetesimals, faces a well-documented pair of constraints known collectively as the metre barrier. In this thesis we discuss techniques for studying mechanisms which may be capable of overcoming the metre barrier with numerical simulations.

A recent study by Gonzalez et al. 2017 reported on a promising mechanism which claimed self-induced dust traps are capable of forming in protoplanetary disks, and within these traps, small dust grains could grow to form planetesimals. Thus, we attempted to explore their results further by using and modifying the one-fluid dust-gas prescription that our collaborators implemented in our SPH program ChaNGa (Menon et al. 2015). However, we discovered that one-fluid schemes are overly diffusive, and thus would not be useful for exploring the results of the Gonzalez et al. 2017 study which depends on strong dust concentration. We decided to develop a two-fluid dust-gas scheme in ChaNGa, which is the method used in Gonzalez et al. 2017 and is capable of modelling significant dust coagulation.

In Chapter 2 we explored both one-fluid scheme and two-fluid schemes for described a coupled dust-gas system. In Chapter 3, we discussed associated SPH implementations which have been developed and tested by G. Laibe and D. J. Price, two of the prominent researchers using SPH to study dust in astrophysics (Laibe and Price 2012, Laibe and Price 2014b). In Sections 3.3.1 to 3.3.3 we outlined our attempts to quantify the performance of the numerical method in full three-dimensional protoplanetary disk

simulations. We discovered that, on the scale of full protoplanetary disks, noise present in the SPH density estimator obscures subtle aerodynamic behaviour of the dust grains such as radial drift. With these results, along with private communications with Laibe and Price, we discovered that simulators employing SPH to study dust behaviour must be careful to avoid integrating simulations for many orbits or dynamical times. These errors will become imparted on the dust, and may end up manufacturing macroscopic behaviour that can affect the results of experiment. Thus SPH can be effective for problems with larger perturbers (e.g. planets and binary companions as in the work of Price and Laibe) but is has yet to be proven suitable for cases that rely on growth of small perturbations. The Gonzalez et al. 2017 study ran their simulations for hundreds of orbits from quiet initial disks, and this could have driven some of their results.

Gonzalez et al. proposed a new growth mechanism in a complex scenario. Based on our experiences, we decided to examine a simpler and arguably more fundamental mechanism for the formation of planetesimals known as the streaming instability (SI) (Youdin and Goodman 2005). The analytical theory behind this mechanism is thoroughly developed, and high-resolution 3D simulations have demonstrated that the non-linear regime of this instability can concentrate an initially disperse dust distribution to large overdensities. The previously mentioned density noise errors in SPH make it difficult to study the linear evolution of the instability. In private communications, Price and Laibe have informed us of their unsuccessful efforts to capture the linear SI in SPH. Thus, we decided to use an established Eulerian astrophysics code, Athena (Stone et al. 2008). Modules to simulate dust and the streaming instability in Athena are publicly available and have been tested (Bai and Stone 2010a). Thus Athena provides a solid framework to explore the analytic instability as well as a benchmark for comparing alternate methods (such as an improved SPH treatment). In Chapter 4 we explored our investigations involving the SI. We confirmed the predicted enhancement to the SI growth rates from Squire and Hopkins 2018 with our numerical simulations, and have begun an exploration into the non-axisymmetric modes of the streaming instability.

The original analytic theory for the streaming instability only considered axisymmetric perturbations to the coupled dust-gas system. This perturbation is analytically solvable using an eigenvalue analysis, and predicts specific growth rates that could be confirmed in numerical simulations. We are interested in exploring the presence of modes in the radial-azimuthal plane (i.e. x-y) which can experience significant growth,

as it appears it is these modes which dominate the non-linear evolution of the SI in simulations with periodic shearing boxes. This is at odds with the existing theoretical frameworks which are not-only axisymmetric but also assume a thick disk extending in r and z. The non-axisymmetric theory is more complex and difficult to work with but we have made inroads and will explore this analysis further.

Beyond the non-axisymmetric SI peturbation study, we are interested in exploring other additions to the non-linear SI theory, including:

- developing a shearing box module in ChaNGa to study the non-linear SI
- exploring how grain growth affects the non-linear evolution of the streaming instability

The main objective of our research is to build an array of robust numerical approaches for studying dust in protoplanetary disks during the early stages of planet formation, and investigate how mechanisms such as the streaming instability are capable of overcoming the metre barrier.

Bibliography

Adams, F. C. et al. (1987). "Spectral evolution of young stellar objects". *ApJ* 312, pp. 788–806.

ALMA Science Portal (2018). Online, visited on 2018-08-17. URL: `https://almascience.nrao.edu/about-alma`.

Andre, P. et al. (2000). "From Prestellar Cores to Protostars: the Initial Conditions of Star Formation". *Protostars and Planets IV*, p. 59.

Andrews, S. M. et al. (2016). "Ringed Substructure and a Gap at 1 au in the Nearest Protoplanetary Disk". *ApJL* 820, L40, p. L40.

Armitage, Philip J. (2013). *Astrophysics of Planet Formation*. Cambridge University Press.

Ayliffe, B. A. et al. (2012). "On the accumulation of planetesimals near disc gaps created by protoplanets". *MNRAS* 423, pp. 1450–1462.

Bai, X.-N. and J. M. Stone (2010a). "Particle-gas Dynamics with Athena: Method and Convergence". *ApJ Supp.* 190, pp. 297–310.

Bai, X.-N. and J. M. Stone (2010b). "Dynamics of Solids in the Midplane of Protoplanetary Disks: Implications for Planetesimal Formation". *ApJ* 722, pp. 1437–1459.

Bai, X.-N. and J. M. Stone (2010c). "The Effect of the Radial Pressure Gradient in Protoplanetary Disks on Planetesimal Formation". *ApJL* 722, pp. L220–L223.

Baines, M. J. et al. (1965). "Resistance to the motion of a small sphere moving through a gas". *MNRAS* 130, p. 63.

Bally, J. et al. (2000). "Disks, Microjets, Windblown Bubbles, and Outflows in the Orion Nebula". *Astronomical Journal* 119, pp. 2919–2959.

Beaulieu, J.-P. et al. (2006). "Discovery of a cool planet of 5.5 Earth masses through gravitational microlensing". *Nature* 439, pp. 437–440.

Benisty, M. et al. (2015). "Asymmetric features in the protoplanetary disk MWC 758". *Astron. & Astrophys.* 578, L6, p. L6.

Birnstiel, T. et al. (2010). "Gas- and dust evolution in protoplanetary disks". *Astron. & Astrophys.* 513, A79, A79.

Blum, J. and G. Wurm (2008). "The Growth Mechanisms of Macroscopic Bodies in Protoplanetary Disks". *Ann. Rev. of Astron. & Astrophys.* 46, pp. 21–56.

Borucki, W. J. et al. (2010). "Kepler Planet-Detection Mission: Introduction and First Results". *Science* 327, p. 977.

Brandenburg, A. (2003). "Computational aspects of astrophysical MHD and turbulence". *Advances in Nonlinear Dynamics*. Ed. by A. Ferriz-Mas and M. Núñez, p. 269.

Calvet, N. et al. (1994). "Flat spectrum T Tauri stars: The case for infall". *ApJ* 434, pp. 330–340.

Capobianco, C. C. et al. (2011). "Planetesimal-driven planet migration in the presence of a gas disk". *Icarus* 211, pp. 819–831.

Charbonneau, D. et al. (2007). "When Extrasolar Planets Transit Their Parent Stars". *Protostars and Planets V*, pp. 701–716.

Chiang, E. and A. Youdin (2010). "Forming Planetesimals in Solar and Extrasolar Nebulae". *Annual Review of Earth and Planetary Sciences* 38, pp. 493–522.

Colella, P. and P. R. Woodward (1984). "The Piecewise Parabolic Method (PPM) for Gas-Dynamical Simulations". *Journal of Computational Physics* 54, pp. 174–201.

Courant, R. et al. (1967). "On the Partial Difference Equations of Mathematical Physics". *IBM Journal of Research and Development* 11, pp. 215–234.

de Pater, Imke and Jack J. Lissauer (2010). *Planetary Sciences*. Cambridge University Press.

Dipierro, G. et al. (2015). "On planet formation in HL Tau". *MNRAS* 453, pp. L73–L77.

Dipierro, G. et al. (2016). "Two mechanisms for dust gap opening in protoplanetary discs". *MNRAS* 459, pp. L1–L5.

Dong, Ruobing et al. (2018). "The Eccentric Cavity, Triple Rings, Two-armed Spirals, and Double Clumps of the MWC 758 Disk". *The Astrophysical Journal* 860.2, p. 124. URL: http://stacks.iop.org/0004-637X/860/i=2/a=124.

Draine, B. T. (2003). "Interstellar Dust Grains". *Ann. Rev. of Astron. & Astrophys.* 41, pp. 241–289.

Epstein, Paul S. (1924). "On the Resistance Experienced by Spheres in their Motion through Gases". *Phys. Rev.* 23 (6), pp. 710–733.

Exoplanet Archive (2018). Online, visited on 2018-08-16. URL: `https://exoplanetarchive.ipac.caltech.edu/`.

Fischer, D. A. et al. (2014). "Exoplanet Detection Techniques". *Protostars and Planets VI*, pp. 715–737.

Fulton, B. J. et al. (2017). "The California-Kepler Survey. III. A Gap in the Radius Distribution of Small Planets". *Astronomical Journal* 154, 109, p. 109.

Goldreich, P. and D. Lynden-Bell (1965a). "I. Gravitational stability of uniformly rotating disks". *MNRAS* 130, p. 97.

Goldreich, P. and D. Lynden-Bell (1965b). "II. Spiral arms as sheared gravitational instabilities". *MNRAS* 130, p. 125.

Gonzalez, J.-F. et al. (2017). "Self-induced dust traps: overcoming planet formation barriers". *MNRAS* 467, pp. 1984–1996.

Greene, T. P. et al. (1994). "Further mid-infrared study of the rho Ophiuchi cloud young stellar population: Luminosities and masses of pre-main-sequence stars". *ApJ* 434, pp. 614–626.

Harlow, F. H. and A. A. Amsden (1975). "Numerical calculation of multiphase fluid flow". *Journal of Computational Physics* 17, pp. 19–52.

Hawley, J. F. et al. (1995). "Local Three-dimensional Magnetohydrodynamic Simulations of Accretion Disks". *ApJ* 440, p. 742.

Hockney, R. W. and J. W. Eastwood (1981). *Computer Simulation Using Particles*.

Johansen, A. and M. Lambrechts (2017). "Forming Planets via Pebble Accretion". *Annual Review of Earth and Planetary Sciences* 45, pp. 359–387.

Johansen, A. and A. Youdin (2007). "Protoplanetary Disk Turbulence Driven by the Streaming Instability: Nonlinear Saturation and Particle Concentration". *ApJ* 662, pp. 627–641.

Johansen, A. et al. (2007). "Rapid planetesimal formation in turbulent circumstellar disks". *Nature* 448, pp. 1022–1025.

Kataoka, A. et al. (2016). "Submillimeter Polarization Observation of the Protoplanetary Disk around HD 142527". *ApJL* 831, L12, p. L12.

Kenyon, S. J. et al. (1993). "The embedded young stars in the Taurus-Auriga molecular cloud. I - Models for spectral energy distributions". *ApJ* 414, pp. 676–694.

Kitsionas, S. and A. P. Whitworth (2002). "Smoothed Particle Hydrodynamics with particle splitting, applied to self-gravitating collapse". *MNRAS* 330, pp. 129–136.

Laibe, G. and D. J. Price (2012). "Dusty gas with smoothed particle hydrodynamics - I. Algorithm and test suite". *MNRAS* 420, pp. 2345–2364.

Laibe, G. and D. J. Price (2014a). "Dusty gas with one fluid". *MNRAS* 440, pp. 2136–2146.

Laibe, G. and D. J. Price (2014b). "Dusty gas with one fluid in smoothed particle hydrodynamics". *MNRAS* 440, pp. 2147–2163.

Laney, Culbert B. (1998). *Computational Gasdynamics*. Cambridge University Press.

LeVeque, Randall J. (2006). *Numerical methods for conservation laws*. 2nd ed. Birkhäuser.

Lissauer, J. J. et al. (2014). "Advances in exoplanet science from Kepler". *Nature* 513, pp. 336–344.

Lorén-Aguilar, P. and M. R. Bate (2016). "Toroidal vortices as a solution to the dust migration problem". *MNRAS* 457, pp. L54–L58.

Lynden-Bell, D. and J. E. Pringle (1974). "The evolution of viscous discs and the origin of the nebular variables." *MNRAS* 168, pp. 603–637.

Marois, C. et al. (2008). "Direct Imaging of Multiple Planets Orbiting the Star HR 8799". *Science* 322, p. 1348.

Mayor, M. and D. Queloz (1995). "A Jupiter-mass companion to a solar-type star". *Nature* 378, pp. 355–359.

Menon, H. et al. (2015). "Adaptive techniques for clustered N-body cosmological simulations". *Computational Astrophysics and Cosmology* 2, 1, p. 1.

Mizuno, H. et al. (1978). "Instability of a gaseous envelope surrounding a planetary core and formation of giant planets". *Progress of Theoretical Physics* 60, pp. 699–710.

Monaghan, J. J. (1992). "Smoothed particle hydrodynamics". *Ann. Rev. of Astron. & Astrophys.* 30, pp. 543–574.

Monaghan, J. J. and A. Kocharyan (1995). "SPH simulation of multi-phase flow". *Computer Physics Communications* 87, pp. 225–235.

Moore, G. S. M. and H. E. Rose (1973). "The Structure of Powdered Quartz". *Nature* 242, p. 187.

Nakagawa, Y. et al. (1986). "Settling and growth of dust particles in a laminar phase of a low-mass solar nebula". *Icarus* 67, pp. 375–390.

Paczyński, Bohdan (1996). "GRAVITATIONAL MICROLENSING IN THE LOCAL GROUP". *Annual Review of Astronomy and Astrophysics* 34.1, pp. 419–459. URL: https://doi.org/10.1146/annurev.astro.34.1.419.

Pérez, Laura M. et al. (2016). "Spiral density waves in a young protoplanetary disk". *Science* 353.6307, pp. 1519–1521.

Perri, F. and A. G. W. Cameron (1974). "Hydrodynamic instability of the solar nebula in the presence of a planetary core". *Icarus* 22, pp. 416–425.

Pollack, J. B. et al. (1996). "Formation of the Giant Planets by Concurrent Accretion of Solids and Gas". *Icarus* 124, pp. 62–85.

Price, D. J. (2012). "Smoothed particle hydrodynamics and magnetohydrodynamics". *Journal of Computational Physics* 231, pp. 759–794.

Price, D. J. and G. Laibe (2015). "A fast and explicit algorithm for simulating the dynamics of small dust grains with smoothed particle hydrodynamics". *MNRAS* 451, pp. 813–826.

Price, D. J. et al. (2018). "Circumbinary, not transitional: on the spiral arms, cavity, shadows, fast radial flows, streamers, and horseshoe in the HD 142527 disc". *MNRAS* 477, pp. 1270–1284.

Rafikov, R. R. (2006). "Atmospheres of Protoplanetary Cores: Critical Mass for Nucleated Instability". *ApJ* 648, pp. 666–682.

Ribas, Á. et al. (2014). "Disk evolution in the solar neighborhood. I. Disk frequencies from 1 to 100 Myr". *Astron. & Astrophys.* 561, A54, A54.

Shakura, N. I. and R. A. Sunyaev (1973). "Black holes in binary systems. Observational appearance." *Astron. & Astrophys.* 24, pp. 337–355.

Simon, J. B. et al. (2017). "Evidence for Universality in the Initial Planetesimal Mass Function". *ApJL* 847, L12, p. L12.

Smith, N. et al. (2005). "New Silhouette Disks with Reflection Nebulae and Outflows in the Orion Nebula and M43". *Astronomical Journal* 129, pp. 382–392.

Sod, G. A. (1978). "A survey of several finite difference methods for systems of nonlinear hyperbolic conservation laws". *Journal of Computational Physics* 27, pp. 1–31.

Squire, J. and P. F. Hopkins (2018). "Resonant drag instabilities in protoplanetary discs: the streaming instability and new, faster growing instabilities". *MNRAS* 477, pp. 5011–5040.

Stepinski, T. F. and P. Valageas (1996). "Global evolution of solid matter in turbulent protoplanetary disks. I. Aerodynamics of solid particles." *Astron. & Astrophys.* 309, pp. 301–312.

Stone, J. M. et al. (2008). "Athena: A New Code for Astrophysical MHD". *ApJ Supp.* 178, pp. 137–177.

Thommes, E. W. et al. (2002). "The Formation of Uranus and Neptune among Jupiter and Saturn". *Astronomical Journal* 123, pp. 2862–2883.

Toomre, A. (1964). "On the gravitational stability of a disk of stars". *ApJ* 139, pp. 1217–1238.

Wadsley, J. W. et al. (2017). "Gasoline2: a modern smoothed particle hydrodynamics code". *MNRAS* 471, pp. 2357–2369.

Weidenschilling, S. J. (1977). "Aerodynamics of solid bodies in the solar nebula". *MNRAS* 180, pp. 57–70.

Weidenschilling, S. J. (1980). "Dust to planetesimals - Settling and coagulation in the solar nebula". *Icarus* 44, pp. 172–189.

Weingartner, J. C. and B. T. Draine (2001). "Dust Grain-Size Distributions and Extinction in the Milky Way, Large Magellanic Cloud, and Small Magellanic Cloud". *ApJ* 548, pp. 296–309.

Williams, David R. (2018). *Planetary Fact Sheet*. Online, visited on 2018-08-22. URL: `https://nssdc.gsfc.nasa.gov/planetary/factsheet/`.

Youdin, A. and J. Goodman (2005). "Streaming Instabilities in Protoplanetary Disks". *ApJ* 620, pp. 459–469.

Youdin, A. and A. Johansen (2007). "Protoplanetary Disk Turbulence Driven by the Streaming Instability: Linear Evolution and Numerical Methods". *ApJ* 662, pp. 613–626.

Zeytounian, R. K. (1991). *Meteorological Fluid Dynamics*.